

Superconducting Radiofrequency Probes For Magnetic Resonance

Microscopy, Simulation And Experiments

by

John C. Nouls

Department of Biomedical Engineering
Duke University

Date: _____

Approved:

G. Allan Johnson, Supervisor

David Enterline

Gregg Trahey

Patrick Wolf

James MacFall

Qing Liu

Dissertation submitted in partial fulfillment of the requirements
for the degree of Doctor of Philosophy
in the Department of Biomedical Engineering
in the Graduate School of Duke University

2009

ABSTRACT

Superconducting Radiofrequency Probes for Magnetic Resonance Microscopy,

Simulation and Experiments

by

John C. Nouls

Department of Biomedical Engineering
Duke University

Date: _____

Approved:

G. Allan Johnson, Supervisor

David Enterline

Gregg Trahey

Patrick Wolf

James MacFall

Qing Liu

An abstract of a dissertation
submitted in partial fulfillment of the requirements for the degree
of Doctor of Philosophy
in the Department of Biomedical Engineering
in the Graduate School of Duke University

2009

Copyright by
John Claude Kenneth Robert Nouis
2009

Abstract

In magnetic resonance microscopy, insufficient signal-to-noise ratio currently limits imaging performance. Superconducting probes can potentially increase the sensitivity of the magnetic resonance experiment. However, many superconducting probes failed to entirely deliver the expected increase in signal-to-noise ratio.

We present a method based on finite-element radiofrequency simulations. The radiofrequency model computes several figures of merit of a probe, namely: i) the resonant frequency, ii) the impedance, iii) the magnetic field homogeneity, iv) the filling factor, and v) the sensitivity. The probe is constituted by several components. The method identifies the component limiting the sensitivity of the probe. Subsequently, the probe design can be improved iteratively.

We show that the sensitivity of an existing superconducting Helmholtz pair can be improved by increasing the filling factor and cooling the radiofrequency shield, which was implemented in the design of a new superconducting probe. The second probe exhibits a sensitivity three times as high, leading to improved imaging performance.

To the shiny, hopping toad that I love a little bit more every day

Contents

Abstract	iv
Contents.....	vi
List of Tables.....	x
List of Figures	xii
List of Abbreviations	xviii
Acknowledgments.....	xix
1 Introduction	1
1.1 The Sensitivity of Magnetic Resonance Microscopy.....	1
1.2 The Meaning of a High-Sensitivity Probe	2
1.3 The Discovery of High-Temperature Superconductivity	5
1.4 High-Sensitivity Cryogenic Probes	6
1.5 The SNR Discrepancy.....	10
1.6 Aims of the Dissertation	14
2 The Signal	15
2.1 The Nuclear Magnetic Resonance Phenomenon.....	15
2.2 Spin Dynamics.....	17
2.3 The Magnetization	18
2.4 The Flip Angle	20
2.5 T ₂ Decay.....	21
2.6 T ₁ Recovery	23

2.7	Signal Transfer and Dissipation Within The Probe.....	24
3	The Noise.....	28
3.1	Thermal Noise	28
3.2	Estimating Resistance.....	29
3.2.1	Analytical Estimation.....	29
3.2.2	Dissipated Power.....	31
3.3	Coupled Noise.....	32
3.4	Noise Transmission within a Probe	35
4	The Signal-To-Noise Ratio	39
4.1	Increasing SNR by Maximizing the Sensitivity	40
4.1.1	Scaling Laws.....	41
4.2	Increasing SNR by Volume Encoding.....	45
4.3	Increasing SNR With Contrast Agents	46
4.4	Increasing SNR with Imaging Sequences.....	48
5	The Radiofrequency Coil.....	51
5.1	Resonant Frequency	51
5.2	Impedance.....	52
5.3	Homogeneity	54
5.4	Filling Factor	54
5.5	Sensitivity.....	55
5.6	Quality Factor	56
5.7	Superconducting Coil Peculiarities	57
6	Finite-Element Radiofrequency Simulations.....	59

6.1	Benefits	60
6.2	Limitations	61
6.3	A Simple Probe.....	62
6.3.1	Probe Configuration.....	62
6.3.2	Precision, Mesh Size and Computation Time.....	64
6.3.3	Validating a Model Experimentally.....	66
6.3.4	Validating a Model Through its Internal Consistency	69
6.3.5	Transformed Resistance.....	71
7	The Beryllia Probe	74
7.1	Probe Configuration	74
7.2	Radiofrequency Simulation.....	76
7.2.1	Model Validation Using a Single Coil	78
7.2.2	Model Validation Using the Probe.....	81
7.3	Resonant Frequency	82
7.4	Impedance.....	82
7.5	Homogeneity	82
7.6	Filling factor.....	84
7.7	Sensitivity.....	85
7.8	Imaging.....	86
7.9	Performance and Improvements	89
8	The Alumina Probe	90
8.1	Design Requirements	90
8.2	Probe Configuration	91

8.2.1	Geometry	91
8.2.2	Cooling.....	92
8.3	Radiofrequency Simulations	93
8.3.1	Resonant Frequency	93
8.3.2	Impedance	95
8.3.3	Filling Factor	97
8.3.4	Sensitivity	99
8.3.5	Quality Factor.....	100
8.4	Imaging.....	100
8.5	Sensitivity and SNR comparisons	103
8.6	Important Aspects of the Probe Design.....	105
8.6.1	Alignment.....	105
8.6.2	Heat Transfer, Thermal Contraction and Vacuum.....	107
8.6.3	Microphonics.....	110
9	Summary	112
10	Appendix.....	115
10.1	Radiofrequency Model of the Beryllia Probe.....	115
10.2	Radiofrequency Model of Alumina Probe	118
10.3	Alumina Heat Exchangers.....	121
10.4	Titanium Heat Exchangers	123
	References	128
	Biography.....	132

List of Tables

Table 6-1: The resonant frequency, the separation distance between the coupling loop and the horse-shoe coil in a matched configuration, as well as the coil quality factor were measured experimentally and compared to the values predicted by the radiofrequency model. For experimental results, the error is given by the standard deviation of 5 measurements. For simulations, the error is given by the standard deviation of the output computed at least 5 times with a different mesh.....	67
Table 6-2: transformed resistance of the probe components. The sum of the resistances of all the components ranges between 54.7 Ω and 61.2 Ω . It should be 50 Ω , the impedance of the radiofrequency chain.....	70
Table 7-1: transformed resistance and absolute temperature of the beryllia probe components.....	85
Table 8-1: temperature of several probe components during normal operation. The top surface of the heat exchangers and the cold shield is believed to be the warmest.....	93
Table 8-2: Size and position of the coupling loop, recorded experimentally and predicted by the radiofrequency simulations, showing good agreement.....	96
Table 8-3: transformed resistance and absolute temperature of the alumina probe components.....	99
Table 8-4: Imaging volume, voxel volume, echo-time, repetition time, bandwidth, number N of samples acquired in the frequency-encoding direction, and acquisition time used by the beryllia probe and the alumina probe.	103
Table 8-5: The SNR recorded experimentally was divided by the square-root of acquisition time ($hr^{-1/2}$), the square root of N, the voxel volume (pL^{-1}) and for convenience, multiplied by 100.....	104
Table 10-1: Electromagnetic properties of the components included in the radiofrequency model of the Beryllia probe	116
Table 10-2: Mesh size for each component of the radiofrequency model of the Beryllia probe	117
Table 10-3: Electromagnetic properties of the components included in the	

radiofrequency model of the Alumina probe 119

Table 10-4: Mesh size for each component of the radiofrequency model of the Alumina probe 120

List of Figures

Figure 1-1: Several research group have produced a superconducting probe between 1991 and 2008. The logarithmic graph shows the unloaded quality factor of the superconducting probes (filled), comparable copper probe (hatched), and illustrates the ability of superconducting probes to exhibit a much larger quality factor than copper probes. 8

Figure 1-2: Several research groups reported an SNR gain by using a superconducting probe (full). Some authors reported a theoretical SNR, often largely exceeding the experimental SNR. The SNR gain missing experimentally is given by hatched blocks... 10

Figure 1-3: On the left part of the figure, the spectrum recorded by Styles (23) shows both signal amplification and noise noise reduction when the silver coil is cooled. On the right part of the figure, Hill (15) recorded a spectrum with a superconducting coil (top) and a room-temperature copper coil (bottom). The superconducting coil amplifies the signal, but no noise floor reduction is apparent. 12

Figure 2-1: Elements possessing an isotope exhibiting a fractional spin with dual-energy state, such as ^1H , are depicted in grey. Other elements can have more than two spin states, and some do not emit a nuclear magnetic resonance signal. [Figure reproduced from (26)]. 16

Figure 2-2: The misalignment of B_0 and μ causes a torque on the magnetic moment of the spin. Because the spin intrinsically possesses angular momentum, it precesses around B_0 to conserve the total angular momentum of the system. [Figure Reproduced from (27)] 18

Figure 2-3: A B_1 magnetic flux density irradiates the magnetization at the Larmor frequency. In a frame rotating around B_0 at the Larmor frequency, the B_1 field appears immobile and B_0 disappears (left part). B_1 applies a torque on the spin. Because the spin possesses angular momentum, it precesses around the vector B_1 . The same phenomenon is depicted from an laboratory reference frame (right).[Reproduced from (27) and modified] 20

Figure 2-4: a,d) The magnetization is the equilibrium state. The magnetization points along B_0 . The axis of the radiofrequency coil is along y. b,e) After the coil has emitted radiofrequency waves at the Larmor frequency, the magnetization has been tipped in the transverse plane. c,f) Because each spin feels the magnetic interaction of its neighboring spins, it feels a slightly different B_0 value and precesses at a slightly different frequency. As a consequence, the overall magnetic flux density of the magnetization, given by the vector-sum of all the spin magnetic moments, vanishes. The intensity of the vector M in the transverse plane decreases with time. [Figure reproduced

from (27)].....	22
Figure 2-5: the component M_z of the magnetization along B_0 regrows exponentially with time-constant T_1 . [Figure reproduced from (27)].....	23
Figure 2-6: The radiofrequency coil excites the spins (left) and tips the magnetization in the transverse plane. The magnetic flux created by the coil must be perpendicular to B_0 represented by the long vertical arrow. In a subsequent part of the magnetic resonance acquisition process, the coil collects the time-varying flux created by the precessing spins (right). [Figure reproduced from (27) and modified]	24
Figure 2-7: The energy flow from the radiofrequency coil emitting a pulse to excite the specimen, and back to the radiofrequency coil to be later sampled by the imager.....	25
Figure 3-1: (Left) electrically coupled components. The noise power depends on the sum of resistance of the components. (Right) magnetically coupled components. The noise power depends on the resistance of one component added to the impedance-transformed resistance of the other component. The mutual inductance M between the two inductors L_1 and L_2 determines the amplitude of the transformation (8).	33
Figure 3-2: The schematic shows the essential components of a superconducting Helmholtz pair. A segment of the second superconducting coil and heat exchanger is removed in this schematic to allow better appreciation of the geometry. The YBCO traces (1) are deposited on sapphire substrates (2) attached to ceramic heat exchangers (3) in thermal contact with titanium chambers containing flowing helium vapor. The coils are inductively coupled to the radiofrequency chain by an room-temperature circular copper coupling loop (4). The cartridge (5) containing the specimen (6) is placed at the center of the Helmholtz pair. A room-temperature copper foil is wrapped around the probe housing and acts as a radiofrequency shield. [Reproduced from (21)].....	34
Figure 3-3: The equivalent circuit of a magnetically coupled radiofrequency coil. The primary circuit (left) corresponds to the radiofrequency coil and all the losses it produces. The secondary circuit (middle) is comprised of the coupling loop magnetically coupled to the primary circuit. The equivalent circuit (right) contains noise from the secondary circuit, and transformed noise from the primary. It includes the secondary resistance, and the transformed primary resistance.	35
Figure 4-1: A mouse kidney acquired with low SNR by a copper probe (left) and with high SNR by a superconducting probe (right). [Figure reproduced from (16)].....	39
Figure 4-2: For a single-turn surface coil irradiating a semi-infinite specimen of conductivity 0.5 S/m, the line indicates sets of coil radius and operating frequency where the noise emitted by the specimen is equal to the noise emitted by the coil. The figure	

pertains to a room-temperature copper coil, a cold copper coil, and a superconducting YBCO with and without B_0 -induced change in coil noise properties. [Figure reproduced from (6)].....	43
Figure 4-3: Many imaging sequences excite a slab of magnetization (left) that emits signal. In volume encoding techniques sometimes used in microscopy (right), the entire volume is excited and more signal is collected by the coil. [Figure Reproduced from (33)]	45
Figure 4-4: Chemical structure of the macrocyclic, non-ionic gadolinium chelate Prohance (Bracco S.p.A., Milano, Italy). [Figure reproduced from (35)]	47
Figure 4-5: the three-dimensional gradient-recalled echo imaging sequence contains a non-selective hardpulse. The first part of the echo can be left unsampled to shorten echo time.	49
Figure 4-6: In a radial acquisition sequence, the sampling window is open as soon as the spatial encoding begin and the free induction decay of the spins submitted to gradients is recorded. The echo-time is extremely short, in the range of a few hundreds of microseconds.	50
Figure 6-1: (Right) A stack of circular sapphire substrates (1) lays on a square copper shield (2) 100 mm wide. The substrates exhibit a 38 mm outer-diameter, the two lower substrates are 1 mm thick, and the top one is 3 mm thick. The copper traces of the horse-shoe coil (3) measure 35 mm outer-diameter, and 13 mm inner-diameter, and are interrupted by a 2 mm wide gap. They are sandwiched between the substrates. A homogeneous spherical specimen (4), 15 mm in diameter, of known conductivity equal to 4 S/m lies at the center of the top surface of the thicker substrate. The coupling loop (5), measuring 28 mm outer-diameter and 24 mm inner-diameter, is matched to the radiofrequency chain and placed above the coils.	63
Figure 6-2: The input power sent to the model is 50 W. The model was solved 21 times with a mesh increasingly refined. The integrated input power measured inside the model is given on the horizontal axis. A measure in arbitrary unit of the relative finite-element size used during the computation ranged from 0.85 to 1.25 (y-axis on the right, dots on the graph). It can be seen that with smaller finite-elements, the integrated input power converges towards 50 W. The amount of unshared computer-processing-unit (CPU) time required by the computations ranged from 8 to 63 minutes (y-axis on the left, squares on the graph). The computation load grows exponentially with smaller finite-elements, but allows the solution to converge towards its true value. The oscillations in both curves are error caused by numerical noise.....	64
Figure 6-3: the insert (top right) shows the simple probe, the specimen and the coupling	

loop. The coupling loop was connected to a network analyzer so that the resonant frequency of the probe and its quality factor could be measured without shield and with a flat copper shield. Similarly, the separation distance between the coupling loop and the coil was recorded. 66

Figure 6-4: Transformed resistance of each probe component for the simple probe, without and with a shield. The hollow bar gives the total losses, which should amount to 50 Ω . Errors bars equal to $\pm 20\%$ indicate numerical error..... 72

Figure 7-1: The schematic shows the essential components of the beryllia probe. A segment of the second superconducting coil and heat exchanger is removed in this schematic to allow better appreciation of the geometry. The YBCO traces (1) are deposited on sapphire substrates (2) attached to beryllia heat exchangers (3) in thermal contact with titanium chambers containing flowing helium vapor. The coils are inductively coupled to the radiofrequency chain by a room-temperature circular copper coupling loop (4). The cartridge (5) containing the mouse brain specimen (6) is placed at the center of the Helmholtz pair. A room-temperature copper foil is wrapped around the probe housing and acts as a radiofrequency shield. [Reproduced from (21)] 75

Figure 7-2: A picture of the beryllia superconducting probe without its housing (left) and the radiofrequency model (right). The model includes the superconducting traces deposited on sapphire substrates, held in place against beryllia heat exchangers, as well as the coupling loop, a cylinder-shaped specimen, the cartridge and the radiofrequency shield. In the model, the probe housing and the titanium heat exchangers are not represented. The mouse brain is represented by a cylinder, 14mm in length and 8 mm in diameter, of conductivity equal to 0.7 S/m and relative permittivity equal to 50. 77

Figure 7-3: The superconducting coil (left) scored during the manual tuning process, and its radiofrequency model (right)..... 79

Figure 7-4: A detailed view of one spiral coil shows the pitch p of a spiral, and the trace width w . The inner radius r of the coil is measured to the midline of the inner trace. The spiral coil parameters are: $r=11.75\text{mm}$, $w=1\text{mm}$ and $p=1.65\text{mm}$. The superconducting coil substrate is a 38 mm outer diameter, 22 mm inner diameter, one-millimeter thick sapphire ring. The substrate of the copper replica coil is identical, but made out of a organic ceramic material of similar dielectric constant. Each coil resonates at 180 MHz as manufactured with an original number of turns of $N=2.875$. They can be brought to 410 MHz by reducing the number of turns to approximately 1.3. Data from a copper replica (o) is compared to tuning data from a superconducting coil after its manufacturing (\square), as well as simulations (dashed line). [Figure reproduced from (21)] 80

Figure 7-5: Experimental values of resonant frequency and impedance for a superconducting Helmholtz pair are compared to values predicted by the

radiofrequency model. [Figure reproduced from (21)] 81

Figure 7-6: sagittal and transverse sections of a homogeneous cylindrical phantom, 11mm in diameter and 23mm in length (excluding the lateral lid protrusion) filled with silicone oil, showing the signal intensity at the mid-line of the image. (a) Central longitudinal slice from the 3D array acquired with the HTS coil and signal intensity across the R/L direction for the HTS coil (solid line), through the center of the Helmholtz pair. The simulated B_1 field intensity is given by the dashed line. The coupling loop of the superconducting probe is located at position +20mm along the R/L axis. The element closer to the coupling loop, located at +6.5mm, carries more current and generates a higher B_1 field than the coil further away, placed at -6.5mm. (b) signal intensity across the A/P direction for the HTS coil (solid line) through the center of the Helmholtz pair, and simulated B_1 field intensity (dashed line). The imaging parameters are: GRE 90°, TR 500 ms, TE 5.5 ms, FOV 51.2x25.6x25.6 mm, Bandwidth 62.5 kHz, NEX 1, Voxel Size 200x200x200 micron. [Figure reproduced from (21)] 83

Figure 7-7: Image of octagonal piece of mesh fabric, clamped in a polymeric round clip, and immersed in copper sulphate (0.05 M) acquired with the beryllia probe. From a 1024^3 array, the selected imaging plane intersects the mesh with 20-micron openings along an arc on the left side of the image. The magnified section emphasizes dark regions of signal void delineating the mesh fibers. Bright dots mark the location of the mesh openings. The insert in the top-right corner shown the intensity profile acquired along line 1 placed perpendicular to the fibers. Two-pixel-wide peaks correspond to the position of the mesh openings falling within the imaging plane..... 87

Figure 7-8: (a) 20-micron thick transverse slice through the mouse hippocampus, at a 10-micron in-plane resolution. Both axes are phase-encoded. (b) In the hippocampus, transitions between layers (1, 2) are visible. The layering of the corpus callosum (3) is apparent. Signal-to-noise ratio is 18. (c, d) Hematoxylin and eosin histological section of a different brain at approximately the same location, for comparison. 88

Figure 8-1: A central alumina heat exchanger (1) cools down the radiofrequency coil (2). Lateral Alumina heat exchangers (3) cool the copper shield wrapped around the group of three alumina components. All alumina parts are in thermal contact with titanium heat exchangers (4). A polymeric housing (5) allows vacuum to be established around the coils. The cartridge (6) holding the specimen is placed at the center of the sample well (7). A resonant coupling loop (8) matches the probe to the radiofrequency chain. Four nitrogen lines (9) supply a flow of room-temperature nitrogen flowing around the cartridge to prevent it from freezing..... 91

Figure 8-2: The angular position of the single-sided substrate changes the resonant frequency of the assembly constituted by the double-sided substrate and the single-

sided substrate. For clarity, the two substrates are depicted apart from each other. Within the probe, they adhere to each other by interposition of a thin layer of thermal compound. The resonant frequency of the probe was recorded experimentally (\square). In practice, the thickness of the thermal compound layer strongly impacts the resonant frequency. The thickness of the layer was measured and then used as an input into the radiofrequency model. The resonant frequency of the probe predicted by the radiofrequency model (\bullet) is in good agreement with experimental values. 94

Figure 8-3: (a) perspective of the alumina probe. For clarity, one lateral alumina heat exchanger was removed. The cartridge (1) is placed within the sample well (2), at the center of the superconducting coils (3). (b) Side view of the alumina probe. The distance d between the inner edge of the superconducting trace and the outer edge of specimen (4) was kept as small as possible to maximize the filling factor. 98

Figure 8-4: (a,c) The layering of the cerebellum is apparent in the image acquired by the alumina superconducting probe. Signal-to-noise ratio ranges from 18 to 45. 102

Figure 8-5: To maximize the filling factor of the probe, the clearance between the coils and the sample well must be minimal which requires the precise alignment of all the probe components. Four screws (1) adjust the vertical position of the superconducting coils around the sample well. Four supplementary set-screws (2) adjust the horizontal position of the coils. Edges (3) were machined in the titanium heat exchangers to facilitate the correct alignment of the alumina components (4). Finally, shoulders (5) machined in the alumina heat exchangers make the alignment of the coils easier. Low thermal conductivity ceramic washers (6) limit the heat load towards the titanium heat exchangers. 106

Figure 8-6: Room-temperature components (red) do not shorten during the cooling of the probe. In contrast, components cooled below 60 K (blue) become up to 2 mm smaller. So that the superconducting coils travel a tolerable distance within the probe housing (1), a room temperature frame (2) is attached (3) to the cold components close to the center of the coils (4). A short length of titanium and alumina (D) limits the travel of the coils due to thermal contraction to less than 0.2 mm. 108

Figure 8-7: Severe artifacts due to microphonics are apparent in an image of 9-day mouse embryo, imaged at 11 μm isotropic resolution. 111

List of Abbreviations

AC	Alternating Current
CIVM	Center for In Vivo Microscopy
DC	Direct Current
FOV	Field-of-view
GRE	Gradient Recalled Echo
HTS	High-Temperature Superconducting
Q	Quality Factor
SNR	Signal-to-Noise Ratio
TE	Echo Time
TR	Repetition Time
T/R	Transmit / Receive
YBCO	Yttrium Barium Copper Oxide

Acknowledgments

As a student at the Center for In Vivo Microscopy, I would like to express my gratitude to my advisor Dr. G. Allan Johnson for creating, developing and supporting the CIVM, a scientifically thrilling and fantastically well-funded environment where a student can learn and poke around, discover and pursue his interests while being supported every step of the way. I would like to acknowledge my mentor for teaching me how to organize my thoughts and encourage me to look further ahead, for showing me how to design a purposeful experiment and pushing me at times, for explaining to me how to write meaningfully and hopefully, intelligibly. Finally, I would like to thank Dr. Johnson for consistently providing the scientific guidance and the support that I needed, and encouraging me along a career path that I love.

I would like to thank as well my committee for their interest in me and my project, and guiding me towards the completion of this research.

I am thankful to the graduate students at the CIVM for sharing with me their ups and downs, scientific or not, teaching me new skills, and for all our good times together. In particular, I would like to express my gratitude to Gabe Howles-Banerji for his explanations of physiology and medicine wrapped in undefeatable enthusiasm, as well as Alex Petiet for teaching me how to perfuse and fix specimens while speaking French to me. The researchers at the CIVM should find here the expression of my deep

appreciation: Gary Cofer and Brett Guenther for cheerfully teaching me almost everything I know about magnetic resonance hardware, Larry Hedlund for letting me handle small rodents, Boma Fubara for showing me with kindness how to carry out simple surgical procedures and how to identify neuroanatomy, alongside of Alexandra Badea. Finally, the remainder of the staff for our lively Friday afternoon seminars around beer and chips, attempting to tackle the meaning of life.

Taking a step back, I am aware that I found my way through graduate school in part thanks to my high-school and college friends in Europe. Together we discovered parts of the world, close and remote, but mostly ourselves. We fostered in each other a taste for learning and a friendship lasting to this day. My friends in North Carolina lead me to numerous adventures in Chapel Hill, trips, treks and gatherings. Together we tried to supplement fun with a curiosity for each other, and a desire for meaning.

I will keep the last paragraph for my family. I am immensely thankful to my parents for my education and caring for me. I am proud of my father for his journey from Graduate School before me to who he is today, and of my sister for choosing her own original path in life. I am grateful to my mother for always encouraging my endeavors, be they geographic, academic, professional or sentimental. Finally and foremost, Jason Chumley and I have lived happily together across two continents and loved each other for more than a decade. He is both my own tiny piece of sunshine and the hopping toad to whom this dissertation is dedicated.

1 Introduction

1.1 The Sensitivity of Magnetic Resonance Microscopy

Magnetic resonance imaging, demonstrated in 1973 by Lauterbur and Mansfield (1,2), revolutionized the field of medical imaging. It is non-ionizing, three-dimensional, non-destructive and benefits from a rich contrast that can be modified to fulfill the need of the user. Similarly, magnetic resonance microscopy is now having a profound impact on basic sciences across the biological field. It allows scientists to study fundamental biology, be it on a plant, a small rodent or a zebrafish, understand physiology and disease models, record pathologic progression and develop therapeutic approaches.

Scaling down magnetic resonance imaging to smaller specimens presents its own set of challenges. A 20-g mouse is 4000 times smaller than a 80-kg human. To preserve the relative definition of the smaller organs of the mouse during imaging, the voxel volume must be decreased by a factor 4000. Consequently the signal in magnetic resonance microscopy can be 4000 times as weak as the signal in clinical magnetic resonance imaging.

Several techniques are used to compensate the low sensitivity of magnetic resonance microscopy. Presently, studies can take place at a field as high as 17.4 T (3), in

principle providing a higher signal. Contrast agents can be infused into fixed tissues or injected into living organisms prior to imaging to enhance signal. Specific imaging sequences, sometimes including volume encoding, can increase the signal-to-noise ratio (SNR) further. Even so, the crucial and most important technique implemented to compensate the low sensitivity of magnetic resonance microscopy is the use of high-sensitivity radiofrequency probes. They can increase the SNR, presently the major factor limiting imaging performance, increase imaging efficiency, and ultimately expand the boundaries of magnetic resonance microscopy.

1.2 The Meaning of a High-Sensitivity Probe

This section clarifies the relation between probe sensitivity and SNR. It identifies the common physical traits of “high-sensitivity” probes: high filling factor and high quality factor, low equivalent resistance and low noise temperature.

The signal-to-noise ratio available in a magnetic resonance experiment has been presented by Hoult and Richards (4) for a lossless specimen irradiated by an homogeneous coil acting as the only source of noise. Later, Hoult and Lauterbur (5) included a conducting specimen inserted in the same coil. The signal-to-noise relation (6) below encompasses noise stemming from the specimen, the coil and multiple probe components. Obviously, a magnetic resonance user wants to maximize the SNR

recorded:

$$SNR \approx F^{-1/2} \frac{\omega_0(B_1 / I)}{\sqrt{4kR_{eq}T_{eq}}} VM_T \sqrt{\frac{t_w}{t_r}} \sqrt{t_{scan}} \quad (1-1)$$

where F is the noise factor accounting for the supplementary noise power added to the signal by the scanner electronics, V is the volume of a voxel containing the transverse magnetization M_T , t_w is the duration of the sampling window, t_r is the repetition time and t_{scan} is the total scan duration. The product $R_{eq}T_{eq}$ is an equivalent temperature-weighted sum or resistances defined by the respective power dissipation rate and temperature of all the components of the probe, as well as the specimen. Under the assumptions made by Hoult and Richards (4), including a lossless specimen, a uniform multi-turn solenoid coil exhibiting no current inhomogeneity, and a single source of noise stemming from the coil, the product $R_{eq}T_{eq}$ is such that the SNR exhibits a $\omega^{7/4}$ dependency. Part of the scope of this dissertation is to relax those assumptions and include noise originating from multiple probe components.

The parameters contributing to signal detection, and defining the probe sensitivity, are gathered below:

$$S \approx \frac{\omega_0(B_1 / I)}{\sqrt{4kR_{eq}T_{eq}}} \quad (1-2)$$

where S is the probe sensitivity, ω_0 is the Larmor angular frequency, B_1 is the magnetic flux density created by the probe carrying a current of intensity I , k is Boltzmann's constant.

To further express the probe sensitivity based on values reported in literature, we make the fundamental assumption that the B_1 field created by the probe is homogeneous over the internal volume of the probe. Consequently (6):

$$S \approx \sqrt{\frac{\mu_0 \omega_0 \eta Q}{4kR_{eq}T_{eq}V_s}} \quad (1-3)$$

where μ_0 is the magnetic permeability of free space, η is the filling factor defined as the ratio of the magnetic energy stored in the specimen of volume V_s to the magnetic energy stored in the probe. Q is the quality factor of the probe, defined to be equal to $\omega L_{equ}/R_{equ}$, and L_{equ} is the amount of magnetic energy stored in the coil per unit of current.

The equations above enable us to draw three important conclusions. First, SNR is proportional to the sensitivity of the probe. To maximize SNR, we will attempt to maximize the probe sensitivity. Secondly, in high-sensitivity probe, the product ηQ must be maximized, indicating that the specimen should occupy most of the probe internal volume where the magnetic field is high, and that the probe quality factor must be high.

And thirdly, in a high-sensitivity probe, the product $R_{\text{equ}}T_{\text{equ}}$ must be minimized, indicating that conducting components in the probe may benefit from being cold, and should show a resistance as small as possible.

We will see in the next chapter that the discovery of high-temperature superconductivity sparked enthusiasm and excitement in the magnetic resonance community: superconductors may fulfill the requirements above, foretell an increased probe sensitivity and higher SNR...

1.3 The Discovery of High-Temperature Superconductivity

Discovered in 1986 by J. Georg Bednorz and K. Alex Muller, high-temperature superconductors are ceramics containing copper planes along which electrons can move freely in the superconducting state, reached above 77 K. They exhibit no direct current (DC) resistance, and an extremely low alternating current (AC) resistance when the superconducting state is reached. Used in a magnetic resonance microscopy probe, a superconducting coil exhibits a negligible AC resistance, a low temperature, a quality factor several orders of magnitude higher than regular conductors, and consequently presents a stunning potential at increasing the probe sensitivity and SNR.

1.4 High-Sensitivity Cryogenic Probes

In the last twenty-five years, several research groups have produced a high-sensitivity cryogenic probe using cold conductors or superconductors. In the next few paragraphs, we will elaborate on the recurring theme emerging from the published literature: high-sensitivity probes record a significant SNR gain experimentally (7-24); however, the SNR gain is lower than theoretically predicted (16,17,19,22,23), and the performance of at least one component of the probe is unexpectedly poor (8,16-19,21-23,25).

Several investigators attempted to develop high-sensitivity probes before the discovery of high-temperature superconductivity. In 1984, Styles et al. (23) described a silver-wire, saddle-shaped, Helmholtz pair for carbon spectroscopy at 4.3 T. Both the coil and the preamplifier were cooled to 4.3 K. A 7-fold increase in SNR was reported, whereas theoretical analysis forecasted a factor of 17. The authors emphasized that "the results that we have achieved so far show a disappointing discrepancy between the predicted and realized improvement in sensitivity due to cooling. We appreciate that there are several mechanisms which could account for this, including inductive coupling between the coils and the surrounding conducting materials, [...]". In 1987, Damico et al. (11) presented a dual-tuned spectroscopy probe in which the tuning inductor was cooled to liquid nitrogen temperature. They demonstrated an SNR gain of 1.12 for proton and

1.35 for phosphorus. In 1988, Hall et al. (13) described a three-loop copper surface coil cooled to liquid nitrogen temperature for human imaging at 0.15 T. The SNR gain ranged from 1.25 to 2.1 when cooling the coil.

After the early attempts at developing high-sensitivity cold conducting probes in the eighties, superconducting films became available to magnetic resonance microscopists at the beginning of the nineties. Yttrium-barium-copper-oxide (YBCO), a high-temperature superconductor, can be deposited on a flat substrate of lanthanum aluminate or sapphire. YBCO coils tend to exhibit a quality factor several orders of magnitude higher than regular copper coils. Several high-sensitivity superconducting probes were produced, at times exhibiting a quality factor more than two orders of magnitude larger than comparable copper probes. In 1991, Hall et al. (14) modified their cold copper probe to accommodate a superconducting surface coil. They reported a superconducting quality factor of 2500, as compared to 500 for an identical copper probe cooled to liquid nitrogen temperature. In 1993, Black et al. (7) reported a superconducting quality factor of 60'000, 150 times as large as the quality factor of a comparable copper probe, equal to 400. The next figure illustrates the impressive ability of superconducting probes to exhibit a much larger quality factor than copper probes.

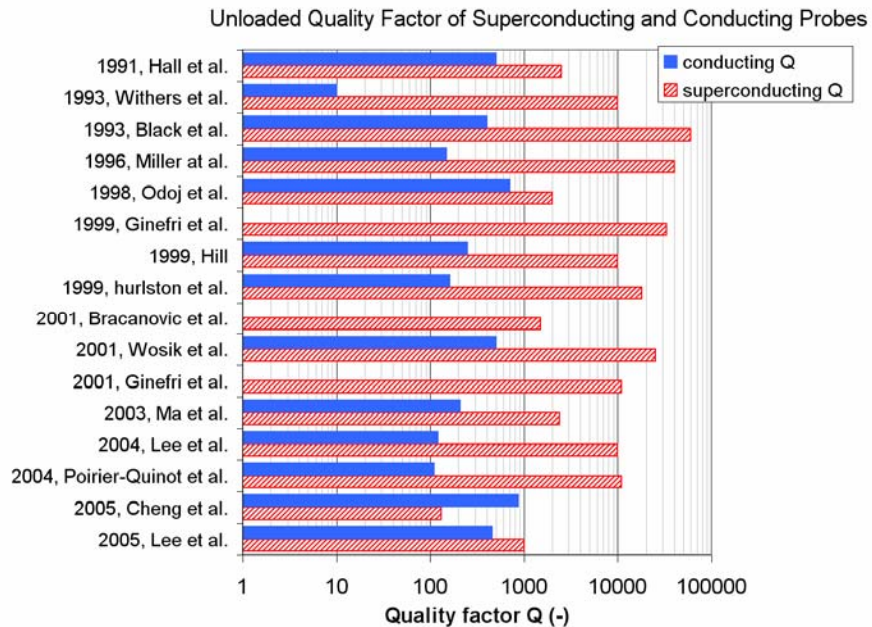


Figure 1-1: Several research group have produced a superconducting probe between 1991 and 2008. The logarithmic graph shows the unloaded quality factor of the superconducting probes (filled), comparable copper probe (hatched), and illustrates the ability of superconducting probes to exhibit a much larger quality factor than copper probes.

The high quality factor of superconducting probes lead to significant gains in sensitivity and SNR. Although the SNR gain was fairly large, it was smaller than expected by most authors who speculated that some probe components may be deleterious to sensitivity and SNR. Black et al. (7) reported an SNR gain of 10, and included a theoretical prediction of 60. The authors pointed out (25) that "we do not know if the loss tangent of LaAlO_3 (lanthanum aluminate), radiative loss, or the surface resistance of the YBCO is setting the current zero-field limit on Q". They suspected that the experimental SNR gain was due to the increase in quality factor without any benefit

from the lower noise temperature. They hypothesized that a room-temperature shield may couple noise to the probe and degrade its SNR performance, and that the preamplifier may add significant amounts of noise to the recorded signal.

In 1998, Odoj et al. (22) presented a probe using a YBCO horse-shoe surface coil. The probe included a cooled radiofrequency shield at 80 K. The coil itself operated at 30 K and exhibited outside the probe an unloaded quality factor of 12'000, which degraded to 2000 when the coil was inserted into the probe. The authors compared the superconducting probe to the same copper coil at 48 K. The experimental SNR gain was 3.1 with a water sample, as compared to 4.6 predicted theoretically. With a conducting MnCl_2 sample, the experimental SNR gain was 1.9 as compared to 1.7 forecasted by theory. The authors underlined that the lower-than-expected homogeneity of the superconducting resonator may explain the SNR gain discrepancy and concluded that "with increased coil sensitivity, inductive coupling to conducting parts of the probe can deteriorate the noise properties."

1.5 The SNR Discrepancy

Figure 1-2 gathers the SNR gain published by several groups using a superconducting probe. For the few authors who included SNR predictions, the SNR recorded experimentally was generally lower than theory. The SNR gain missing experimentally can be visualized on the graph.

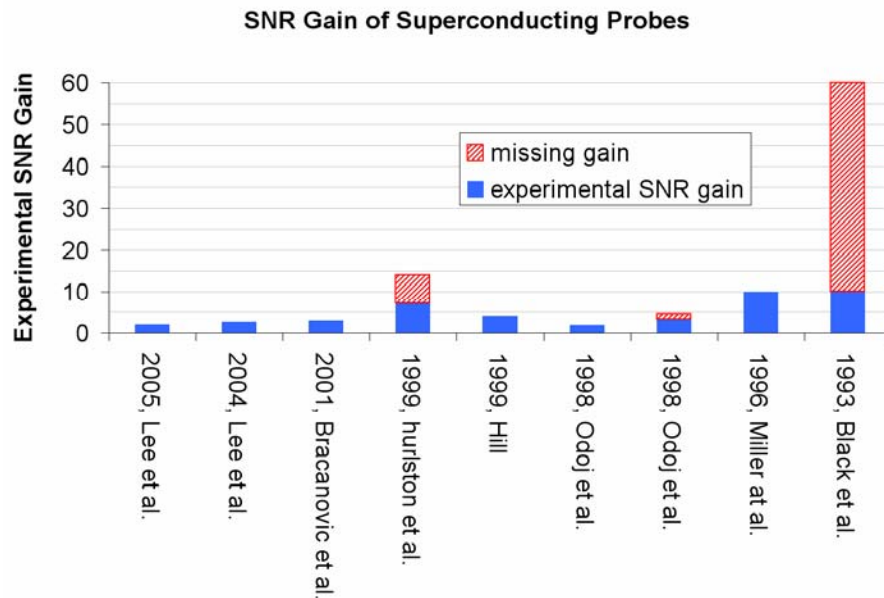


Figure 1-2: Several research groups reported an SNR gain by using a superconducting probe (full). Some authors reported a theoretical SNR, often largely exceeding the experimental SNR. The SNR gain missing experimentally is given by hatched blocks.

Most investigators attempted to identify the cause of the incomplete SNR gain recorded experimentally. Ma et al. (19) acknowledged that "all empirical (SNR) gains [...] are well below the theoretical gains" In fact, all authors faced an SNR gain discrepancy, excepted Odoj et al. (22) in one specific case. Hurslton et al. (16) commented "the entire SNR gain of 7 stems from signal amplification, since negligible reduction in the noise floor is attained." The same situation applied to Hill (15). Similarly, other research groups imputed the SNR gain discrepancy to additional noise, originating from the insufficient noise performance of the preamplifier (17,19,25), from the "system" (10), or from coupling to the radiation shield (9,16,21,22,25). They also pointed at a low filling factor (15,19), signal attenuation due to the filtering effect of a high-Q resonator (17), or a decrease in superconductivity due to overheating (17).

Figure 1-2 illustrates the difficulty that most investigators faced at harvesting the entire SNR gain from superconducting probes. One or several components of the cryogenic probe, generally uncertainly identified, inject deleterious amounts of noise into the probe or limits the quality factor to the detriment of overall sensitivity and SNR.

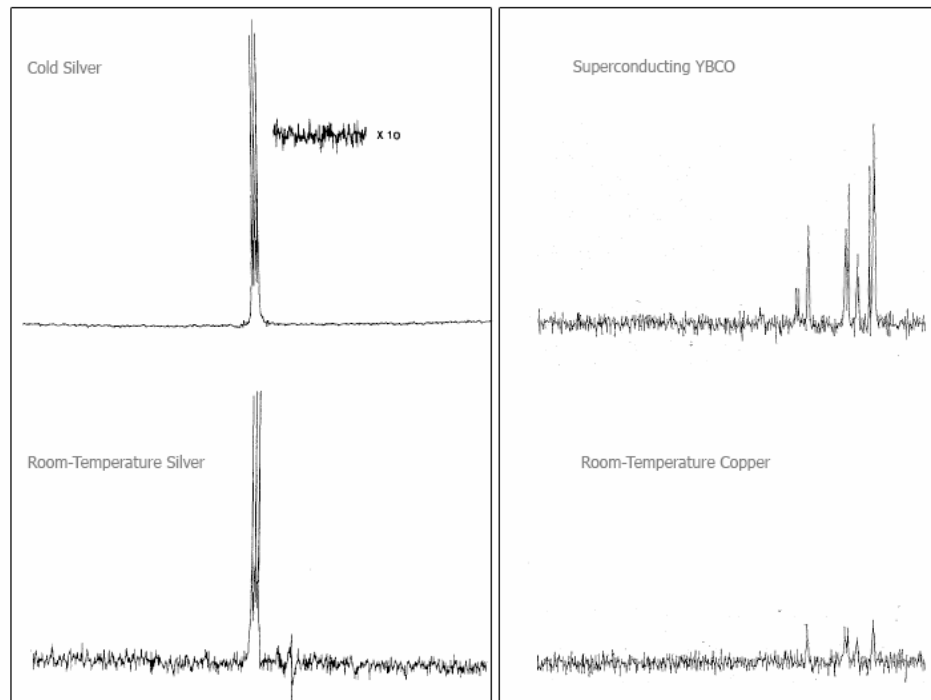


Figure 1-3: On the left part of the figure, the spectrum recorded by Styles (23) shows both signal amplification and noise noise reduction when the silver coil is cooled. On the right part of the figure, Hill (15) recorded a spectrum with a superconducting coil (top) and a room-temperature copper coil (bottom). The superconducting coil amplifies the signal, but no noise floor reduction is apparent.

In conclusion to this review of cryogenic probes for magnetic resonance microscopy, published research has demonstrated the high-sensitivity of superconducting probes and their ability to record high levels of SNR. The SNR gain recorded experimentally, however, is incomplete. The reason for that SNR discrepancy has yet to be properly explained. We formulate the hypothesis that first, the SNR models may be insufficient. As a consequence, they should be expanded until they correctly predict experimental SNR gain. Secondly, superconducting probes may be built

imperfectly and do not deliver all the SNR gain physically possible. Their limitations should be identified and if possible, remedied.

This dissertation, for the first time to our knowledge, analyzes the sensitivity of a superconducting probe systematically, including all of its components. The method predicts SNR gains and evaluates the individual impact on sensitivity of every probe component. We can then identify components deleterious to SNR and possible remedies.

1.6 Aims of the Dissertation

We present an original, detailed model of superconducting probes *at the component level*. Our systematic analysis encompasses all the individual components of a superconducting probe: the superconducting coil and its substrate, the complex geometry of dielectric materials surrounding the probe, the specimen, the radiofrequency shield, and the magnetic coupling to the radiofrequency chain. The model calculates the probe sensitivity holding into account *every* component, as well as the common figures of merit pertaining to a radiofrequency coil. Specifically, we deliver an estimate of: i) the coil resonant frequency, ii) the impedance, iii) the homogeneity, iv) the filling factor and v) the sensitivity.

In addition, we deliver the individual contribution of each probe component to the overall noise detrimental to SNR. The detailed understanding of the transmission of signal and noise between components enables us to identify deleterious components of the probe and offers remedies.

Finally, we apply our original analysis to the design a new superconducting probe, maximizing its sensitivity and the SNR it records. We use the probe for the imaging of a mouse cerebellum, ultimately increasing the imaging performance of magnetic resonance microscopy.

2 The Signal

This section describes the physical properties that determine the magnetic resonance signal intensity. The mechanisms by which the signal appears and decays will be described. Then, we focus on the crucial role of the radiofrequency probe in both transmitting energy to the specimen and acquiring the signal emitted by the specimen, estimating the efficiency of the signal transmission process.

2.1 The Nuclear Magnetic Resonance Phenomenon

Isotopes possessing an odd number of nucleons exhibit a fractional spin, and emit a nuclear magnetic resonance signal. Some are illustrated in Figure 2-1 (26). For concision, only ^1H will be discussed further. It exhibits a spin with dual-energy state, the source of signal in most magnetic resonance experiments including ours.

		Spin: 1/2 3/2 5/2 7/2 9/2 1 3 5 6																									
IA																	O										
H	D	IIA														III A	IV A	V A	VIA	VII A	He						
Li	Li	Be															B	B	C	N	N	O	F	Ne			
Na	Mg	IIIB		IVB	VB	VIB	VII B	VIII		IB	IIB	Al	Si	P	S	Cl	Cl	Ar									
K	K	Ca	Sc	Ti	Ti	V	V	Cr	Mn	Fe	Co	Ni	Cu	Cu	Zn	Ga	Ga	Ge	As	Se	Br	Br	Kr				
Rb	Rb	Sr	Y	Zr	Nb	Mo	Mo	Tc	Ru	Ru	Rh	Pd	Ag	Ag	Cd	Cd	In	In	Sn	Sn	Sb	Sb	Te	Te	I	Xe	Xe
Cs	Ba	Ba	La	La	Hf	Hf	Ta	W	Re	Re	Os	Os	Ir	Ir	Pt	Au	Hg	Hg	Tl	Tl	Pb	Bi					

Figure 2-1: Elements possessing an isotope exhibiting a fractional spin with dual-energy state, such as ^1H , are depicted in grey. Other elements can have more than two spin states, and some do not emit a nuclear magnetic resonance signal. [Figure reproduced from (26)].

The spin of a hydrogen nucleus can be envisioned by two intrinsic vectorial quantities: the angular momentum \vec{L} and the magnetic moment $\vec{\mu}$. Both vectors are parallel. The vector of angular momentum gives the spin some gyroscopic properties, while the magnetic moment make the spin behave like a magnetic dipole. As a consequence, the dynamic behavior of a spin is particularly interesting when it is subjected to a torque created by an external magnetic field. It is the subject of the few paragraphs below.

2.2 Spin Dynamics

The angular momentum and the magnetic moment of a spin are colinear vectors:

$$\vec{\mu} = \gamma \vec{J} \quad (2-1)$$

where $\vec{\mu}$ is the spin magnetic moment, \vec{J} its angular momentum, and γ is the gyromagnetic ratio, a property of the isotope predicted theoretically from first principles and found experimentally.

Angular momentum is conserved within a system. Similarly to a gyroscope precessing in a gravity field, a spin immersed in an external magnetic field is submitted to a magnetic torque, and consequently precesses around the magnetic field:

$$\frac{d\vec{\mu}}{dt} = \gamma \vec{\mu} \times \vec{B}_0 \quad (2-2)$$

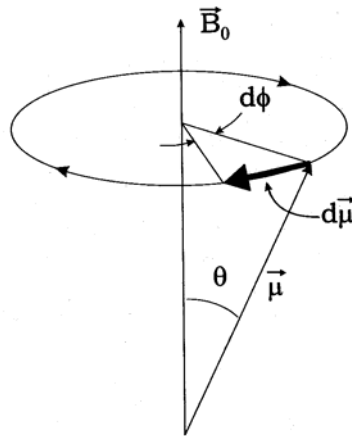


Figure 2-2: The misalignment of B_0 and μ causes a torque on the magnetic moment of the spin. Because the spin intrinsically possesses angular momentum, it precesses around B_0 to conserve the total angular momentum of the system. [Figure Reproduced from (27)]

The angular frequency of the precessing spin is the Larmor frequency ω_0 :

$$\omega_0 = \gamma B_0 \quad (2-3)$$

2.3 The Magnetization

The magnetization is the vector-sum of each magnetic moment among a group of spins. Like $\vec{\mu}$ and \vec{B}_0 , magnetization is a vector of magnetic flux density. When all the spins are at thermal equilibrium, the magnetization vector is aligned with B_0 and its value is given by:

$$M_0 = \frac{\rho_0 \gamma^2 \hbar^2}{4kT} B_0 \quad (2-4)$$

where M_0 is the longitudinal component of the magnetization at equilibrium, ρ_0 is the spin density, \hbar is the reduced Planck constant, k is Boltzmann's constant, T is the absolute temperature of the specimen. It is possible to tip the magnetization out of alignment with B_0 by irradiating it at the Larmor frequency.

2.4 The Flip Angle

When the magnetization is irradiated with a magnetic flux density B_1 , at the Larmor frequency, perpendicularly to the holding field, B_0 disappears in a reference frame rotating at the angular resonance frequency ω_0 . In contrast, B_1 seems immobile. The B_1 vector creates a torque on the spin, which consequently rotates around the support of B_1 (left part of Figure 2-3). In the laboratory reference frame, the trajectory of the tip of the magnetic moment is illustrated in the right part of the figure. By irradiating the specimen at the resonant Larmor frequency with a radiofrequency pulse, the magnetization can be partially or completely tipped into the plane transverse to B_0 .

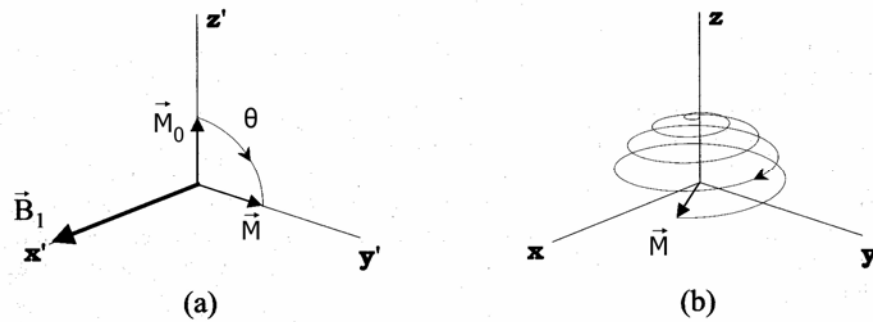


Figure 2-3: A B_1 magnetic flux density irradiates the magnetization at the Larmor frequency. In a frame rotating around B_0 at the Larmor frequency, the B_1 field appears immobile and B_0 disappears (left part). B_1 applies a torque on the spin. Because the spin possesses angular momentum, it precesses around the vector B_1 . The same phenomenon is depicted from an laboratory reference frame (right).[Reproduced from (27) and modified]

The magnetization tipping angle is the flip angle:

$$\theta = \gamma B_1 \tau \quad (2-5)$$

where θ is the flip angle, and τ is the duration of the radiofrequency pulse.

2.5 T₂ Decay

When the spins are tipped away from alignment with B_0 , they do not all precess in phase. Each spin feels the magnetic influence of its neighboring spins, slightly distorting the value of the holding field. Consequently, each spin precesses at a slightly different frequency, and the vector-sum of the magnetic moment of all the spins vanishes, in turn making the time-varying magnetic flux sensed by the coil decay exponentially with time-constant T_2 .

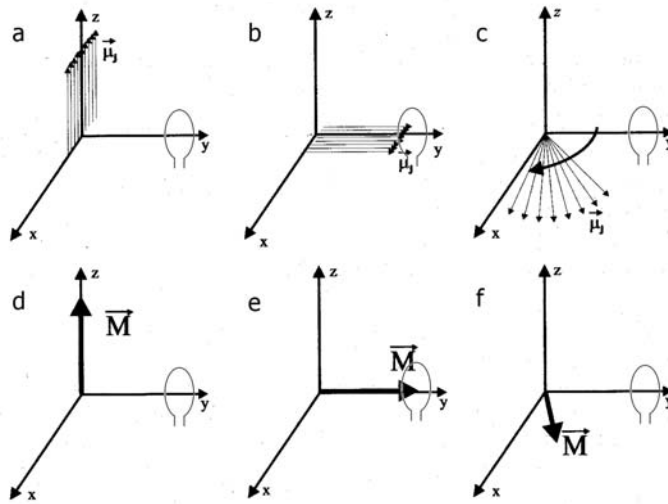


Figure 2-4: a,d) The magnetization is the equilibrium state. The magnetization points along B_0 . The axis of the radiofrequency coil is along y . b,e) After the coil has emitted radiofrequency waves at the Larmor frequency, the magnetization has been tipped in the transverse plane. c,f) Because each spin feels the magnetic interaction of its neighboring spins, it feels a slightly different B_0 value and precesses at a slightly different frequency. As a consequence, the overall magnetic flux density of the magnetization, given by the vector-sum of all the spin magnetic moments, vanishes. The intensity of the vector M in the transverse plane decreases with time. [Figure reproduced from (27)]

The component M_{xy} of the magnetization in the transverse plane exhibits an exponential decay of time-constant T_2 :

$$M_{xy} = M_z e^{-t/T_2} \quad (2-6)$$

where t is time, and M_z is the longitudinal component of the magnetization before the radiofrequency pulse.

The T_2 decay includes spin-spin magnetic interactions only. In practice, supplementary spin dephasing occurs because the B_0 field is inhomogeneous. In addition, interfaces between material of different magnetic susceptibility can abruptly change the value of the applied field. As a consequence, the actual decay time-constant T_2^* measured in practice is shorter than T_2 .

2.6 T_1 Recovery

When the magnetization has been tipped in part into the transverse plane, the spins realign themselves with B_0 during a non-instantaneous process. T_1 is the inverse of the rate at which the recovery of the longitudinal magnetization takes place:

$$M_z = M_0(1 - e^{-t/T_1}) \quad (2-7)$$

where M_z is the longitudinal component of the magnetization, along B_0 , illustrated below.

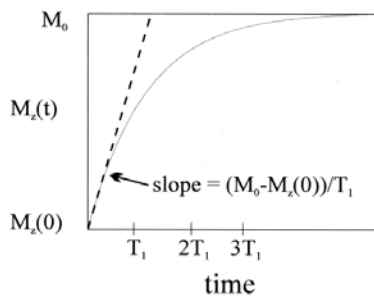


Figure 2-5: the component M_z of the magnetization along B_0 regrows exponentially with time-constant T_1 . [Figure reproduced from (27)].

2.7 Signal Transfer and Dissipation Within The Probe

The transmission of the signal within the probe deserves a thorough attention. The signal acquisition process conducted by a radiofrequency coil can be viewed as a series of lossy energy transfers. The figure below shows the same radiofrequency coil used both to irradiate the specimen and later sense the emitted magnetic resonance signal.

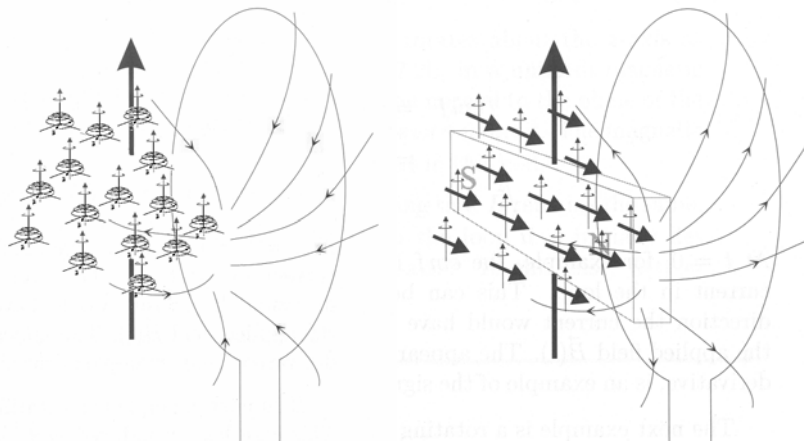


Figure 2-6: The radiofrequency coil excites the spins (left) and tips the magnetization in the transverse plane. The magnetic flux created by the coil must be perpendicular to B_0 represented by the long vertical arrow. In a subsequent part of the magnetic resonance acquisition process, the coil collects the time-varying flux created by the precessing spins (right). [Figure reproduced from (27) and modified]

First, the radiofrequency pulse is transmitted to the coil in the form of a radiofrequency wave of voltage and current traveling along a scanner cable. The current flowing in the coil induces a magnetic flux density B_1 , that tips the magnetization into

the transverse plane. Simultaneously, the coil and the specimen dissipate some power in the form of heat, and other losses take place in the surrounding probe components.

Secondly, the excited magnetization creates a time-varying magnetic flux density that induces an electromotive force, and consequently a current, in the coil. The same losses occur: the coil temperature increases, and the coil transfers power to surrounding components.

Finally, the current established in the coil travels down the scanner cable and constitutes the magnetic resonance signal sampled by the imager. Strictly, some losses occur as well during that step; they will not be described in this dissertation.

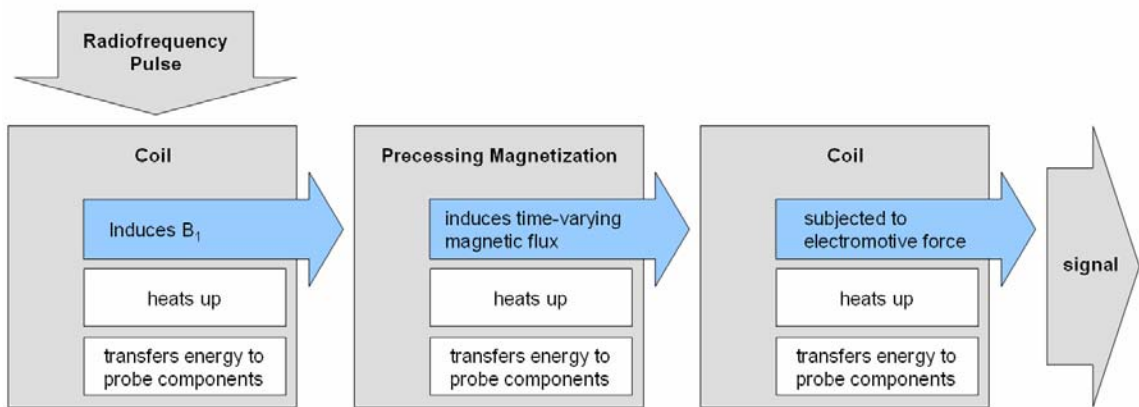


Figure 2-7: The energy flow from the radiofrequency coil emitting a pulse to excite the specimen, and back to the radiofrequency coil to be later sampled by the imager.

The efficiency of the energy transfer between coil and specimen can be determined by comparing the magnetic energy deposited into the specimen to the magnetic energy created by the probe. The reciprocity theorem (4) implies that the efficiency of transfer back to the coil is identical.

The magnetic part P_M of the power delivered to the specimen of volume V_{sp} is:

$$P_M = \frac{\mu}{4} \int_{V_{sp}} \vec{H} \cdot \vec{H}^* dV = \frac{\mu}{4} \int_{V_{sp}} |\vec{H}|^2 dV = \frac{1}{4\mu} \int_{V_{sp}} |\vec{B}_1|^2 dV \quad (2-8)$$

In magnetic resonance microscopy, only the component of H perpendicular to B_0 is useful. Therefore the part of magnetic energy deposited into the specimen and useful for imaging is:

$$P_{Mxz} = \frac{\mu}{4} \int_V |\vec{H}_{xy}|^2 dV \quad (2-9)$$

The magnetic energy created by the probe is:

$$P_{M0} = \frac{\mu}{4} \int_{all\ space} |\vec{H}|^2 dV \quad (2-10)$$

Finally, the efficiency of the probe at depositing magnetic power into the specimen is expressed by the filling factor η :

$$\eta = \frac{P_{My}}{P_{M0}} \quad (2-11)$$

Numerical simulations presented later estimate the electromagnetic coupling between component, calculate the power dissipated by each component, estimate the amount of magnetic power transferred to the specimen, and evaluate the signal transmission efficiency of the probe.

3 The Noise

We will describe the origin of the noise contaminating the magnetic resonance experiment. As we have seen in the last chapter, magnetic resonance is an electromagnetic phenomenon where signal can be sensed and transmitted by electrical conductors or superconductors. Unavoidably, every conducting body transmitting the signal creates some amount of supplementary noise degrading the signal. To understand the noise behavior of the probe, we will estimate the amount of noise that each conducting component emits, which will require us to estimate its resistance. The analysis will lead to techniques that may be used to limit noise levels.

3.1 Thermal Noise

Within a conductor, random atomic motion due to heat causes electronic motion, called thermal noise. Thermal noise exhibits the behavior (28,29):

$$N = \sqrt{4kTRB} \quad (3-1)$$

where N is the standard deviation of the noise voltage, k is Boltzmann's constant, T is the absolute temperature of the conductor, R its resistance, and B the reception bandwidth. A salient property of thermal noise power is its proportionality to both temperature and resistance. Superconductors exhibit the potential of very low noise

emission, precisely because their temperature is low and their resistance is infinitesimally small. To infer the amount of thermal noise emitted by a probe component, we will need to measure its temperature and determine its resistance.

3.2 Estimating Resistance

We have seen that in order to calculate the noise power of a probe component, we need to estimate its resistance. Several approaches are possible. The first method, analytical in nature and presented below, makes geometric assumptions that may fail to conform to reality. As a consequence, the calculated resistance value can significantly differ from the true resistance. The second approach, released from any geometric assumption, relies on a more robust energy argument and the resistance value can be estimated numerically.

3.2.1 Analytical Estimation

Electromagnetic waves, and the current that they induce, are rapidly attenuated in a normal conductor. Effectively, only a fraction of the conductor cross-section is available for conduction, which increases the resistance of the conducting body. The depth at which the current has decreased to $1/e$ of its original value at the conductor surface is called skin-depth δ :

$$\delta = \sqrt{\frac{2}{\omega\mu\sigma}} \quad (3-2)$$

where ω is the angular frequency of the wave, μ is the magnetic permeability of the conductor and σ its DC conductivity. When frequency increases, skin depth decreases and the resistance presented by the conductor increases.

The AC resistance R of a conductor can be estimated by:

$$R = \frac{\rho L}{\delta W} \quad (3-3)$$

where ρ is the resistivity of the material, L is the length of the conducting path and W its width.

In radiofrequency practice, currents along conductors are inhomogeneous which makes the conducting path and cross-section difficult to identify accurately. Consequently, the length and width of the actual conducting path of a conductor are imprecisely known. The calculated resistance value can significantly differ from the true resistance, for example by a factor of 3 (4).

3.2.2 Dissipated Power

A more robust way to estimate the resistance of a component is to equate its resistance R to the amount of power P_{1A} dissipated by the conductor submitted to a one-ampere current:

$$R = P_{1A} \quad (3-4)$$

where current and power are root-mean-square values.

The materials in the probe are electromagnetically lossy and exhibit a permittivity described by a complex number. We introduce the loss tangent $\tan L$, that expresses the ratio of the dissipated current over the transmitted current in a lossy medium (30):

$$\varepsilon = \varepsilon' - j\varepsilon'' = \varepsilon_0 \varepsilon_r (1 - j \tan L) \quad (3-5)$$

$$\tan L = \frac{\omega \varepsilon''}{\omega \varepsilon'} + \frac{\sigma}{\omega \varepsilon'} \quad (3-6)$$

where ε_0 is the permittivity of vacuum, ε_r is the relative permittivity of the medium, ε' and ε'' are the real and imaginary part of the medium's permittivity, respectively. The first right-hand term of the loss tangent is the dielectric loss tangent, and corresponds to dielectric losses within the component. The second right-hand term

corresponds to conductivity losses in the component. The power dissipated by a probe component of volume V is (30):

$$P_L = \frac{\sigma}{2} \int_V |\vec{E}|^2 dV + \frac{\omega}{2} \int_V \left(\epsilon'' |\vec{E}|^2 + \mu'' |\vec{H}|^2 \right) dV \quad (3-7)$$

The first right-hand term represents the losses due to the conductivity of the probe component, the second term represents the dielectric losses within the probe component. The third term is the magnetic loss within the component. From now on, we will assume that they are nil. Hence, losses are limited to conduction and dielectric dissipation, depending on the square of the electric field:

$$P_L = \frac{\sigma + \omega\epsilon''}{2} \int_V |\vec{E}|^2 dV \quad (3-8)$$

The power dissipated by every probe component can be calculated numerically.

3.3 Coupled Noise

Because the probe components are electrically and magnetically coupled to each other, they exchange noise with each other. Noise is additive. A well-performing component may see its noise performance degraded by extraneous noise induced by another component.

The figure below illustrate the amount of noise emitted by two components coupled with each other, electrically or magnetically.

$$N_{tot} = \sqrt{4k(T_1 R_1 + T_2 R_2)} B$$

$$N_{tot} = \sqrt{4k \left(\frac{\omega^2 M^2 T_1}{R_1} + T_2 R_2 \right)} B$$

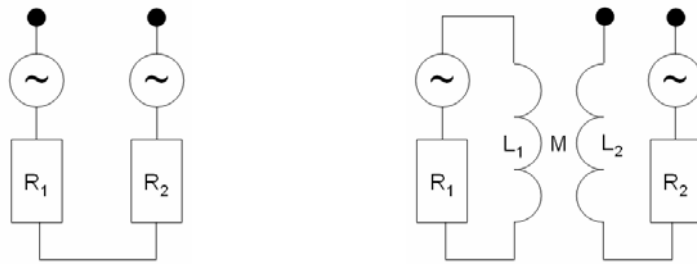


Figure 3-1: (Left) electrically coupled components. The noise power depends on the sum of resistance of the components. (Right) magnetically coupled components. The noise power depends on the resistance of one component added to the impedance-transformed resistance of the other component. The mutual inductance M between the two inductors L_1 and L_2 determines the amplitude of the transformation (8).

The entire probe is constituted by a number of different components, each of which is coupled to some degree to all the others. At this point, a more detailed presentation of the probe main components is informative.

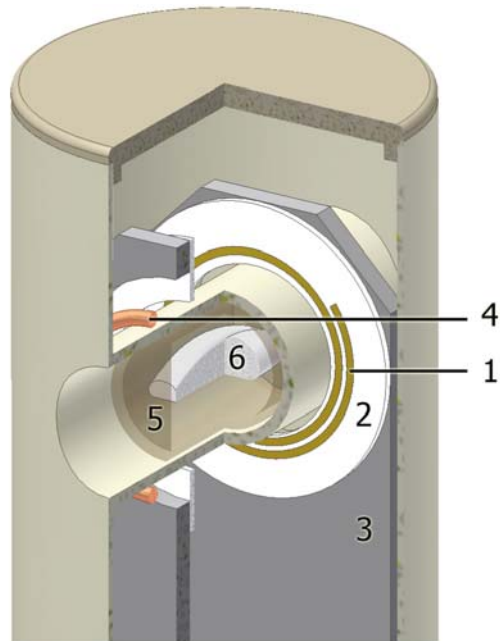


Figure 3-2: The schematic shows the essential components of a superconducting Helmholtz pair. A segment of the second superconducting coil and heat exchanger is removed in this schematic to allow better appreciation of the geometry. The YBCO traces (1) are deposited on sapphire substrates (2) attached to ceramic heat exchangers (3) in thermal contact with titanium chambers containing flowing helium vapor. The coils are inductively coupled to the radiofrequency chain by a room-temperature circular copper coupling loop (4). The cartridge (5) containing the specimen (6) is placed at the center of the Helmholtz pair. A room-temperature copper foil is wrapped around the probe housing and acts as a radiofrequency shield. [Reproduced from (21)]

3.4 Noise Transmission within a Probe

Magnetic coupling between the radiofrequency coil and the coupling loop corresponds to an impedance transformation (8). All the sources of noise contaminating the radiofrequency coil circuit are transferred to the coupling loop with a change in amplitude.

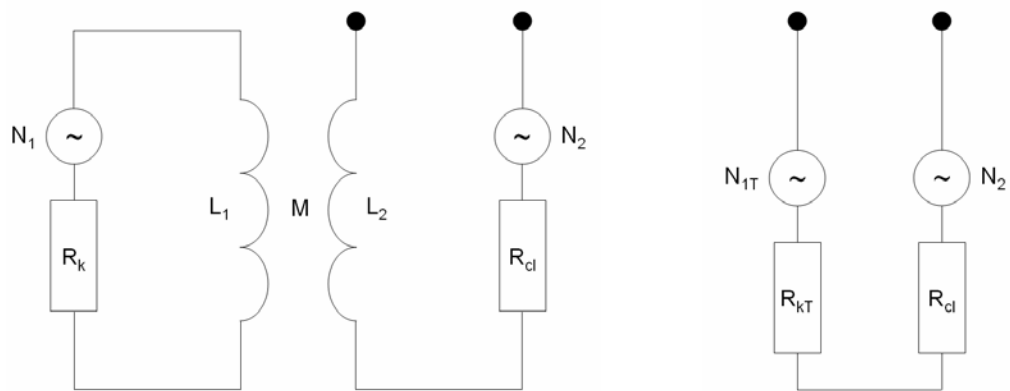


Figure 3-3: The equivalent circuit of a magnetically coupled radiofrequency coil. The primary circuit (left) corresponds to the radiofrequency coil and all the losses it produces. The secondary circuit (middle) is comprised of the coupling loop magnetically coupled to the primary circuit. The equivalent circuit (right) contains noise from the secondary circuit, and transformed noise from the primary. It includes the secondary resistance, and the transformed primary resistance.

The primary circuit, constituted by the radiofrequency coil, contains a series of resistances corresponding to all the losses occurring in the coil. The primary circuit, of inductance L_1 , is magnetically coupled to the secondary circuit, comprised of the coupling loop of inductance L_2 . The mutual inductance M defines an impedance

transformation between the circuits. The generator N_1 corresponds to the noise emitted by the primary circuit. The amplitude of the noise changes when it is transferred to the secondary circuit, and becomes N_{1T} . Similarly, the sum of resistance R_k becomes R_{kT} in the secondary circuit, which also adds a small supplementary amount of noise N_2 .

All the conductive components within a probe exhibit a resistance added in serie to the resistance of the radiofrequency coil and the specimen:

$$R_k = R_{sp} + R_{co} + R_{ce} + R_{sh} + R_{ra} \quad (3-9)$$

where each resistance value equates the time-average power dissipated in the respective component when the coil carries a one-ampere current (root-mean-square). Specifically, R_{sp} refers to the resistive loss inside the sample being imaged, and R_{co} is determined by the resistive loss taking place inside the radiofrequency coil conductor. R_{ce} corresponds to the dielectric loss taking place in the ceramic components of the probe. R_{sh} refers to the resistive loss occurring in the radiofrequency shield, and R_{ra} is the radiation resistance of the radiofrequency coil.

The noise emitted by the coil depends on the temperature of every component:

$$N_1 = \sqrt{4k(R_{sp}T_{sp} + R_{co}T_{co} + R_{su}T_{su} + R_{ce}T_{ce} + R_{sh}T_{sh} + R_{ra}T_{ra})B} \quad (3-10)$$

where T_{sp} , T_{co} , T_{su} , T_{ce} , T_{sh} refer to the absolute temperature of the specimen, the

radiofrequency coil, the substrate, the ceramic and the shield, respectively. T_{ra} corresponds to the absolute temperature of the environment broadcasting noise into the coil. N_1 is the standard deviation of the noise voltage.

Because the radiofrequency coil is magnetically coupled to the coupling loop, the noise N_1 will be injected into the coupling loop circuit, and change amplitude:

$$N_{1T} = \sqrt{\frac{4k\omega^2 M^2 (R_{sp} T_{sp} + R_{co} T_{co} + R_{su} T_{su} + R_{ce} T_{ce} + R_{sh} T_{sh} + R_{ra} T_{ra})}{(R_{sp} + R_{co} + R_{su} + R_{ce} + R_{sh} + R_{ra})^2}} B \quad (3-11)$$

The coupling loop adds noise to the circuit as well:

$$N_2 = \sqrt{4kR_{cl}T_{cl}} B \quad (3-12)$$

where N_2 is the standard deviation of the noise voltage created by the coupling loop, R_{cl} is the resistance of the coupling loop and T_{cl} its absolute temperature. Finally, the total amount of noise contaminating the experiment is:

$$N_{1T+2} = \sqrt{4k \left(\frac{\omega^2 M^2 (R_{sp} T_{sp} + R_{co} T_{co} + R_{su} T_{su} + R_{ce} T_{ce} + R_{sh} T_{sh} + R_{ra} T_{ra})}{(R_{sp} + R_{co} + R_{su} + R_{ce} + R_{sh} + R_{ra})^2} + R_{cl} T_{cl} \right)} B \quad (3-13)$$

The ratio in the right-hand part of the equality expresses the impedance-transformed noise originating in the radiofrequency probe, and transformed by the

coupling loop. The last product in the right-hand part of the equality corresponds to the noise added directly by the coupling loop. In a well-designed probe, that term is negligible. The expression above can be better understood by making the two following assumptions: i) the resistance of the coupling loop is negligible, and ii) the probe is matched to the characteristic impedance Z (50Ω) of the radiofrequency chain. We have:

$$N_2 = \sqrt{4kR_{cl}T_{cl}B} = 0 \quad (3-14)$$

$$Z = \frac{\omega^2 M^2}{(R_{sp} + R_{co} + R_{su} + R_{ce} + R_{sh} + R_{ra})} \quad (3-15)$$

Therefore, the standard deviation of the noise voltage N_{1T+2} injected in the radiofrequency chain is:

$$N_{1T+2} = \sqrt{4kZ \frac{(R_{sp}T_{sp} + R_{co}T_{co} + R_{su}T_{su} + R_{ce}T_{ce} + R_{sh}T_{sh} + R_{ra}T_{ra})}{(R_{sp} + R_{co} + R_{su} + R_{ce} + R_{sh} + R_{ra})} B} \quad (3-16)$$

If all the probe components are at the same temperature T_0 , the noise injected by the matched probe will be the one of a resistor of impedance Z at temperature T_0 (most commonly a 50-ohm resistance at temperature T_0). In addition, by cooling some components, their contribution to overall noise can be reduced.

4 The Signal-To-Noise Ratio

Every experimentalist attempts to maximize signal-to-noise ratio. In microscopy, the quality of the image relies on the ability of the probe to record electromagnetic energy stemming from the specimen efficiently, and then transmit it to the imager without noise degradation. A high signal-to-noise ratio recorded and sent to the scanner leads to a high-quality image. Reciprocally, a low SNR produces an image of poor quality.

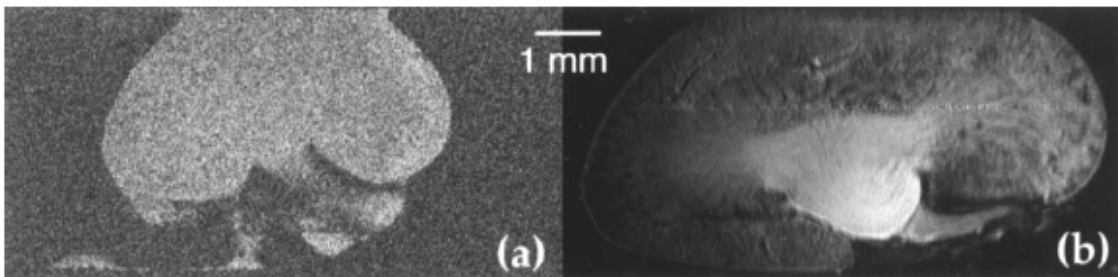


Figure 4-1: A mouse kidney acquired with low SNR by a copper probe (left) and with high SNR by a superconducting probe (right). [Figure reproduced from (16)]

We will produce in the text a definition of sensitivity that we can evaluate numerically, and explore the relationship between experiment size, holding field intensity, and signal-to-noise ratio. Three ways to increase SNR will be briefly exposed: volume encoding, the use of contrast agents, and short-echo time imaging sequences.

Two imaging sequences amenable to superconducting probes will be presented: the gradient-recalled sequence, and the radial acquisition sequence.

4.1 Increasing SNR by Maximizing the Sensitivity

The signal-to-noise ratio is proportional to the probe sensitivity. The prior presentation of both the signal transmission and the noise contamination within a probe leads to the expression of the probe sensitivity:

$$S \approx \frac{\frac{\omega_0}{V_{sp}} \int_{specimen} (B_1 / I) dV}{\sqrt{4k \left(Z \frac{(R_{sp} T_{sp} + R_{co} T_{co} + R_{su} T_{su} + R_{ce} T_{ce} + R_{sh} T_{sh} + R_{ra} T_{ra})}{(R_{sp} + R_{co} + R_{su} + R_{ce} + R_{sh} + R_{ra})} + R_{cl} T_{cl} \right)}} \quad (4-1)$$

The probe sensitivity should be maximized. A small coil, tightly encompassing the specimen, maximizes the numerator. The denominator may be minimized by cooling the probe components of dominant resistance, if possible. If the coil is dominant, the probe sensitivity can be significantly increased by cooling the coil, or making it superconducting. In contrast, if the specimen or a component that cannot be cooled is dominant, the sensitivity increase of a cryogenic probe will be marginal. Consequently, the one or several components of significant resistance must be identified.

4.1.1 Scaling Laws

The resistance of a component depends on its size and the frequency of the electromagnetic field. The scaling laws are simplified models that include a specimen and a coil only. They identify the regime, in frequency and size, where the noise emitted by the coil is equal to the noise emitted by the specimen. In that regime, or at lower frequencies or smaller sizes, the use of a cryogenic probe is beneficial to sensitivity and SNR. At larger sizes or higher frequencies, the SNR increase provided by a cryogenic probe is insignificant.

For a multi-turn solenoid coil which geometry has been optimized, subjected to a homogeneous current of uniform skin-depth, irradiating a spherical specimen of homogeneous conductivity, including losses from coil and the specimen only (5):

$$\Psi \approx \frac{\omega^2}{\sqrt{\alpha a^2 \omega^{1/2} + \beta \omega^2 b^5}} \quad (4-2)$$

where Ψ is the SNR, a is the solenoid radius, b is the specimen radius, α is a constant dependent of the sensitivity of the experiment, β is a constant dependent on the conductivity of the specimen, and f is the frequency. The numerator corresponds to the signal, and the left-hand term of the denominator represents the noise voltage induced by losses in the coil. The right-hand term indicates the noise voltage stemming from the

specimen. At high frequency, the noise from the specimen dominates because of its ω^2 dependence. At a given frequency, an experimental size exists below which the coil noise dominates. Remarkably, the specimen noise voltage depends on the fifth power of the specimen size, and consequently, decreasing the size of the specimen is a very powerful way to reduce the amount of noise originating from the specimen. As a side note, if the specimen is non-conductive, the signal-to-noise ratio follows the expected $\omega^{7/4}$ law (4).

Ginefri et al. (6,31) described a model including a single-turn surface coil irradiating a semi-infinite specimen of homogeneous conductivity. In the parametric space of varying coil radius and operating frequency, the noise power emitted by the coil and the specimen are equal along a line illustrated in Figure 4-2 for a copper coil, a cold copper coil, and a superconducting YBCO coil.

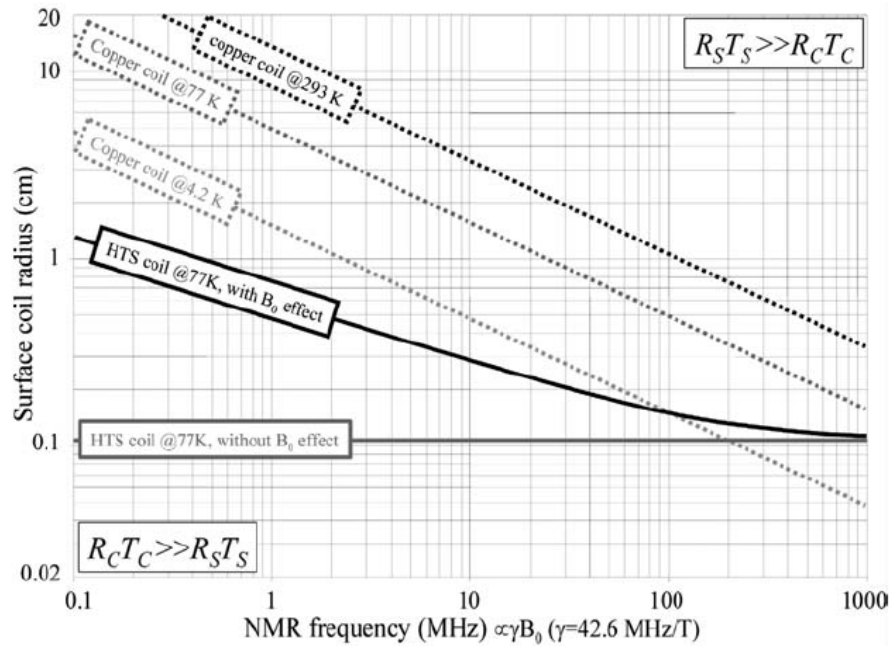


Figure 4-2: For a single-turn surface coil irradiating a semi-infinite specimen of conductivity 0.5 S/m, the line indicates sets of coil radius and operating frequency where the noise emitted by the specimen is equal to the noise emitted by the coil. The figure pertains to a room-temperature copper coil, a cold copper coil, and a superconducting YBCO with and without B_0 -induced change in coil noise properties. [Figure reproduced from (6)]

Ginefri et al. (31) report that for a 12-mm diameter coil, the noise power of the coil and specimen are equal at 64 MHz. It should be emphasized that the specimen is semi-infinite. For a spherical specimen, the noise emitted by the specimen would be much less, and the curves would move toward higher frequency and larger size. Glover and Mansfield (32) comment "in microscopic imaging regimes, the interdependence of these effects (the interdependence of coil and specimen resistance) are not clear cut, but

below around 10 mm coil diameter and 400 MHz, it is the room-temperature coil's own resistance that will dominate."

Analytical scaling laws make a number of assumptions. They idealize the coil and specimen geometry. They assume that homogeneous currents circulate in the coil, that can be described using the concept of skin-depth. They neglect proximity effects, and often, dielectric dissipation. The analysis is limited to two dissipative components magnetically coupled: the coil and the specimen. We will relax most of these assumptions later in the text.

4.2 Increasing SNR by Volume Encoding

Besides maximizing the probe sensitivity and SNR by cooling the coils, several acquisition strategies increase the SNR available in magnetic resonance microscopy. Volume encoding is a technique where a three-dimensional volume is acquired rather than a slice-selective, two-dimensional image. Because a larger volume is excited by a pulse, a larger amount of signal is collected by the coil during the three-dimensional acquisition, which mitigates the low sensitivity of magnetic resonance microscopy.

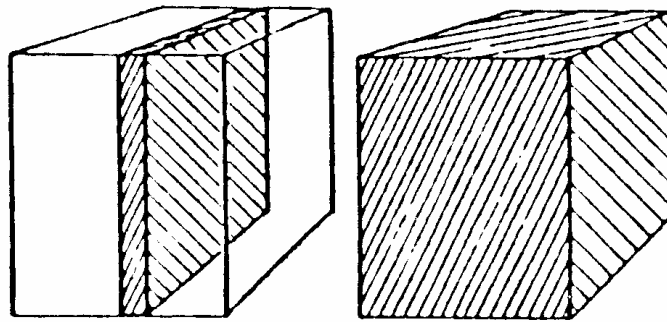


Figure 4-3: Many imaging sequences excite a slab of magnetization (left) that emits signal. In volume encoding techniques sometimes used in microscopy (right), the entire volume is excited and more signal is collected by the coil. [Figure Reproduced from (33)]

4.3 Increasing SNR With Contrast Agents

Similarly to the techniques presented earlier, the amount of signal recorded in resonance magnetic imaging can be increased by the use of contrast agents, paramagnetic substances that increase the spin-lattice relaxation rate. We will limit our presentation to gadolinium, a powerful hydrogen relaxation catalyst due to the fact that it possesses seven unpaired electrons, a high magnetic moment, and binds easily to bulk water (34). Gadolinium ions can relax hydrogen nuclei at a rate exceeding 10^6 s^{-1} .

The rare-earth metal is acutely toxic: *in vivo*, gadolinium ions produce insoluble oxides and hydroxydes, precipitate with carbonate and phosphate ions in tissue, deposit in the liver and macrophages, and finally accumulate in bones (35). To reduce toxicity, the ion can be encaged in a chelate, an organic framework that binds to gadolinium very effectively, yet allows for fast bulk water exchange and effective hydrogen relaxation.

Chelating agents available commercially differ in their molecular structure: linear or macrocyclic, ionic or non-ionic. Macrocyclic compounds exhibit superior chemical stability, and non-ionic chelates result in greater osmotolerance, dosing and injection flexibility (35).

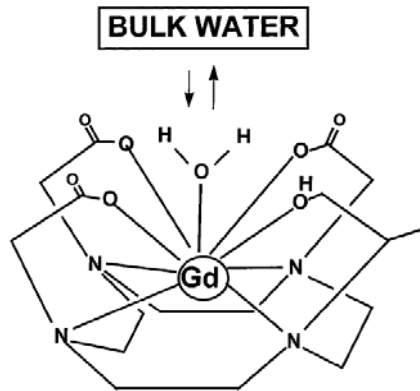


Figure 4-4: Chemical structure of the macrocyclic, non-ionic gadolinium chelate Prohance (Bracco S.p.A., Milano, Italy). [Figure reproduced from (35)]

A macrocyclic, non-ionic gadolinium chelate (ProHance, Bracco S.p.A., Milano, Italy) was perfused into the fixed specimens used for imaging, increased the amount of signal recorded and allowed the use of a short repetition time ($TR \leq 100$ ms).

4.4 Increasing SNR with Imaging Sequences

A magnetic resonance imaging sequence is always specific to an application and can increase the signal-to-noise very significantly. As we have seen, the signal from the transverse magnetization vanishes according to the time constant T_2 , a phenomenon that can be neither avoided nor slowed down. To record high levels of signal, it is crucial to acquire the signal from the spins early, and to complete the acquisition early before the signal vanishes. Therefore, an short echo time is desirable.

To shorten echo-time, the traditional spin echo sequence can be replaced by a gradient-recalled sequence. The absence of a 180° pulse shortens TE. The image is T_2^* -weighted as phase accumulation due to field inhomogeneity is not compensated.

The echo-time can be reduced further by sampling echoes asymmetrically. The Fourier transform is conjugate-symmetric. In principle, only half of an echo needs to be acquired. The missing data can be replaced by the complex conjugate of the data that has been acquired. The Fourier data can then be inverted to reconstruct the image. In our practice however, no less than 75% of the Fourier data is sampled during asymmetric acquisition. In other words, less than the first quarter of the echo is left unrecorded, shortening the echo-time by the duration of a quarter-echo.

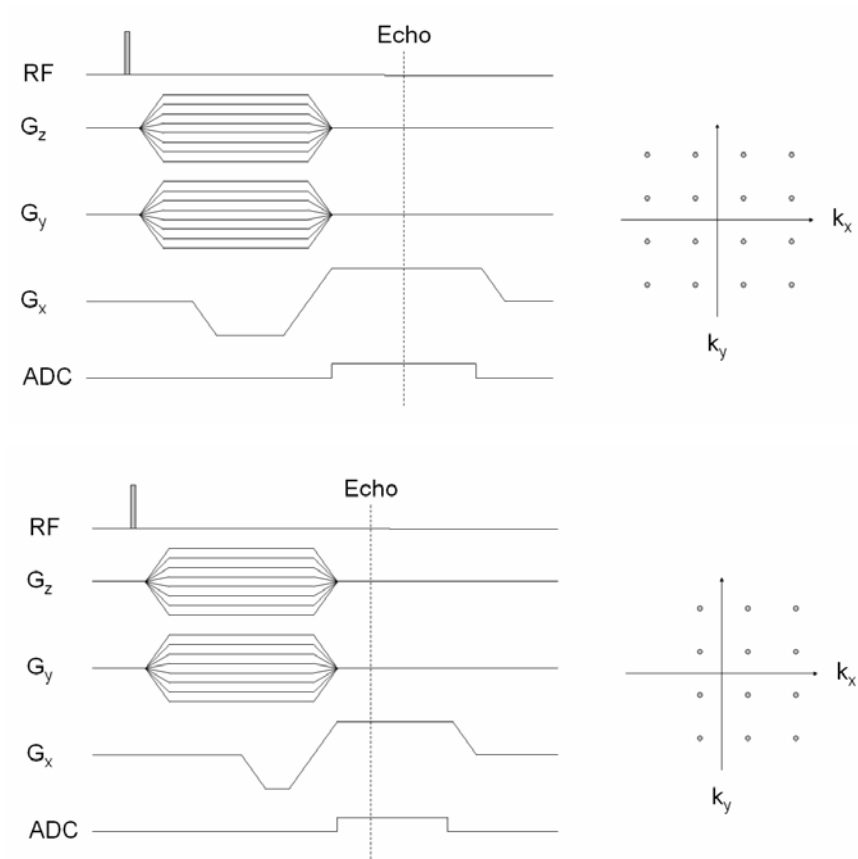


Figure 4-5: the three-dimensional gradient-recalled echo imaging sequence contains a non-selective hardpulse. The first part of the echo can be left unsampled to shorten echo time.

Another type of imaging sequence, radial acquisition, can increase signal levels considerably. Fourier space is encoded using trajectories that start at the center of Fourier space. This eliminates the need for phase encoding lobes prior to the opening of the sampling window, thus reducing the effective echo-time. Strictly speaking, a gradient or radiofrequency-refocused echo is no longer acquired: the free induction decay is encoded directly (1,36).

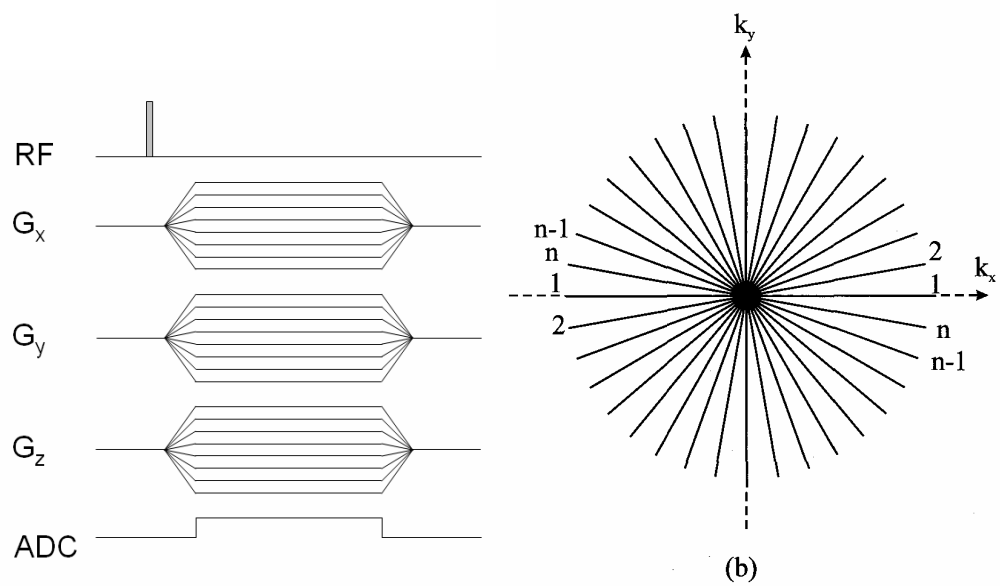


Figure 4-6: In a radial acquisition sequence, the sampling window is open as soon as the spatial encoding begins and the free induction decay of the spins submitted to gradients is recorded. The echo-time is extremely short, in the range of a few hundreds of microseconds.

The framework necessary to estimate the sensitivity of a probe has been established and several techniques enhancing SNR have been presented. We turn our attention to the figure of merit used to characterize a probe.

5 The Radiofrequency Coil

Magnetic resonance relies on the absorption of electromagnetic energy at the Larmor frequency, and re-emits radio waves at the Larmor frequency. Resonant electrical circuits can efficiently produce waves at their resonant frequency, and absorb energy at the same frequency. The first requirement of a radiofrequency coil is to be resonant at the Larmor frequency of interest. In addition, the coil should produce a homogeneous magnetic field tightly coupled to the specimen. Finally, it should induce as little loss as possible. This section gathers the most common figures of merit of a radiofrequency coil, that will be computed later on.

5.1 Resonant Frequency

It is well known that a tank circuit resonates at the frequency:

$$\omega = \frac{1}{\sqrt{LC}} \quad (5-1)$$

where ω is the resonant frequency of the circuit, L its inductance, and C its capacitance.

As magnetic resonance is a process that relies on magnetic induction, the coil inductance should be made as large as possible. The coil capacitance, however, should

remain sufficient to prevent excessive resonant frequency shift when the specimen is inserted into the coil and slightly increases the coil capacitance. In addition, the electrical losses occurring in the coil are proportional to the square of the electrical field. It is therefore desirable to keep the electrical field crossing the specimen as low as possible, for example by using distributed capacitance.

In the specific case of superconducting coils, the coils must remain thermally isolated and cannot be soldered, which precludes the use of variable capacitors to adjust the resonant frequency. Other techniques are possible. The inductance of the superconducting coil can be increased by mutual coupling of part of the inductance of another coil, itself superconducting (21) or not (16). Also, the resonant frequency of a superconducting coil can be decreased by bringing a high-permittivity, low-loss-tangent dielectric material in a region where the coil produces a high electric field (37).

5.2 Impedance

In order to transfer radiofrequency energy between components of an electrical circuit, the components must present the same apparent impedance. A radiofrequency coil is matched when its impedance is equal to the impedance of the radiofrequency chain. More specifically, in a magnetically coupled radiofrequency coil, the coupling loop transforms the coil impedance into the desired impedance:

$$Z_a = \frac{\omega^2 M^2}{Z_1} + Z_{CL} = Z \quad (5-2)$$

where Z_a is the impedance of the radiofrequency coil at the connectors of the coupling loop, ω is the resonant frequency, M is the mutual inductance between the radiofrequency coil and the coupling loop, Z_1 is the impedance of the coil at its connectors, and Z_{CL} is the impedance of the coupling loop at its connectors. The match is realized when Z_a equates Z , the impedance of the radiofrequency chain.

In practice, the electromagnetic environment of a superconducting coil may vary from experiment to experiment: the specimen may change in size, the AC resistivity of the superconducting film may gradually degrade and increase. It is desirable for the match to be adjustable, which is achieved by modifying the mutual inductance between the coil and the coupling loop. The mutual coupling M can be altered by changing the distance separating the coil from the coupling loop, their relative surface area, or the relative angular position of the vectors normal to their surface.

5.3 Homogeneity

To avoid non-uniform signal levels across the field-of-view, and so that the same flip angle is achieved across the specimen, the B_1 field created by the coil must be homogeneous. A perfectly homogeneous coil creates a B_1 field component along a single direction of the transverse plane, no field component in the second direction of the transverse plane, and no field component along B_0 . That ideal situation can never be entirely achieved.

The homogeneity of coil can be estimated by measuring the amplitude of the B_1 field in the three orthogonal directions of space, usually through the center of the probe.

5.4 Filling Factor

An efficient radiofrequency coil is designed to deposit most of its energy as magnetic power into the specimen. The filling factor is a figure of merit, in the case of a solenoid coil, smaller than 0.5 (4), that should be as large as possible:

$$\eta = \frac{\int_{specimen} B_1^2 dV}{\int_{all\ space} B_1^2 dV} \quad (5-3)$$

where B_1 is the magnetic flux density created by the coil.

The overall size of a coil should be chosen to tightly encompass the specimen so that the filling factor is maximized. In superconducting coils, vacuum insulation requirements conflict with maximizing the filling factor, and an acceptable compromise must be found.

5.5 Sensitivity

The sensitivity of a coil refers to its ability to create a large signal when submitted to a time-varying magnetic flux density. When the coil is matched, the sensitivity is:

$$S \approx \frac{\frac{\omega_0}{V_{sp}} \int_{specimen} (B_1 / I) dV}{\sqrt{4k \left(Z \frac{(R_{sp} T_{sp} + R_{co} T_{co} + R_{ce} T_{ce} + R_{sh} T_{sh} + R_{ra} T_{ra})}{(R_{sp} + R_{co} + R_{su} + R_{ce} + R_{sh} + R_{ra})} + R_{cl} T_{cl} \right)}} \quad (5-4)$$

Methodically maximizing the sensitivity of the microscopy coil is complex, and requires the determination of the power dissipated by every component of the probe. Numerical estimations of the equivalent resistance of every component will be presented in the next section.

5.6 Quality Factor

The coil quality factor is a figure of merit commonly quoted in the literature, expressed as the ratio of the energy stored in the coil over the energy dissipated per cycle:

$$Q = \frac{\textit{energy stored}}{\textit{energy dissipated per cycle}} \quad (5-5)$$

The quality factor is a global figure of merit that alone does not characterize the magnetic performance of the coil. First, the numerator contains energy that is stored in the electrical field, which is useless to magnetic resonance. Secondly, the numerator may also contain magnetic energy not deposited in the specimen. If the quality factor has to be reported, at least the pair of number η and Q should be quoted. However, part of the appeal of the quality factor relies in the fact that it can be measured experimentally very easily (38,39).

5.7 Superconducting Coil Peculiarities

YBCO, a single crystal, contains copper planes along which superconductivity takes place if the planes remain uninterrupted by a change in crystalline structure. Consequently, a single YBCO crystal must be deposited onto a perfectly flat substrate. In addition, the substrate must exhibit a crystalline structure and a linear expansion coefficient similar to YBCO. Acceptable substrates include lanthanum aluminate and sapphire. Sapphire benefits from a lower loss tangent than lanthanum aluminate, and therefore a YBCO coil deposited on sapphire exhibits a larger quality factor than the same coil deposited on lanthanum aluminate.

A temperature gradient between the cold superconducting coil and the room-temperature specimen is unavoidable. A layer of vacuum insulation minimizes heat transfer towards the coils. Since the evacuated region within the coil cannot be occupied by the specimen, superconducting coils suffer from a lower filling factor than a room-temperature coil where no vacuum insulation is required. The filling factor may decrease to a value as low as 0.2 (15).

YBCO transmits power non-linearly (40,41). At increasing transmitted power levels, the current carried by the coil saturates and cannot surpass the critical current value of approximately 3 MA/cm² (YBCO quality assurance certification, Theva GmbH,

Ismaning, Germany). The non-linear power transmission by YBCO bears two main consequences in practice. First, doubling the transmitted power level required for a 90-degree pulse achieves less than a 180-degree pulse. Similarly, the power required to achieve an arbitrary flip angle cannot be linearly predicted from the power required for a 90-degree pulse (40). Secondly, care must be exerted during the measurement of the quality factor with a network analyzer. The quality factor measurement should be repeated at decreasing amounts of power transferred to the coil. If the quality factor does not increase, the current carried by the coil remains sufficiently below the critical current value and the quality factor measurement is valid.

6 Finite-Element Radiofrequency Simulations

Three-dimensional, finite-element radiofrequency simulations can extract all the figures of merit of a radiofrequency coil. The benefits of numerical methods and their main limitations will be presented.

To introduce our numerical analysis in a tractable context amenable to experimental proof, we produce a simplified probe including a single coil, a specimen, a shield and a coupling loop. The probe was assembled experimentally. A radiofrequency model was defined and solved numerically. We will briefly expose the indirect relationship between solution accuracy and computation time. Also, we will see that the experimental validation of the numerical model is critical. The validation can be carried out by comparing numerical outputs to experimental values, or by confirming the internal consistency of the model. Finally, radiofrequency simulations will be used to estimate the losses taking place in the probe.

6.1 Benefits

A probe includes a complex assembly of dielectric materials and conducting components coupled to each other. It is worthy wondering if analytical methods can be successfully applied to characterize a probe. Analytical methods (42-44) are subject to a number of limiting assumptions. They usually ignore dielectric materials, the dissipation that they cause and their effect on the probe resonant frequency. In addition, a radiofrequency shield is usually not included because the effect on the probe resonant frequency and quality factor is highly dependent on geometry. Analytical methods only describe simplified probes with a few components; otherwise, the mutual coupling between many components becomes unmanageable analytically.

In contrast, three-dimensional numerical methods rely on a geometrical and electromagnetic description of every probe component. Within the probe and its surroundings, the numerical solver identifies the electromagnetic fields satisfying Maxwell's equations. Essentially, the solution includes the coupling of every component to all the others. Therefore the figures of merit computed pertain to the entire probe, presented as a complex electromagnetic assembly of all the probe components.

6.2 Limitations

Numerical methods can be computationally expensive. A typical radiofrequency model of a probe requires a few hours to be solved. Often, slightly different probe configurations need to be compared and each requires a solution, which can become time-consuming.

The finite-element methods used in this dissertation require the definition of a mesh encompassing the entire probe and its surroundings. The electromagnetic fields are calculated at the mesh nodes, and interpolated in-between. The physical size of the mesh bears an indirect influence on the accuracy and precision of the solution. To estimate precision, the standard deviation of every figure of merit can be determined by repeating the same analysis with different meshes. Accuracy can be determined experimentally or by checking the mutual consistency of different model outputs.

In addition, as with any complex numerical model, it is crucial to validate the model against experimental values to guarantee that the model outputs are plausible.

6.3 A Simple Probe

To introduce finite-element numerical models, we focus on a simplified radiofrequency probe. We elucidate the relationship between solution accuracy and computation time. Then we carry out the experimental validation of our radiofrequency model, and compute some figures of merit of the simplified probe.

6.3.1 Probe Configuration

The simple probe includes a magnetically coupled horse-shoe coil sandwiched between sapphire substrates, and irradiating a spherical, homogeneous specimen of known conductivity. To illustrate different types of losses within the simple probe, we model the probe: i) without shield; ii) with a square flat copper shield.

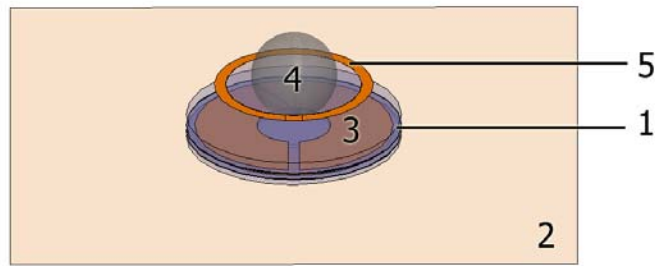


Figure 6-1: (Right) A stack of circular sapphire substrates (1) lays on a square copper shield (2) 100 mm wide. The substrates exhibit a 38 mm outer-diameter, the two lower substrates are 1 mm thick, and the top one is 3 mm thick. The copper traces of the horse-shoe coil (3) measure 35 mm outer-diameter, and 13 mm inner-diameter, and are interrupted by a 2 mm wide gap. They are sandwiched between the substrates. A homogeneous spherical specimen (4), 15 mm in diameter, of known conductivity equal to 4 S/m lies at the center of the top surface of the thicker substrate. The coupling loop (5), measuring 28 mm outer-diameter and 24 mm inner-diameter, is matched to the radiofrequency chain and placed above the coils.

The radiofrequency model of the simple probe was defined using a commercially available finite-element software (HFSS version 10.1, Ansoft Corporation, Pittsburgh, PA). The interplay of solution accuracy, size of a finite-element, and computation time is presented below.

6.3.2 Precision, Mesh Size and Computation Time

In the radiofrequency model, the connectors of the coupling loop are excited with a power equal to 50 W root-mean-square. The actual power entering the model can be measured numerically, and is given by the real part of the Poynting vector integrated over the cross-section feeding the model. It may differ from the 50 W input because of numerical inaccuracy and imprecision. The plot below shows the calculated value of power entering the model, integrated numerically using an increasingly refined mesh. When the mesh is sufficiently refined, at the expense of computation time, the integrated power converges towards the 50 W input power.

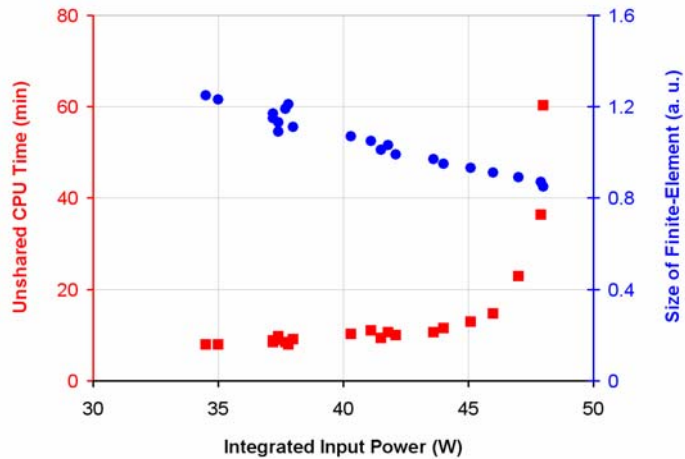


Figure 6-2: The input power sent to the model is 50 W. The model was solved 21 times with a mesh increasingly refined. The integrated input power measured inside the model is given on the horizontal axis. A measure in arbitrary unit of the relative finite-

element size used during the computation ranged from 0.85 to 1.25 (y-axis on the right, dots on the graph). It can be seen that with smaller finite-elements, the integrated input power converges towards 50 W. The amount of unshared computer-processing-unit (CPU) time required by the computations ranged from 8 to 63 minutes (y-axis on the left, squares on the graph). The computation load grows exponentially with smaller finite-elements, but allows the solution to converge towards its true value. The oscillations in both curves are error caused by numerical noise.

In Figure 6-2, numerical inaccuracy corresponds to the separation distance between a data point and the right-hand-side y-axis. Numerical imprecision, also referred to as numerical noise, causes the oscillation of the data points; it is mainly due to the discretization of the model into elements of different sizes. Numerical noise contaminates all the model outputs (Help File of Ansoft HFSS version 10.1.3 , entry "Cost Function Noise"). To quantify numerical imprecision, the standard deviation of a figure of merit can be calculated by solving the model repeatedly with a slightly different mesh. Numerical inaccuracy can be estimated by comparing a model output to an experimental value.

6.3.3 Validating a Model Experimentally

Figure 6-2 illustrates that a numerical solution converge towards its correct value if the model is sufficiently complex, and if the mesh is appropriately refined. To guarantee that the figures of merit extracted by a radiofrequency model are accurate, it is crucial to validate the model experimentally. Only a few figures of merit can easily be measured experimentally; they are compared to the values predicted by the model. If they are consistent, the model is deemed validated, which implies that different, more elaborate figure of merit predicted by the model are assumed plausible without experimental proof.

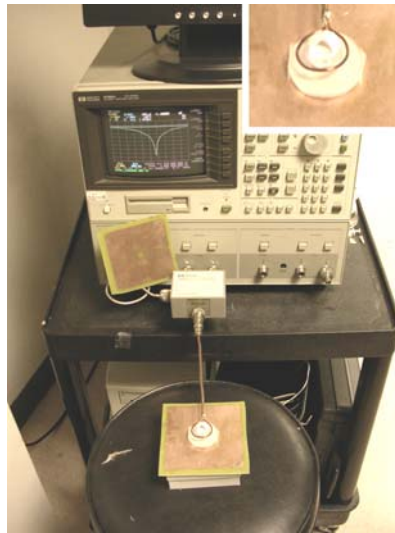


Figure 6-3: the insert (top right) shows the simple probe, the specimen and the coupling loop. The coupling loop was connected to a network analyzer so that the resonant frequency of the probe and its quality factor could be measured without shield and with a flat copper shield. Similarly, the separation distance between the coupling loop and the coil was recorded.

In Table 6-1, we compared the resonant frequency predicted by our model to the same value measured experimentally. Similarly, we made comparisons of the separation distance between the coupling loop and the coil, as well as the quality factor.

Table 6-1: The resonant frequency, the separation distance between the coupling loop and the horse-shoe coil in a matched configuration, as well as the coil quality factor were measured experimentally and compared to the values predicted by the radiofrequency model. For experimental results, the error is given by the standard deviation of 5 measurements. For simulations, the error is given by the standard deviation of the output computed at least 5 times with a different mesh.

	No Shield	Shield
$f_{\text{experimental}}$ (MHz)	327 ± 0.2	478 ± 0.3
$f_{\text{simulated}}$ (MHz)	331.6 ± 0.4	485.2 ± 0.5
$d_{\text{experimental}}$ (mm)	12 ± 1	7 ± 1
$d_{\text{simulated}}$ (mm)	10	6
$Q_{\text{experimental}}$	150 ± 7	170 ± 9
$Q_{\text{simulated}}$	166 ± 1	211 ± 14

The resonant frequency predicted by the radiofrequency model is in excellent agreement with the resonant frequency measured experimentally. The discrepancy between simulation and experiments is smaller than 5 %.

The separation distance between the coupling loop and the coil is measured when the power match is realized. According to equation (5-2) on p. 53, large losses taking place in the probe require a large mutual inductance for the match to be realized, and consequently a short separation distance between the coil and the coupling loop. Qualitatively, experimental and simulated results are in good agreement. Quantitatively, simulated values are larger than experimental values. Assuming that the experimental value is correct, the inaccuracy is smaller than 20%. Similarly, simulated and measured values of quality factors are qualitatively consistent, the inaccuracy is smaller than 20%.

The previous paragraphs illustrate three aspects of radiofrequency simulations consistent with our personal experience. First, both the estimation and the measurement of frequency are very accurate. Secondly, values highly dependent on geometry, including the apparent impedance and inductive coupling, are more difficult to measure and their numerical estimation is subject to a larger inaccuracy. Thirdly, the repetition of the measurement or the numerical estimation unveils a rather small imprecision rather

than the larger, and consequently more meaningful, inaccuracy. The imprecision used in error bars should be replaced with an estimation of inaccuracy, which can be determined by verifying the internal consistency of the model.

We will present in the next chapter a method leading to an estimation of inaccuracy.

6.3.4 Validating a Model Through its Internal Consistency

Different model outputs should be consistent with each other. We present a method that evaluates and compares the losses within the probe after the impedance-transformation by the coupling loop.

The characteristic impedance of our radiofrequency chain is 50Ω . We excite our radiofrequency model at the connector of the coupling loop with a power equal to 50 W root-mean-square. To realize the power match, the coupling loop transforms the impedance of the probe into the impedance of the radiofrequency chain. Consequently, the coupling loop carries a one-ampere, root mean square current and the sum of all the losses in the probe correspond to a 50Ω resistor. If all the losses calculated by the radiofrequency model amount to the characteristic impedance of the radiofrequency chain, the model is internally consistent:

$$Z = R_{sp,T} + R_{co,T} + R_{ce,T} + R_{sh,T} + R_{ra,T} + R_{cl} \quad (6-1)$$

where the suffix refer to the component described in equation (3-9) on p. 36 and the capital T indicates the impedance-transformed value. The radiofrequency solver calculated the value of the transformed resistance of each probe component (Table 6-2). The dissipation among all the components slightly exceeds 50 Ω , tainted by an error smaller than 20%. The model is internally consistent to better than 20%.

Table 6-2: transformed resistance of the probe components. The sum of the resistances of all the components ranges between 54.7 Ω and 61.2 Ω . It should be 50 Ω , the impedance of the radiofrequency chain.

	No Shield	Shield
$R_{sp,T} (\Omega)$	25.8 ± 0.2	8.7 ± 0.1
$R_{co} (\Omega)$	34.8 ± 0.6	37.3 ± 0.5
$R_{sh,T} (\Omega)$	N/A	10.2 ± 0.1
$R_{ce,T} (\Omega)$	0.004 ± 0.0001	0.01 ± 0.001
$R_{ra,T} (\Omega)$	0.02 ± 0.01	2.7 ± 0.5
$R_{cl} (\Omega)$	0.54 ± 0.01	0.50 ± 0.03
Total	61.2 ± 0.8	59.4 ± 1.2

We will from now on present frequency results with a 5% error bar, and all other values with a 20% error bar.

We will present in the following paragraph the more advanced values and figures of merit that can be estimated by our radiofrequency model.

6.3.5 Transformed Resistance

An ideal probe exhibits a specimen resistance amounting to the characteristic impedance of the radiofrequency chain and no other loss takes place (45). The transformed resistance of a probe component is equal to the power dissipated when the coupling loop carries a one-ampere, root-mean-square current. All the losses within the probe are given in Figure 6-4.

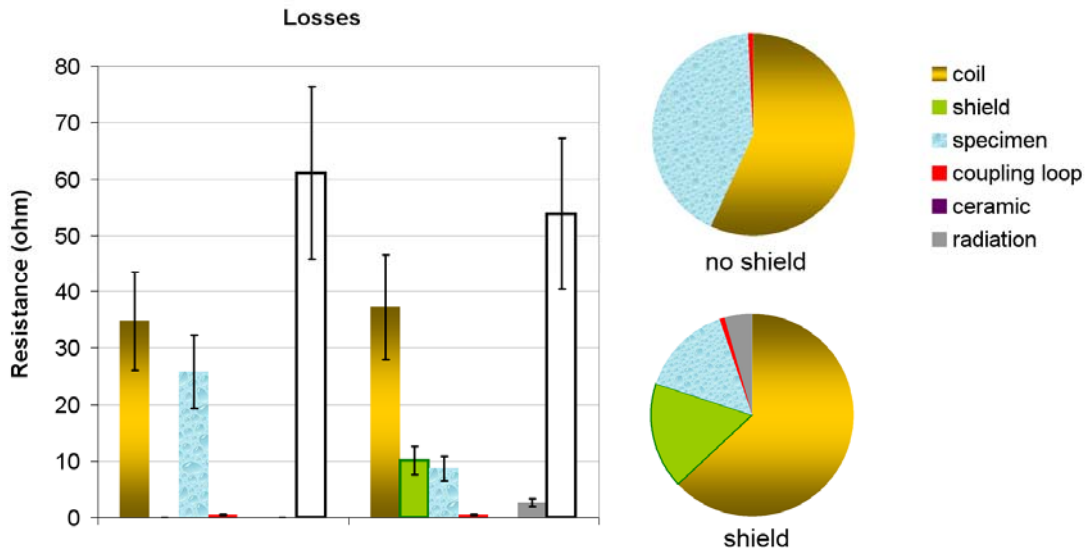


Figure 6-4: Transformed resistance of each probe component for the simple probe, without and with a shield. The hollow bar gives the total losses, which should amount to 50 Ω . Errors bars equal to $\pm 20\%$ indicate numerical error.

Regardless of the shield configuration, the losses in the coupling loop and in the ceramic components of the probe are negligible. Similarly, the radiation resistance can be neglected. Without a shield, the losses taking place in the coil are similar to the losses in the specimen. The addition of a continuous shield does not significantly change the transformed resistance of the coil; however, supplementary losses equivalent to a 10- Ω -resistor take place within the shield. Consequently, the resistance of the specimen must be transformed to a lower value for the match to be realized, which is reflected by the position of the coupling loop closer to the coil (see Table 6-1).

Because the probes were not used for imaging, we will not present the figures of merit pertaining to homogeneity, filling factor and sensitivity. They will be calculated for the real probes presented later, and allow for comparison between the probes.

7 The Beryllia Probe

The beryllia probe was initially designed prior to the development of our radiofrequency analysis method; its geometry and the performance of its components were improved by using our models. The initial design and construction were executed in collaboration with colleagues at Creare Inc. (Hanover, NH) under a small business innovation research grant.

We will start by presenting the configuration of the probe and the radiofrequency model that was developed subsequently. We will use the superconducting coils that were manufactured, as well as the probe itself, to validate experimentally our radiofrequency model. Then, we will apply our finite-element analysis to the beryllia probe, verify the internal consistency of the model, and bring to light some areas of possible improvement in the probe design. Finally, we will show images acquired by the probe, and measure its imaging performance.

7.1 Probe Configuration

The beryllia probe is depicted in Figure 7-1. It was designed for mouse brain imaging at 9.4 T (21). The field-of-view was 11 x 11 x 22 mm, encompassing a mouse brain in its skull. It included two YBCO spiral coils in Helmholtz pair configuration and

a room-temperature radiofrequency shield. The spiral coils were manufactured to resonate much below the operating frequency of 400.2 MHz and manually tuned to frequency. During operation, the distance between the coils could be adjusted from 12.5 mm to 15 mm to alter the resonant frequency.

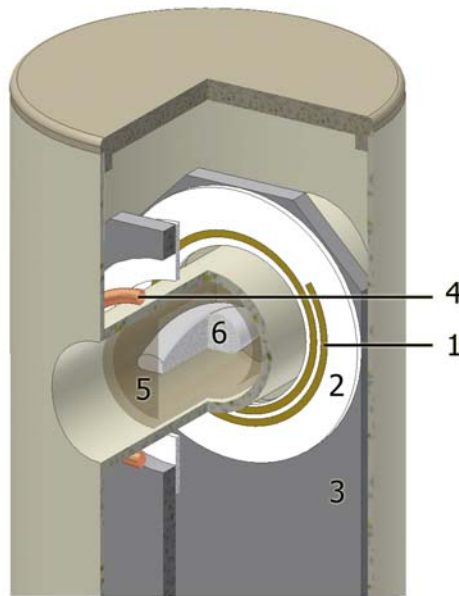


Figure 7-1: The schematic shows the essential components of the beryllia probe. A segment of the second superconducting coil and heat exchanger is removed in this schematic to allow better appreciation of the geometry. The YBCO traces (1) are deposited on sapphire substrates (2) attached to beryllia heat exchangers (3) in thermal contact with titanium chambers containing flowing helium vapor. The coils are inductively coupled to the radiofrequency chain by a room-temperature circular copper coupling loop (4). The cartridge (5) containing the mouse brain specimen (6) is placed at the center of the Helmholtz pair. A room-temperature copper foil is wrapped around the probe housing and acts as a radiofrequency shield. [Reproduced from (21)]

The superconducting coils were bonded to one end of heat exchangers made out of beryllium oxide (beryllia), a ceramic chosen for its high thermal conductivity of 285 W/mK and low loss tangent, below 0.0004. The other end of the heat exchangers was bonded to titanium chambers containing the flow of cryogenic vapor. The cylindrical body of the probe was machined from a garolite hollow tube, around which a room-temperature, one-mil thick, continuous copper shield was wrapped. Vacuum was actively maintained by a turbomolecular pump (Turbovac 361, Oerlikon Leybold Vacuum, Cologne, Germany) in a custom-built Gifford-McMahon cycle cryocooler (Creare Inc., Hanover, NH). The cryocooler was linked to the superconducting probe by a flexible, superinsulated vacuum line carrying a stream of cryogenic helium vapor circulating to and returning from the probe. Temperature feedback controlled the power input to a small heater just upstream from the titanium chambers at the base of the probe. The arrangement maintained the probe at 60 ± 0.1 K over cold runs lasting 96 hours or more, limiting changes in coil quality factor and resonant frequency caused by temperature fluctuations (41).

7.2 Radiofrequency Simulation

A finite-element model of the beryllia probe was defined. It included all the components presented in Figure 7-1, except for the garolite probe housing that was not represented. The mouse brain was simplified and described by a homogeneous cylinder

of electromagnetic properties and size similar to a mouse brain.

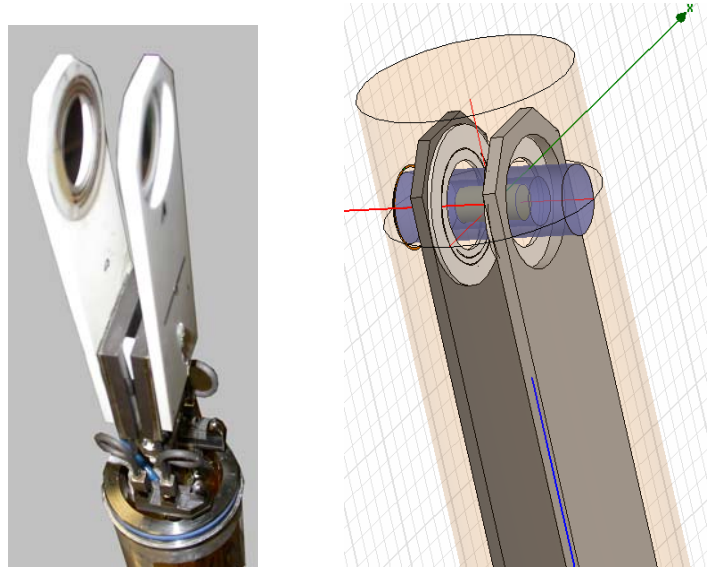


Figure 7-2: A picture of the beryllia superconducting probe without its housing (left) and the radiofrequency model (right). The model includes the superconducting traces deposited on sapphire substrates, held in place against beryllia heat exchangers, as well as the coupling loop, a cylinder-shaped specimen, the cartridge and the radiofrequency shield. In the model, the probe housing and the titanium heat exchangers are not represented. The mouse brain is represented by a cylinder, 14mm in length and 8 mm in diameter, of conductivity equal to 0.7 S/m and relative permittivity equal to 50.

The radiofrequency model was carefully validated using a single superconducting spiral coil and a copper replica, as well as the beryllia probe itself.

7.2.1 Model Validation Using a Single Coil

YBCO spiral coils were fabricated by deposition of a 300nm-thick, epitaxially grown yttrium barium copper oxide film (Theva GmbH, Ismaning, Germany) on a low dielectric loss sapphire substrate, passivated with a 100 nm-thick gold layer. They were tuned manually from an original resonant frequency of 180 MHz to approximately 410 MHz, close to the 400 MHz operating frequency of the probe. Copper replicas of the same coils were machined on an organic ceramic substrate having a relative dielectric constant (10) very close to that of the sapphire substrate (11) of the superconducting coils. The copper coil replica underwent the same manual tuning process. During manual tuning, a segment at the outer end of the coil trace is isolated from the part supporting the resonant mode by making a score with a razor blade. The number of turns carrying the resonant mode, the inductance and the capacitance decreases and the resonant frequency increases. The isolated, unused segment of trace is left on the substrate (Figure 7-3). The position of all the scores, as well as the shift in resonant frequency, were recorded.

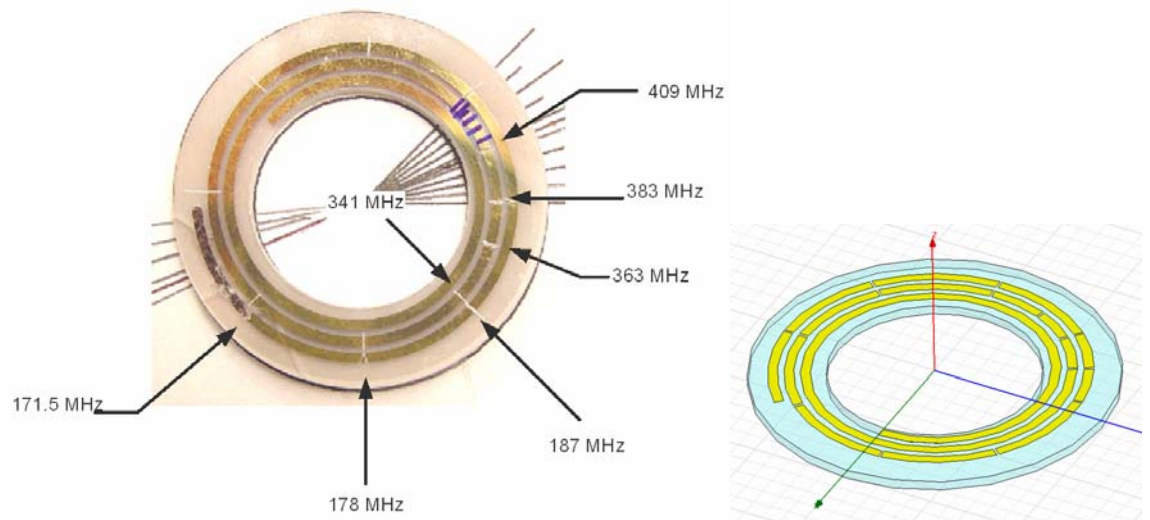


Figure 7-3: The superconducting coil (left) scored during the manual tuning process, and its radiofrequency model (right).

The YBCO coil geometry was defined in a radiofrequency model. The resonant frequency of the individual, stand-alone spiral coil was determined by finite-element simulation as a function of number of turns carrying the resonant mode. The predicted values of resonant frequency were compared to experimental values (Figure 7-4).

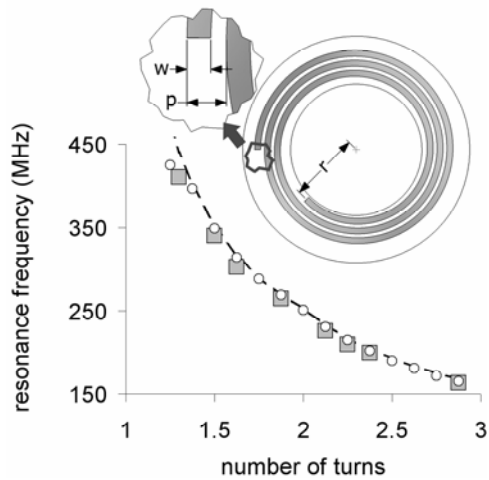


Figure 7-4: A detailed view of one spiral coil shows the pitch p of a spiral, and the trace width w . The inner radius r of the coil is measured to the midline of the inner trace. The spiral coil parameters are: $r=11.75\text{mm}$, $w=1\text{mm}$ and $p=1.65\text{mm}$. The superconducting coil substrate is a 38 mm outer diameter, 22 mm inner diameter, one-millimeter thick sapphire ring. The substrate of the copper replica coil is identical, but made out of a organic ceramic material of similar dielectric constant. Each coil resonates at 180 MHz as manufactured with an original number of turns of $N=2.875$. They can be brought to 410 MHz by reducing the number of turns to approximately 1.3. Data from a copper replica (o) is compared to tuning data from a superconducting coil after its manufacturing (□), as well as simulations (dashed line). [Figure reproduced from (21)]

The resonant frequency values predicted for a single superconducting coil are in excellent agreement with experimental data, with less than a 5% difference between experimental and simulated resonant frequency.

Supplementary validation of the radiofrequency models was carried out using the superconducting probe itself.

7.2.2 Model Validation Using the Probe

Within the beryllia probe, the YBCO coils were used in Helmholtz pair configuration. The resonant frequency could be fine-tuned by adjusting the spacing between the coils. The probe resonant frequency and impedance were recorded experimentally for different separation distance between the spiral coils, and compared to the values predicted by the radiofrequency model of the probe (Figure 7-5).

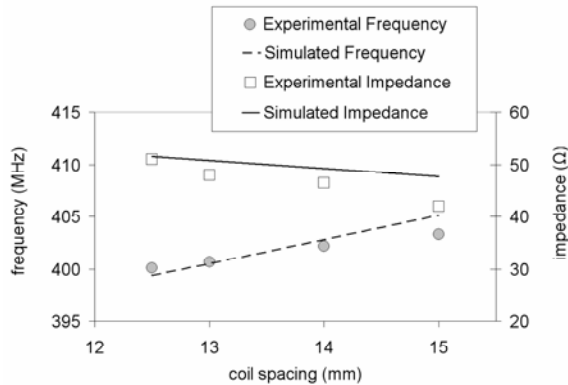


Figure 7-5: Experimental values of resonant frequency and impedance for a superconducting Helmholtz pair are compared to values predicted by the radiofrequency model. [Figure reproduced from (21)]

The predicted values of frequency are in good agreement with the experimental values. The model of the beryllia probe is validated; we will extract the figures of merit pertaining to the probe in the following paragraphs.

7.3 Resonant Frequency

The distance separating the coils can be adjusted between 12.5 mm and 15 mm, which corresponds to a change in simulated resonant frequency ranging from 399.4 MHz to 405.1 MHz, in good agreement with experimental values (Figure 7-5). The tuning range exceeding a few megahertz can readily compensate the frequency shift occurring when the specimen is inserted in the probe (typically, less than 0.25 MHz).

7.4 Impedance

The coupling loop remains immobile when the distance separating the Helmholtz coil is adjusted to fine-tune the probe. As the mutual inductance between coils changes, the probe impedance varies as well. Consequently, some degree of mismatch is unavoidable during the adjustment of the probe resonant frequency. Experimentally, the probe impedance varies between 51 Ω and 42 Ω , in good agreement with simulated values (Figure 7-5) and acceptable in practice.

7.5 Homogeneity

The homogeneity of the beryllia probe was assessed by comparing experimental SNR profiles to simulated B_1 intensity profiles.

Using the beryllia probe, field homogeneity profiles were recorded from a cylindrical phantom filled with silicone oil for comparison to predictions made by the radiofrequency model. A 3D gradient-recalled sequence was used to eliminate the impact of nonlinearity in the response of the YBCO film (40,41), which makes it otherwise difficult to correctly generate the refocusing pulse of the more traditional radiofrequency-refocused spin-echo sequence. The power level of a hard pulse exciting the entire phantom was chosen such as to maximize the signal intensity at the center of the pair.

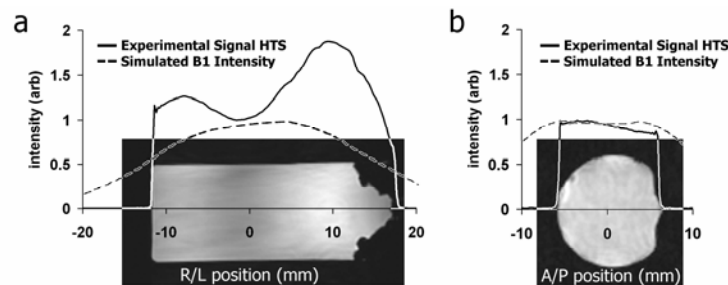


Figure 7-6: sagittal and transverse sections of a homogeneous cylindrical phantom, 11mm in diameter and 23mm in length (excluding the lateral lid protrusion) filled with silicone oil, showing the signal intensity at the mid-line of the image. (a) Central longitudinal slice from the 3D array acquired with the HTS coil and signal intensity across the R/L direction for the HTS coil (solid line), through the center of the Helmholtz pair. The simulated B_1 field intensity is given by the dashed line. The coupling loop of the superconducting probe is located at position +20mm along the R/L axis. The element closer to the coupling loop, located at +6.5mm, carries more current and generates a higher B_1 field than the coil further away, placed at -6.5mm. (b) signal intensity across the A/P direction for the HTS coil (solid line) through the center of the Helmholtz pair, and simulated B_1 field intensity (dashed line). The imaging parameters are: GRE 90° , TR 500 ms, TE 5.5

ms, FOV 51.2x25.6x25.6 mm, Bandwidth 62.5 kHz, NEX 1, Voxel Size 200x200x200 micron. [Figure reproduced from (21)]

The inhomogeneity in the plane transverse to the axis of the coils is less than 14%. Along the axis of the coils in the R/L direction, more pronounced B_1 inhomogeneity (Figure 7-6) has been recorded, which was clearly underestimated by our model. Serfaty et al. (44) presented an analytical method comparing the current circulating in each coil of a Helmholtz pair irradiated by a lateral coupling loop, excluding the effect of dielectric materials or a radiofrequency shield. The analysis indicates that a negligible current imbalance between coils is due to the lateral position of the coupling loop. However, in practice the shield decreases the coupling factor between coils, and the current imbalance can be underestimated. Our finite-element model includes the shield; the B_1 inhomogeneity was nonetheless underestimated. The conductivity of each of the superconducting films may be different experimentally whereas our radiofrequency model assumes equality. In addition, the relation between simulated B_1 intensity and measured MR signal may not be straightforward.

7.6 Filling factor

Similarly, the filling factor was calculated by the model:

$$\eta_{\text{beryllia}} = 0.012 \pm 0.002$$

The beryllia probe suffers from a low filling factor. The internal probe volume lost to vacuum insulation could be decreased by reducing the diameter of the superconducting coils.

7.7 Sensitivity

The equivalent resistance of every component was calculated by the model by computing the power dissipated by each component when the coupling loop carries a one-ampere, root-mean-square current.

Table 7-1: transformed resistance and absolute temperature of the beryllia probe components.

$R_{sp, T} (\Omega)$	$R_{co, T} (\Omega)$	$R_{sh, T} (\Omega)$	$R_{ce, T} (\Omega)$	$R_{ra, T} (\Omega)$	$R_{cl} (\Omega)$
13.9 ± 2.8	22.1 ± 4.4	24.3 ± 4.9	1.0 ± 0.2	0.19 ± 0.04	0.6 ± 0.1
$T_{sp} (K)$	$T_{co} (K)$	$T_{sh} (K)$	$T_{ce} (K)$	$T_{ra} (K)$	$T_{cl} (K)$
293	60	293	60	293	293

Based on equation (5-4) on p. 55, the sensitivity S_b of the beryllia probe is:

$$S_{\text{beryllia}} = 9.8 \pm 1.9 \text{ (a. u.)}$$

The equivalent resistance of the room-temperature shield is large. It could be decreased by cooling the shield. Similarly, the equivalent resistance of the coil could be reduced by using wider spiral traces. Both improvements would lead to a higher probe sensitivity.

7.8 Imaging

To test the in-plane resolution achieved by the beryllia probe, a 50-micron-thick polyester mesh (Small Parts, Miami Lakes, FL) with an opening size of 20 microns immersed in a 0.05 M copper sulphate solution was imaged using a gradient-recalled echo imaging sequence. Acquisition parameters were: GRE, Flip angle=90°, TR=100 ms, TE=5.5 ms, FOV=21.3x10.6x10.6 mm, Bandwidth=62.5 kHz, NEX=1, Voxel Size 10x10x20 micron, array size=1024³, 75% k-space asymmetric sampling. The total imaging time was 16.5 hours.

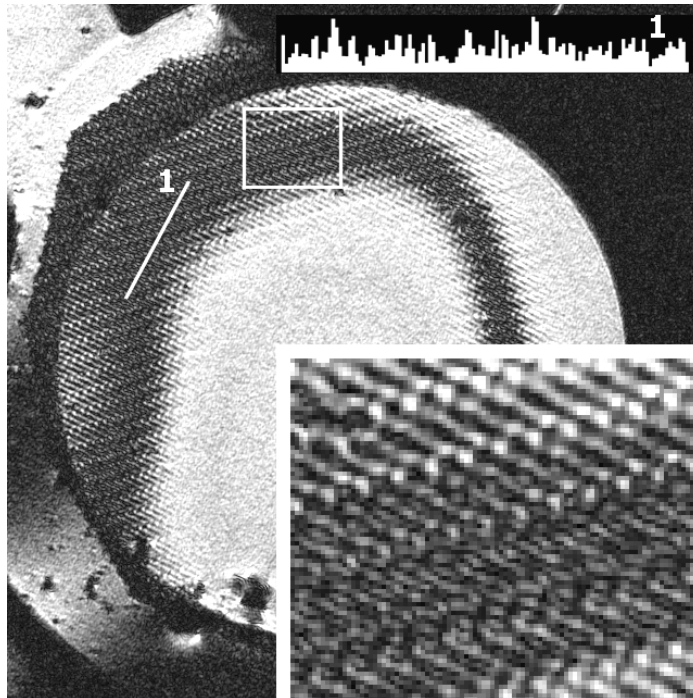


Figure 7-7: Image of octagonal piece of mesh fabric, clamped in a polymeric round clip, and immersed in copper sulphate (0.05 M) acquired with the beryllia probe. From a 1024^3 array, the selected imaging plane intersects the mesh with 20-micron openings along an arc on the left side of the image. The magnified section emphasizes dark regions of signal void delineating the mesh fibers. Bright dots mark the location of the mesh openings. The insert in the top-right corner shown the intensity profile acquired along line 1 placed perpendicular to the fibers. Two-pixel-wide peaks correspond to the position of the mesh openings falling within the imaging plane.

Figure 7-7 indicates that the spatial resolution achieved by the beryllia probe is better than 20 microns (48).

The same imaging sequence was repeated to acquire images of a perfusion-fixed C57BL/6 mouse brain, actively stained by transcathelial perfusion with a mixture of 10%

buffered formalin and ProHance (Bracco S.p.A., Milano, Italy) (46,47) allowing the use of short repetition time ($TR \leq 100$ ms).

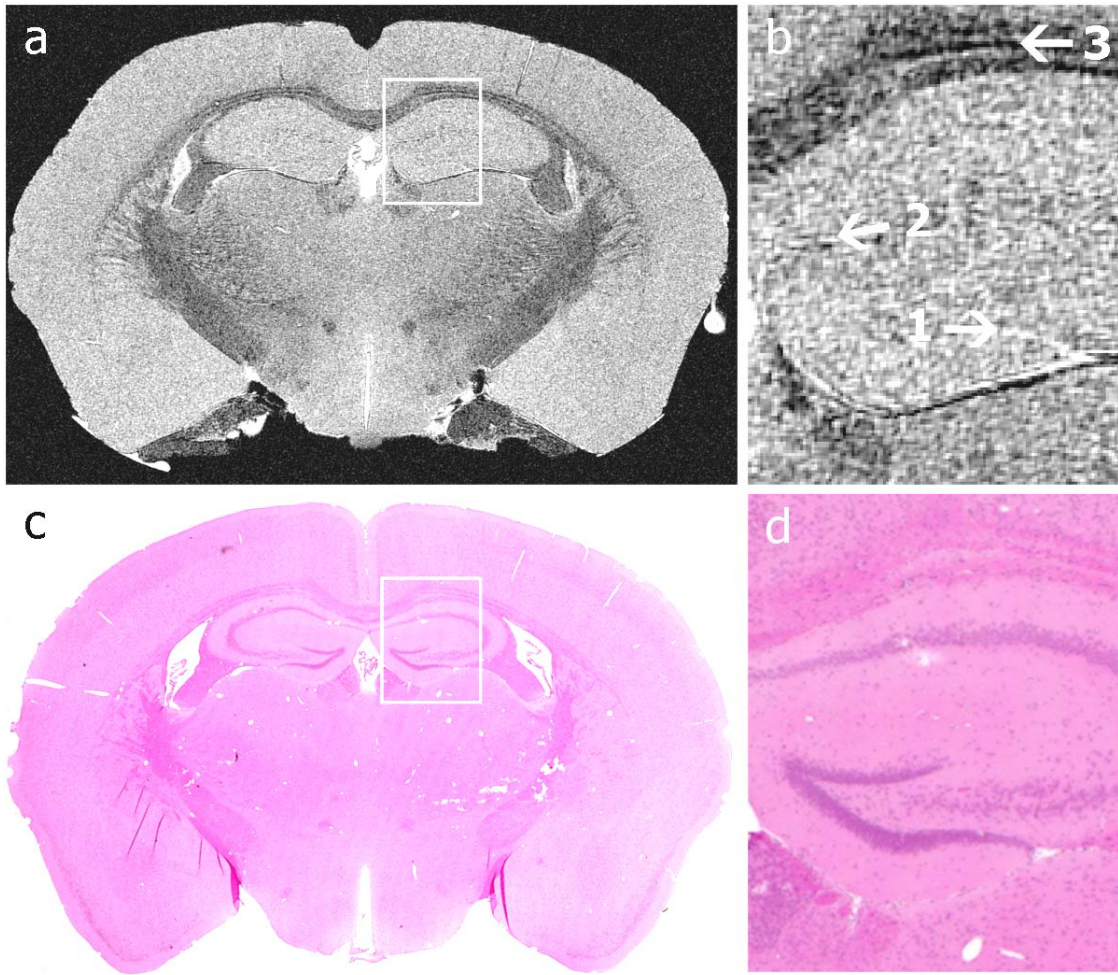


Figure 7-8: (a) 20-micron thick transverse slice through the mouse hippocampus, at a 10-micron in-plane resolution. Both axes are phase-encoded. (b) In the hippocampus, transitions between layers (1, 2) are visible. The layering of the corpus callosum (3) is apparent. Signal-to-noise ratio is 18. (c, d) Hematoxylin and eosin histological section of a different brain at approximately the same location, for comparison.

To make SNR comparisons, the same imaging sequence was used to image another mouse brain using a conventional room-temperature solenoid coil (14 mm diameter and 28 mm length). For each probe, signal-to-noise measurements were made from the 3D gradient recalled images at multiple points in the imaging volume. SNR increased by a factor ranging from 1.1 to 2.9 using the superconducting probe as compared to a copper solenoid.

7.9 Performance and Improvements

The sensitivity of the beryllia probe allowed us to encode at what we believe to be the highest resolution yet achieved for large-size biological specimens (48). Images of a perfusion fixed mouse brain at 10x10x20 micron revealed clear distinction of layers approximately four cells thick.

Radiofrequency simulations indicated that several improvements can increase the sensitivity of the probe further. The filling factor can be increased by reducing the diameter of the coils and decreasing the coil volume dedicated to vacuum insulation. The equivalent resistance of the shield can be decreased by cooling the shield. Finally, the resistance of the coil can be reduced by using a different superconducting trace.

8 The Alumina Probe

It has become apparent that our finite-element models are sufficiently accurate to guide the design of a new superconducting probe.

We will present the probe design that was developed through iterative radiofrequency simulations. We will present the figures of merit of the probe, then emphasize some electromagnetic and mechanical aspects of the probe design. Finally, imaging results will be shown.

8.1 Design Requirements

The alumina probe is designed to image a specimen less than 6 mm x 6 mm x 12 mm in size. In particular, potential specimens include the mouse cerebellum, a mouse kidney, or a 12-day mouse embryo. The imaging is carried out in a 9.4 T vertical bore magnet (Oxford Instruments, Oxford, United Kingdom). One critical change between the beryllia and alumina probe arose from installation of stronger gradients which reduced the external dimension of the probe from 54 mm (beryllia) to 40 mm (alumina). The new shielded coils increased the gradients from 0.95 T/m to 2 T/m, with up to a 50%-increase in duty cycle.

8.2 Probe Configuration

8.2.1 Geometry

The geometry of the alumina probe can be appreciated in the figure below.

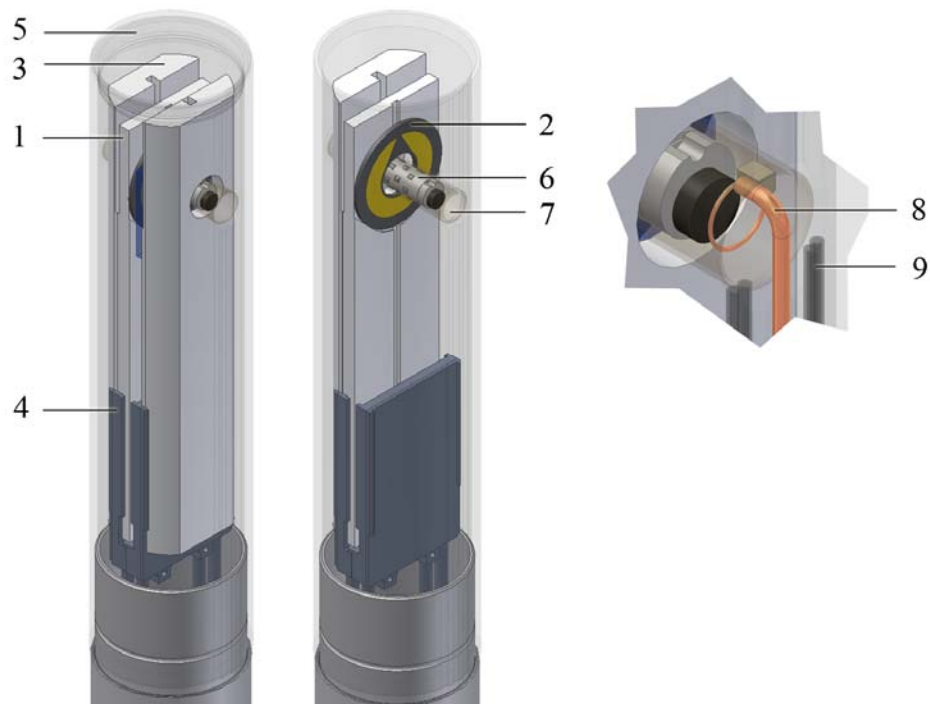


Figure 8-1: A central alumina heat exchanger (1) cools down the radiofrequency coil (2). Lateral Alumina heat exchangers (3) cool the copper shield wrapped around the group of three alumina components. All alumina parts are in thermal contact with titanium heat exchangers (4). A polymeric housing (5) allows vacuum to be established around the coils. The cartridge (6) holding the specimen is placed at the center of the sample well (7). A resonant coupling loop (8) matches the probe to the radiofrequency chain. Four nitrogen lines (9) supply a flow of room-temperature nitrogen flowing around the cartridge to prevent it from freezing.

The superconducting coil is attached to a central heat exchanger made out of 99.9% alumina. Two supplementary, lateral ceramic heat exchangers cool a copper shield. All the alumina heat exchangers are in thermal contact with titanium heat exchangers containing recirculating cold helium vapor.

Vacuum is established within the probe housing to limit heat transfer from the probe surroundings to the cold coils. The specimen is inserted into a thin-wall polymeric cartridge built by stereolithography (durable polypropylene-like resin Somos 9420, Quickparts, Atlanta, GA) and filled with a hydrogen-free perfluoropolyether (Fomblin, Solvay Solexis S.p.A., Bollate, Italy) to limit magnetic susceptibility induced artifacts during imaging. The external surface of the cartridge's circular wall has several short protrusions, allowing for a flow of room-temperature nitrogen to circulate around the cartridge and prevent the specimen from freezing. Four 0.97 mm outer-diameter, 0.58 mm inner-diameter polyethylene catheter lines (PE 50, BD, Franklin Lakes, NJ) provide a nitrogen flow amounting to a total of 10 L/min, maintaining the specimen at 4 °C.

8.2.2 Cooling

The operating temperature of the probe is set by the maximal cooling capacity of the cryocooler described in paragraph 7.1. No temperature regulation is implemented. Temperature can be monitored at different locations inside the probe, using a gallium-

arsenide optic fiber. The optic fiber (model T1 with cryogenic calibration, Neoptix, Québec City, Canada) is immune to radiofrequency interference and does not couple extraneous electromagnetic noise to the probe. The temperature of several components during the normal operation of the probe is given in the table below.

Table 8-1: temperature of several probe components during normal operation. The top surface of the heat exchangers and the cold shield is believed to be the warmest.

Titanium heat exchanger	alumina heat exchanger (top surface)	cold shield (top)
52 ± 5 (K)	60 ± 5 (K)	60 ± 5 (K)

8.3 Radiofrequency Simulations

8.3.1 Resonant Frequency

The superconducting coils installed in the probe must be tunable experimentally to the Larmor frequency of interest. The coils are constituted by two circular sapphire substrates. The interposition of a 0.075-mm-thick layer of thermal compound (Apiezon N, M&I Materials Ltd., Manchester, United Kingdom) allows the substrates to adhere to each other while guaranteeing proper heat transfer. The first substrate is a double-sided

superconducting horse-shoe coil: a c-shaped superconducting trace has been deposited on each side of the substrate. In contrast, the second substrate is single-sided. It can be rotated by hand around its axis to tune the probe to the desired resonant frequency.

The double-sided substrate was designed to resonate at 440 MHz. The single-sided substrate does not resonate alone. Depending on the angular position of the single-sided substrate, the two substrates together resonate from a few megahertz below 400 MHz to 432.8 MHz.

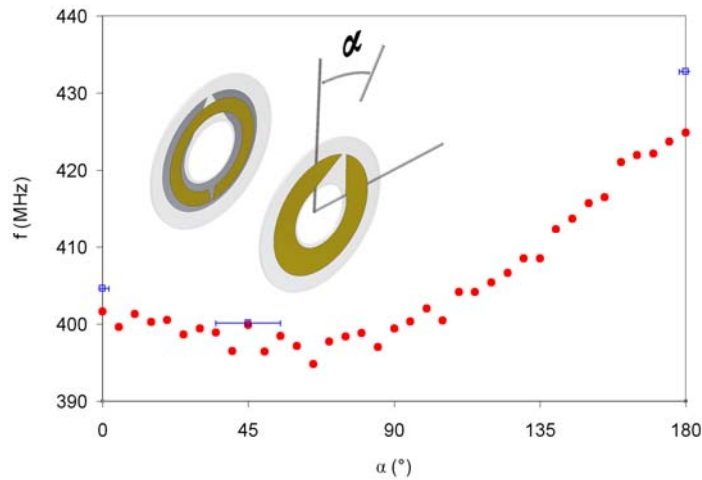


Figure 8-2: The angular position of the single-sided substrate changes the resonant frequency of the assembly constituted by the double-sided substrate and the single-sided substrate. For clarity, the two substrates are depicted apart from each other. Within the probe, they adhere to each other by interposition of a thin layer of thermal compound. The resonant frequency of the probe was recorded experimentally (\square). In practice, the thickness of the thermal compound layer strongly impacts the resonant frequency. The thickness of the layer was measured and then used as an input into the radiofrequency model. The resonant frequency of the probe predicted by the radiofrequency model (\bullet) is in good agreement with experimental values.

During the assembly of the probe, the angular position of the single-sided substrate was iteratively selected so that the probe resonates at 400.10 MHz. The top surface of the alumina heat exchangers was then partially covered by copper to increase the probe resonant frequency to 400.27 MHz.

In practice, supplementary tuning mechanisms are available. During the preliminary set-up of the probe, a set of screws adjusts the separation distance between the two titanium heat exchangers, altering the geometry of the shield and the inductive coupling between coils. If needed, minor adjustment in the probe resonant frequency can be made iteratively.

8.3.2 Impedance

Radiofrequency simulations indicate that the impedance match can be achieved by a coupling loop small enough to be placed within the sample well, which is a great advantage in practice. A coupling loop external to the probe housing can be adjusted easily without warming the probe and opening the housing. In addition, no adjustment mechanism internal to the probe needs to be implemented, which strongly mitigates clearance constraints imposed by a 4-cm diameter probe.

A 5 mm outer-diameter coupling loop was made from silver-plated copper, 0.32 mm-diameter wire. The coupling loop was made resonant close to 400 MHz by using a 10 pF ceramic capacitor (100 B series, non-magnetic, American Technical Ceramics Corp., Huntington Station, NY) soldered in series. The coupling loop is located approximately 12 mm from the superconducting coil center. A half-wavelength long, 1.2 mm outer-diameter low-loss coaxial cable (UT-047C-LL, micro-coax, Pottstown, PA) connects the coupling loop to a low-loss T/R switch and preamplifier hybrid (Nova Medical, Wilmington, MA).

Table 8-2: Size and position of the coupling loop, recorded experimentally and predicted by the radiofrequency simulations, showing good agreement.

	Average Diameter of the Coupling Loop (mm)	Diameter of the Coupling Loop Wire (mm)	Offset from Probe Center (mm)
experimental	5	0.3	12
simulation	4.5	0.5	8

8.3.3 Filling Factor

Radiofrequency simulations indicated that the beryllia probe suffered from a low filling factor. In contrast, the alumina probe was designed to maximize the filling factor.

To increase the amount of magnetic energy deposited in the specimen, therefore maximizing the filling factor, the total clearance between the inner edge of the superconducting trace and the outer edge of the specimen must be kept as small as possible. Consequently, the superconducting trace was deposited as close to the inner edge of the sapphire substrate as achievable. The manufacturer (Theva GmbH, Ismaning, Germany) required at least half a millimeter. A particularly careful alignment between the alumina heat exchangers -securing the coils- and the probe housing -holding the sample well- allowed the clearance between the sapphire substrate and the sample well to be reduced to 1 mm. In addition, the layer of nitrogen flowing around the cartridge was reduced to a thickness of 0.6 mm. The thickness of the cartridge walls was limited to 0.8 mm.

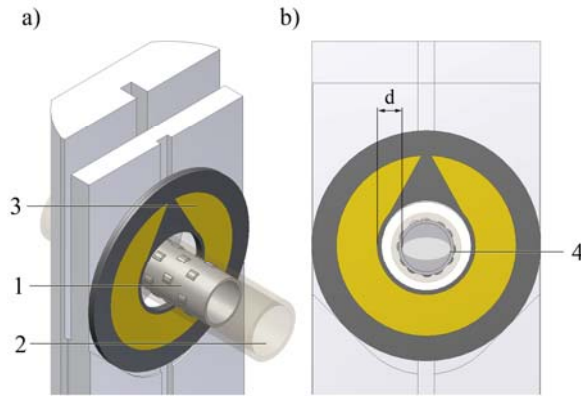


Figure 8-3: (a) perspective of the alumina probe. For clarity, one lateral alumina heat exchanger was removed. The cartridge (1) is placed within the sample well (2), at the center of the superconducting coils (3). (b) Side view of the alumina probe. The distance d between the inner edge of the superconducting trace and the outer edge of specimen (4) was kept as small as possible to maximize the filling factor.

The filling factor cannot be measured easily; therefore, no experimental value will be provided. However radiofrequency simulations predict that the filling factor in the alumina probe is more than four times as large as in the beryllia probe (see 7.6):

$$\eta_{\text{alumina}} = 0.050 \pm 0.003$$

8.3.4 Sensitivity

The power dissipated by each component was calculated by our radiofrequency model. The equivalent resistance, as well as the absolute temperature, of every probe component is listed below:

Table 8-3: transformed resistance and absolute temperature of the alumina probe components.

$R_{sp, T} (\Omega)$	$R_{co, T} (\Omega)$	$R_{sh, T} (\Omega)$	$R_{ce, T} (\Omega)$	$R_{ra, T} (\Omega)$	$R_{cl} (\Omega)$
32.7 ± 6.5	15.7 ± 3.1	16.0 ± 3.2	0.6 ± 0.1	0.02 ± 0.004	0.8 ± 0.2
$T_{sp} (K)$	$T_{co} (K)$	$T_{sh} (K)$	$T_{ce} (K)$	$T_{ra} (K)$	$T_{cl} (K)$
293	60	60	60	293	293

The equivalent resistance of the specimen increased to 32.7Ω in the alumina probe, as compared to 13.9Ω in the beryllia probe. In the ideal case where no loss takes place within the probe, the resistance of the specimen would be 50Ω , underlining the increased sensitivity of the alumina probe.

Based on equation (5-4) on p. 55, the sensitivity S_{alumina} of the alumina probe is three times as large as the sensitivity of the beryllia probe (see 7.7):

$$S_{\text{alumina}} = 29.8 \pm 6.0 \text{ (a. u.)}$$

8.3.5 Quality Factor

The quality factor of the unloaded probe measured outside the imaging magnet is 24'000. When the cerebellum is inserted in the probe, the quality factor decreases to 12'000. Consequently, losses within the specimen are equal to the losses within the probe, which is consistent with our radiofrequency model.

The decrease in quality factor when the specimen is inserted into the probe reveals a very good coupling between the probe and the specimen. In addition, the probe operates in a regime where the noise stemming from the probe has been reduced to a level comparable to the noise originating from the specimen.

8.4 Imaging

A perfusion-fixed C57BL/6 mouse cerebellum, actively stained by transcardial perfusion with a mixture of 10% buffered formalin and ProHance (Bracco S.p.A., Milano, Italy) was imaged using a gradient-recalled sequence. Acquisition parameters were: GRE, Flip angle = 90°, TR = 100 ms, TE = 5.2 ms, FOV = 12 x 6 x 6 mm, Bandwidth = 62.5

kHz, NEX=1, Voxel Size 12 x 12 x 12 micron, array size = 1024 x 512 x 512, 67% k-space asymmetric sampling in the frequency direction only. The total imaging time was 7.5 hours. The SNR ranged from 16 in the darkest region of the specimen to 45 in the brightest areas.

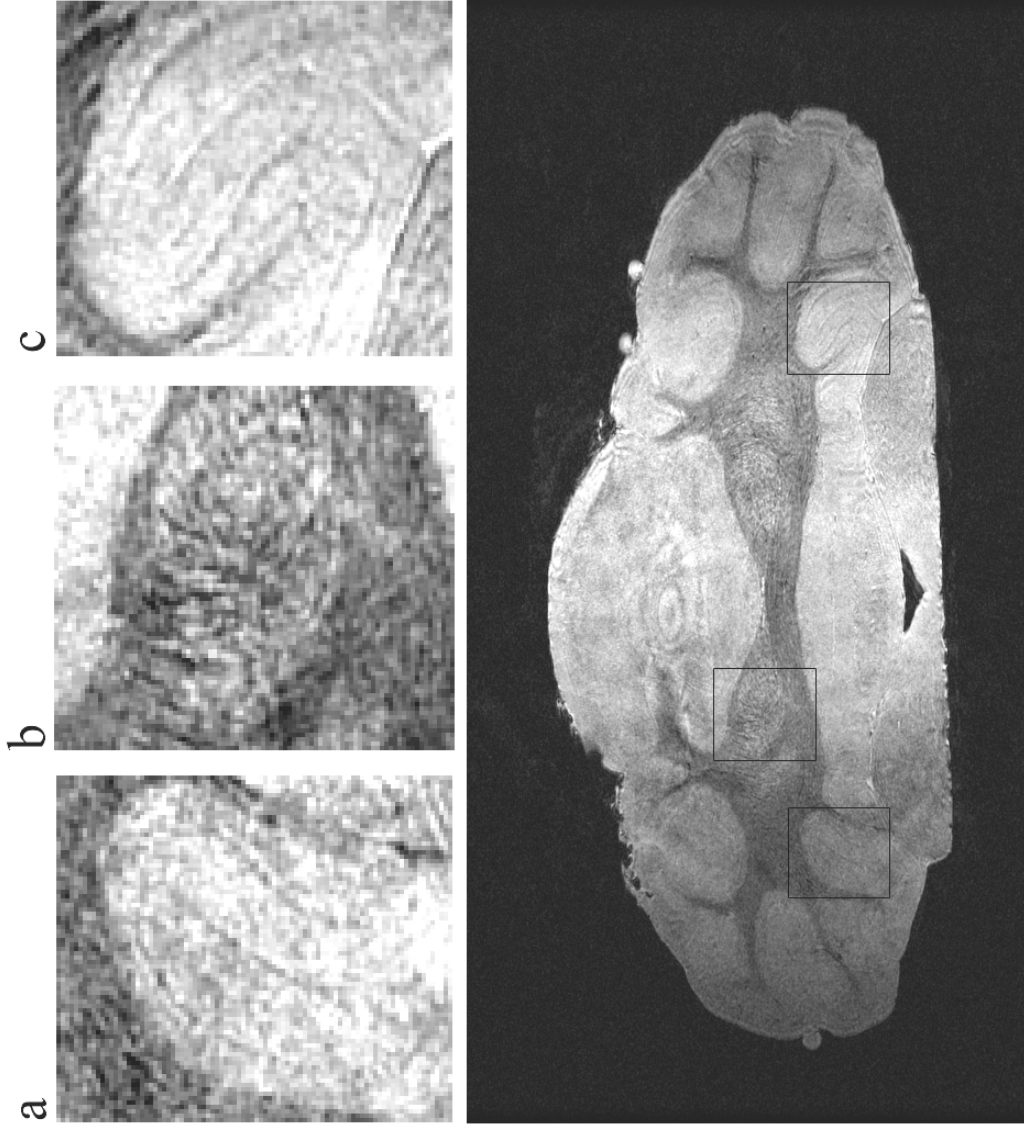


Figure 8-4: (a,c) The layering of the cerebellum is apparent in the image acquired by the alumina superconducting probe. Signal-to-noise ratio ranges from 18 to 45

For comparison, the same imaging sequence was repeated on a different specimen using a room-temperature copper solenoid, 12 mm diameter, 22 mm long. The SNR was below 7.

8.5 Sensitivity and SNR comparisons

The specimens imaged by the beryllia and alumina probes were perfused with contrast agents and fixed the same way. We will assume that they offer the same magnetization per unit of volume. During imaging, the echo-time used was similar between the two probes, the bandwidth and repetition time were identical. However, the encoded resolution in the alumina probe was twice as high as the resolution of the beryllia probe, and the duration of the imaging scan was more than twice as short for the alumina probe.

Table 8-4: Imaging volume, voxel volume, echo-time, repetition time, bandwidth, number N of samples acquired in the frequency-encoding direction, and acquisition time used by the beryllia probe and the alumina probe.

Probe	Imaging Volume (mm ³)	Voxel Volume (pL)	Echo time (ms)	repetition time (ms)	Imaging Bandwidth (kHz)	N	Acquisition time (hr)
beryllia	432	2	5.5	100	62.5	768	16.5
alumina	2662	1	5.2	100	62.5	682	7.5

In the table below, according to equation (1-1) on p. 3, we normalize the SNR acquired experimentally by the square-root of acquisition-time and the number of samples acquired in the frequency-encoding direction, as well as the voxel volume:

Table 8-5: The SNR recorded experimentally was divided by the square-root of acquisition time ($\text{hr}^{-1/2}$), the square root of N, the voxel volume (pL^{-1}) and for convenience, multiplied by 100.

Probe	SNR	normalized SNR ($100 \cdot \text{hr}^{-1/2} \text{ pL}^{-1}$)
beryllia	18	8.0
alumina	31	43.3

The fractional improvement in normalized SNR found experimentally is:

$$\frac{\text{Normalized SNR}_{\text{alumina}}}{\text{Normalized SNR}_{\text{beryllia}}} = \frac{43.3}{8.0} = 5.4$$

The fractional increase in probe sensitivity, predicted by simulation, is:

$$\frac{\text{Sensitivity}_{\text{alumina}}}{\text{Sensitivity}_{\text{beryllia}}} = \frac{29.8}{9.8} = 3$$

The fractional improvement in probe sensitivity predicted by simulations is smaller than the fractional increase in normalized SNR recorded experimentally. Numerous factors may explain the difference. Radiofrequency inhomogeneity in both probes may bias our SNR estimations. In the radiofrequency simulations, the conductivity of the superconducting films and the specimen may be inaccurate. Less favorable experimental circumstances may lead to a lower SNR in the case of the beryllia probe, including an imperfect power match, a flip angle set incorrectly, or the improving skill level of a graduate student under training.

8.6 Important Aspects of the Probe Design

8.6.1 Alignment

The misalignment –unavoidable in practice– of the titanium heat exchangers within the probe housing must be limited to significantly less than the clearance available around the sample well, 1 mm, so that the superconducting coils are centered around the sample well. During the probe set-up, different sets of screws adjust the vertical and horizontal location of the titanium heat exchangers. Protruding guides machined on the titanium heat exchanger limit misalignment between the titanium and the alumina parts. Finally, edges machined in the alumina guarantee minimal misalignment of the superconducting coils.

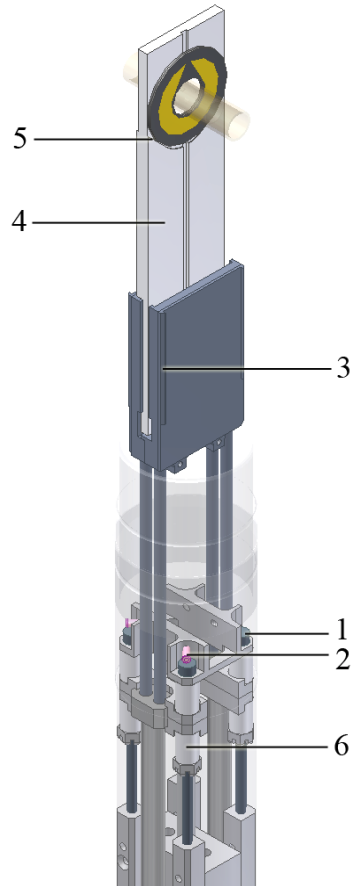


Figure 8-5: To maximize the filling factor of the probe, the clearance between the coils and the sample well must be minimal which requires the precise alignment of all the probe components. Four screws (1) adjust the vertical position of the superconducting coils around the sample well. Four supplementary set-screws (2) adjust the horizontal position of the coils. Edges (3) were machined in the titanium heat exchangers to facilitate the correct alignment of the alumina components (4). Finally, shoulders (5) machined in the alumina heat exchangers make the alignment of the coils easier. Low thermal conductivity ceramic washers (6) limit the heat load towards the titanium heat exchangers.

8.6.2 Heat Transfer, Thermal Contraction and Vacuum

Precision-machined metal clamps minimize misalignment of the titanium heat exchanger within the probe housing. The high thermal conductivity of the metal clamps causes a significant heat load towards the cold heat exchangers. To guarantee the correct alignment and a sufficient thermal isolation of the titanium heat exchangers, the path of heat transfer was interrupted by two stages of low thermal conductivity ceramic washers (see Figure 8-5)

Mechanical stress due to thermal contraction during cooling may induce a thermal bond to break or even the catastrophic failure of an entire component. The linear expansion coefficient of alumina ($5.4 \cdot 10^{-6} \text{ K}^{-1}$) is sufficiently close to titanium ($8.6 \cdot 10^{-6} \text{ K}^{-1}$) to prevent the alumina heat exchangers from cracking during the cooling process. However, a transition from titanium to stainless steel must occur somewhere along the path of cold helium vapor so that affordable, off-the-shelf stainless steel gas connectors can be used. The linear expansion of stainless steel ($16 \cdot 10^{-6} \text{ K}^{-1}$) is twice as large as titanium; the contraction occurring in a 60 cm long probe cooled from room-temperature to 60 K exceeds 2 mm, more than the clearance available between the immobilized sample well and the sapphire substrates, and as large as a third of the imaging field-of-view. Consequently, a frame kept mostly at room-temperature guarantees the alignment of the superconducting coil to the sample well. The clamps holding the titanium heat

exchangers are located in close proximity to the probe isocenter, so that a short 10-cm long section of titanium tubing and alumina causes a misalignment limited to 0.2 mm.

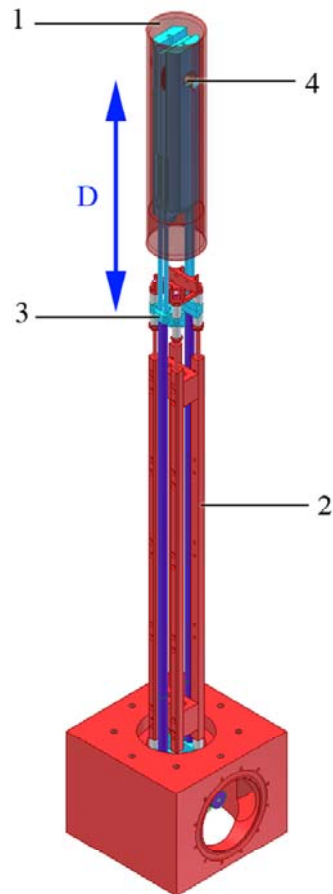


Figure 8-6: Room-temperature components (red) do not shorten during the cooling of the probe. In contrast, components cooled below 60 K (blue) become up to 2 mm smaller. So that the superconducting coils travel a tolerable distance within the probe housing (1), a room temperature frame (2) is attached (3) to the cold components close to the center of the coils (4). A short length of titanium and alumina (D) limits the travel of the coils due to thermal contraction to less than 0.2 mm.

A radiofrequency shield must be thin to limit electromagnetic losses due to eddy currents. When the shield is cooled, a thin cross-section limiting eddy currents conflicts with the need of a bulky heat-transfer cross-section enabling robust heat exchange. The alumina probe presents bulky ceramic heat exchangers cooling down a thin, one thousandth-of-an-inch copper shield, reconciling the design requirements.

Within the probe, vacuum insulation limits deleterious heat transfer towards cold components to thermal radiation. A twenty-layer aluminized mylar shield encompasses most cold components to reduce the radiative thermal load. As a supplementary measure to accelerate the probe housing evacuation process and to avoid vacuum virtual leaks, a loose, 10-mm-opening mesh was intertwined between each layer.

Similarly, to minimize housing evacuation time and to prevent vacuum virtual leaks, all threads exposed to vacuum feature vented hardware. All components exposed to vacuum were ultrasonically cleaned with a solution of deionized water and organic solvent (Alconox, Alconox Inc., White Plains, NY), rinsed five times in deionized water, and further ultrasonically cleaned in acetone and subsequently in methanol. Assembly was carried out using vinyl glove to prevent the deposition of volatile finger prints.

To reach a low base pressure, as few seals as possible were implemented. O-rings were vacuum-baked to eliminate volatile residues. A low outgassing polymer was selected for the probe housing (PETG polymer, part number 9245K47, McMaster, Aurora, OH) based on outgassing properties published by the National Aeronautics and Space Administration (Outgassing Data for Selecting Spacecraft Materials, <http://outgassing.nasa.gov>). The surface exposed to vacuum was left unmachined to minimize the outgassing surface area. A soft, low-outgassing cryogenic epoxy glue (Arathane 5753, Specialty Polymer, Valencia, CA) was selected to bond components.

8.6.3 Microphonics

Microphonics can cause severe artifacts during imaging. At a 10 μm encoding resolution, vibrations within the probe must be limited to a significantly smaller fraction than the encoding resolution. The Gifford-McMahon cycle cryocooler generates vibrations during the mechanical expansion of helium by a piston. Shock absorbing bumpers (part number 9305K29, McMaster, Aurora, OH) were retrofitted onto the supports of the cryorefrigerator cold head. In addition, the cryocooler cart was mounted on high-deflection, spring-action vibration-damping mounts (part number 6219K73, McMaster, Aurora, OH) supported by rubber vibration-damping pads (part number 60015K43, McMaster, Aurora, OH). The shock absorbing devices limited microphonics to tolerable levels.

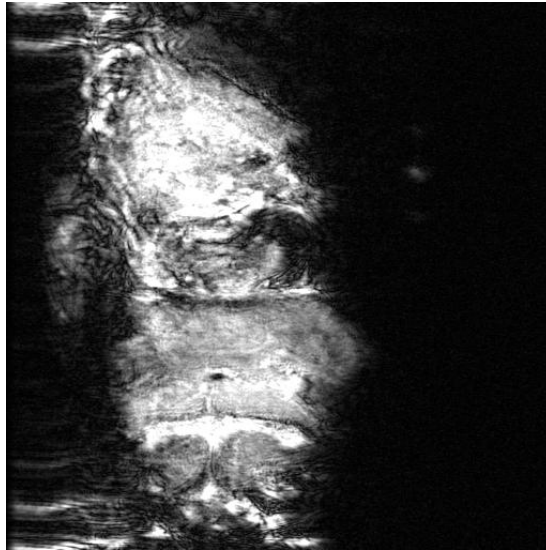


Figure 8-7: Severe artifacts due to microphonics are apparent in an image of 9-day mouse embryo, imaged at 11 μm isotropic resolution.

A thorough optimization of the imaging sequence was not undertaken. Because of the non-linear power transmission behavior of the YBCO superconducting film, the flip angle may be underestimated. Soft pulses have been used; a comparison in image quality with hard pulses should be carried out. The filtering effects of the high-quality-factor resonator should be quantified.

9 Summary

The first superconducting probe for MR microscopy was introduced by this laboratory more than 15 years ago. A number of subsequent studies were performed at Duke and elsewhere. The improvement in sensitivity delivered by a superconducting probe has been uniformly less than predicted by theory. This dissertation has developed a detailed finite-element model that has allowed us to explore quantitatively the electromagnetic performance of these probes.

Our finite-element-based radiofrequency simulations can accurately assess the probe resonant frequency and the geometry leading to an impedance match before the probe is actually built. In addition, radiofrequency simulations assess the electromagnetic losses caused by each component within a probe and compute an equivalent resistance for every probe component. Excluding the specimen being imaged, the component exhibiting the largest resistance, and consequently inducing the largest loss, can be identified. To increase the probe sensitivity, that component can be cooled or design alternatives can be considered to decrease its resistance. Applied iteratively, the method identifies relevant design changes which in turn lead to an increased probe sensitivity.

We showed that the sensitivity of an existing superconducting Helmholtz pair

can be improved by increasing the filling factor of the probe and cooling the radiofrequency shield. In the design of a subsequent probe, we implemented a cold shield and significantly increased the filling factor. Simulations indicate that the alumina probe is three times as sensitive as the beryllia probe, whereas SNR measurements indicate a factor of 5. By extension, the alumina probe can reach a resolution twice as high in less than half the scan acquisition time.

SNR measurements carried out with both probes indicate that the gain in sensitivity between the two probes is larger than predicted. The supplementary SNR delivered by the alumina probe may be used to increase resolution further, shorten scan time, or both.

During the design of a new probe, radiofrequency simulations are a crucial tool enabling the shortening of the lead-time to delivery. They predict the most significant figures of merit relevant for magnetic resonance imaging and identify areas where a modified design may be beneficial. Accompanied by a theoretical understanding of noise and signal transmission within coupled components, the sensitivity of the probe can be extracted and the optimal design identified.

Under the assumption that the transverse magnetization per unit of volume is

identical between different experiments using different radiofrequency probes, the method can be extended to predict the relative change in SNR. Consequently, the worthiness of a radiofrequency probe can be assessed directly from the standpoint of imaging performance.

10 Appendix

10.1 Radiofrequency Model of the Beryllia Probe

The electronic file describing the beryllia probe is available at the CIVM under the name "20090201-SuperconductingProbes". The model pertaining to the beryllia probe is called "Beryllia" and is saved in HFSS version 10.3.1. The model excitation is modal, at the terminals of the coupling loop. The input power is 50 W. The model includes the components listed in the table below, alongside of their radiofrequency properties.

Table 10-1: Electromagnetic properties of the components included in the radiofrequency model of the Beryllia probe

Component	Ceramic Heat Exchange r	Specimen	Cartridge	Substrate	Coupling Loop	Shield	HTS Coil
HFSS Material	N/A	N/A	N/A	N/A	Copper	Copper	N/A
Relative Permittivity	6.8	50	2	10	1	1	1
Relative Permeability	1	1	1	1	0.999991	0.999991	0.999991
Conductivity (S/m)	0	1	1.6E-12	0	5.8E7	5.8E7	1E12
Dielectric Loss Tangent	0.0005	0.5	0.02	1e-6	0	0	0
Magnetic Loss Tangent	0	0	0	0	0	0	0
Magnetic Saturation	0	0	0	0	0	0	0
Lande G Factor	2	2	2	2	2	2	2
Delta H (A/m)	0	0	0	0	0	0	0

The maximum size of the finite-element mesh describing each component is listed below.

Table 10-2: Mesh size for each component of the radiofrequency model of the Beryllia probe

Component	Ceramic Heat Exchanger	Specimen	Cartridge	Substrate	Coupling Loop	Shield	HTS Coil
Maximum Mesh Size (mm)	15	3	3	10	2	30	5

The maximum mesh size is multiplied by a uniteless factor, called "MyMesh", varying from 0.5 to 1.5 in 0.1 increments. Consequently, the model is solved 11 times. For each solution, the resonant frequency is determined by identifying the minimum of the S11 curve. At the resonant frequency, for each component, the phase corresponding to peak losses is identified. The dissipated power is displayed for the component at the resonant frequency and phase corresponding to peak losses. The resistance values presented in this dissertation are given by the mean of the 11 solutions.

10.2 Radiofrequency Model of Alumina Probe

The electronic file describing the Alumina probe is available at the CIVM under the name "20090201-SuperconductingProbes". The model pertaining to the Alumina probe is called "Alumina" and is saved in HFSS version 10.3.1. The model is similar to the Beryllia probe model, and is solved in a similar fashion. The materials and mesh size are presented below.

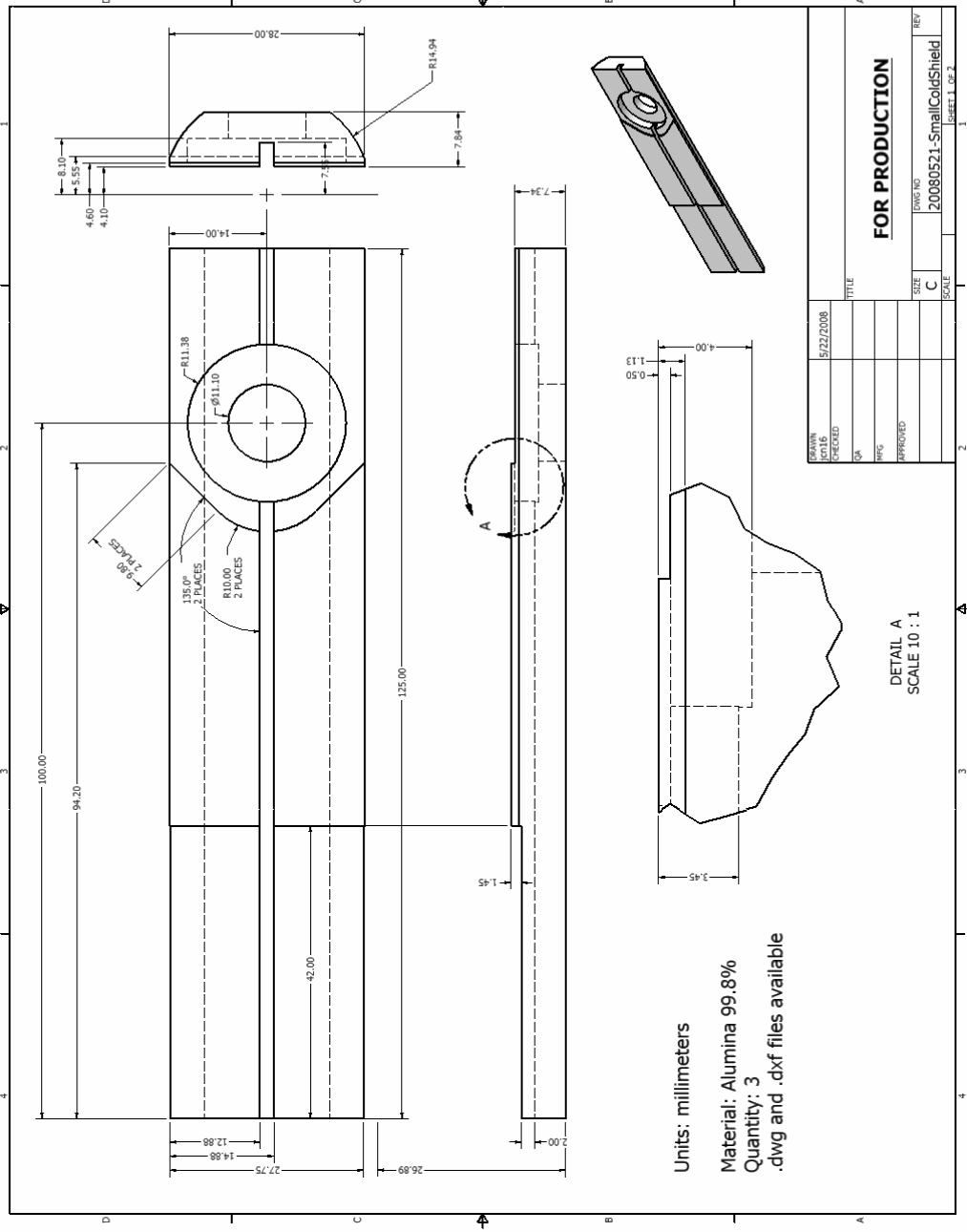
Table 10-3: Electromagnetic properties of the components included in the radiofrequency model of the Alumina probe

Component	Ceramic Heat Exchanger	Specimen	Cartridge	Substrate	Coupling Loop	Shield	HTS Coil
HFSS Material	alumina_96pct	N/A	N/A	N/A	Copper	N/A	N/A
Relative Permittivity	9.4	50	2	10	1	1	1
Relative Permeability	1	1	1	1	0.999991	0.999991	0.999991
Bulk Conductivity (S/m)	0	1	1.6E-12	0	5.8E7	4.7E8	1E12
Dielectric Loss Tangent	0.006	0.5	0.02	1e-6	0	0	0
Magnetic Loss Tangent	0	0	0	0	0	0	0
Magnetic Saturation	0	0	0	0	0	0	0
Lande G Factor	2	2	2	2	2	2	2
Delta H (A/m)	0	0	0	0	0	0	0

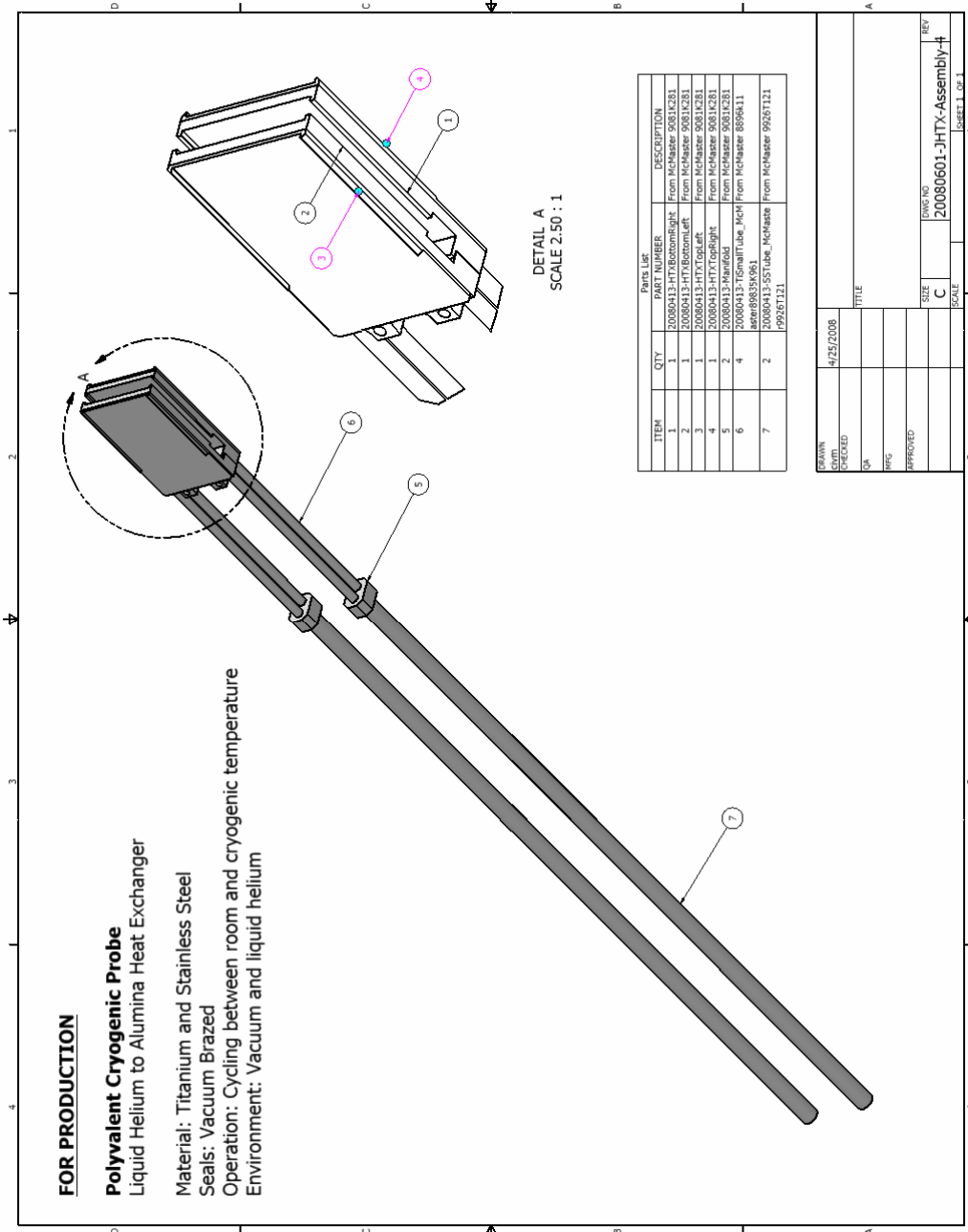
The maximum size of the finite-element describing each component is listed below.

Table 10-4: Mesh size for each component of the radiofrequency model of the Alumina probe

Component	Ceramic Heat Exchanger	Specimen	Cartridge	Substrate	Coupling Loop	Shield	HTS Coil
Maximum Mesh Size (mm)	25	2	4	10	0.2	30	0.5



10.4 Titanium Heat Exchangers



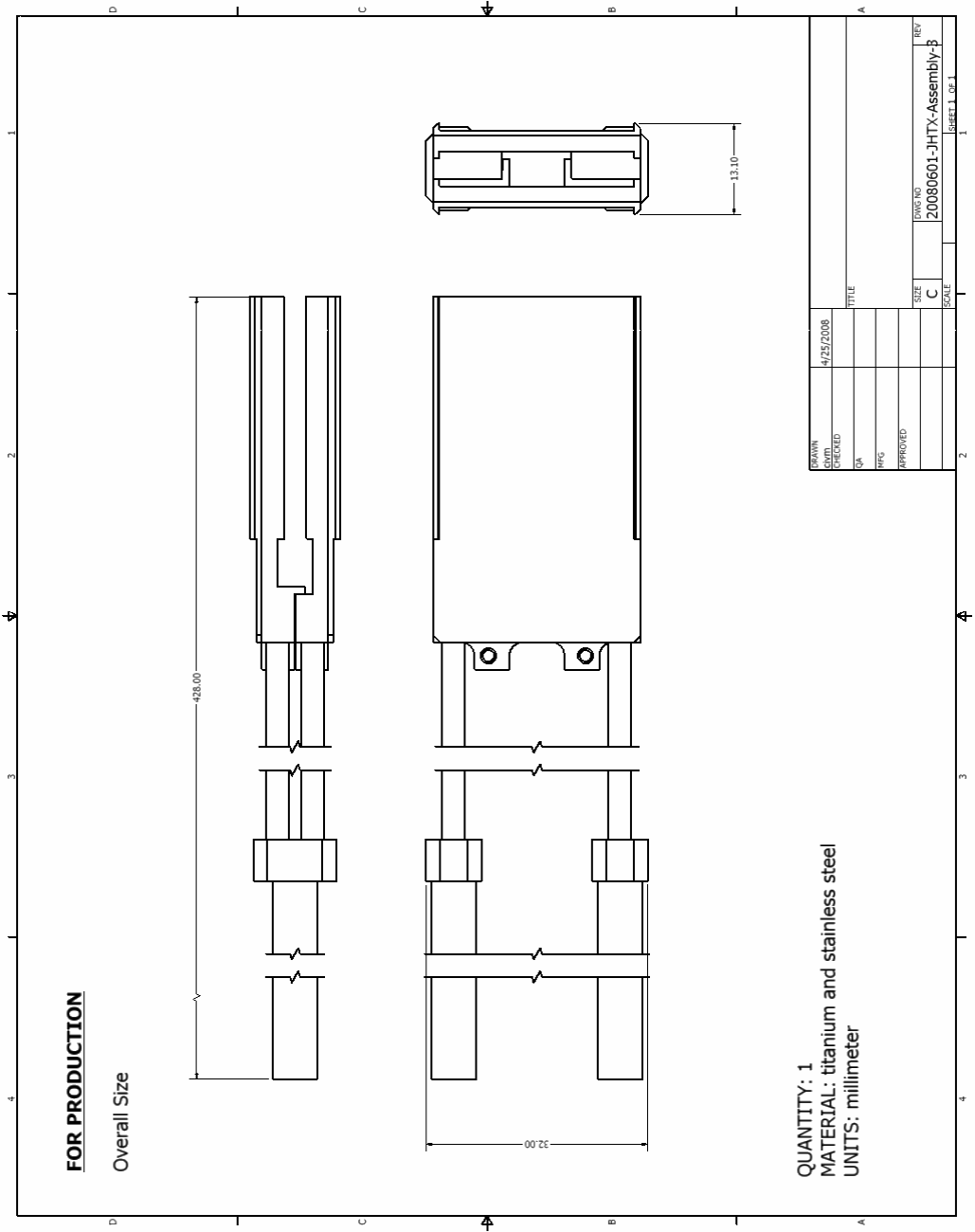
FOR PRODUCTION

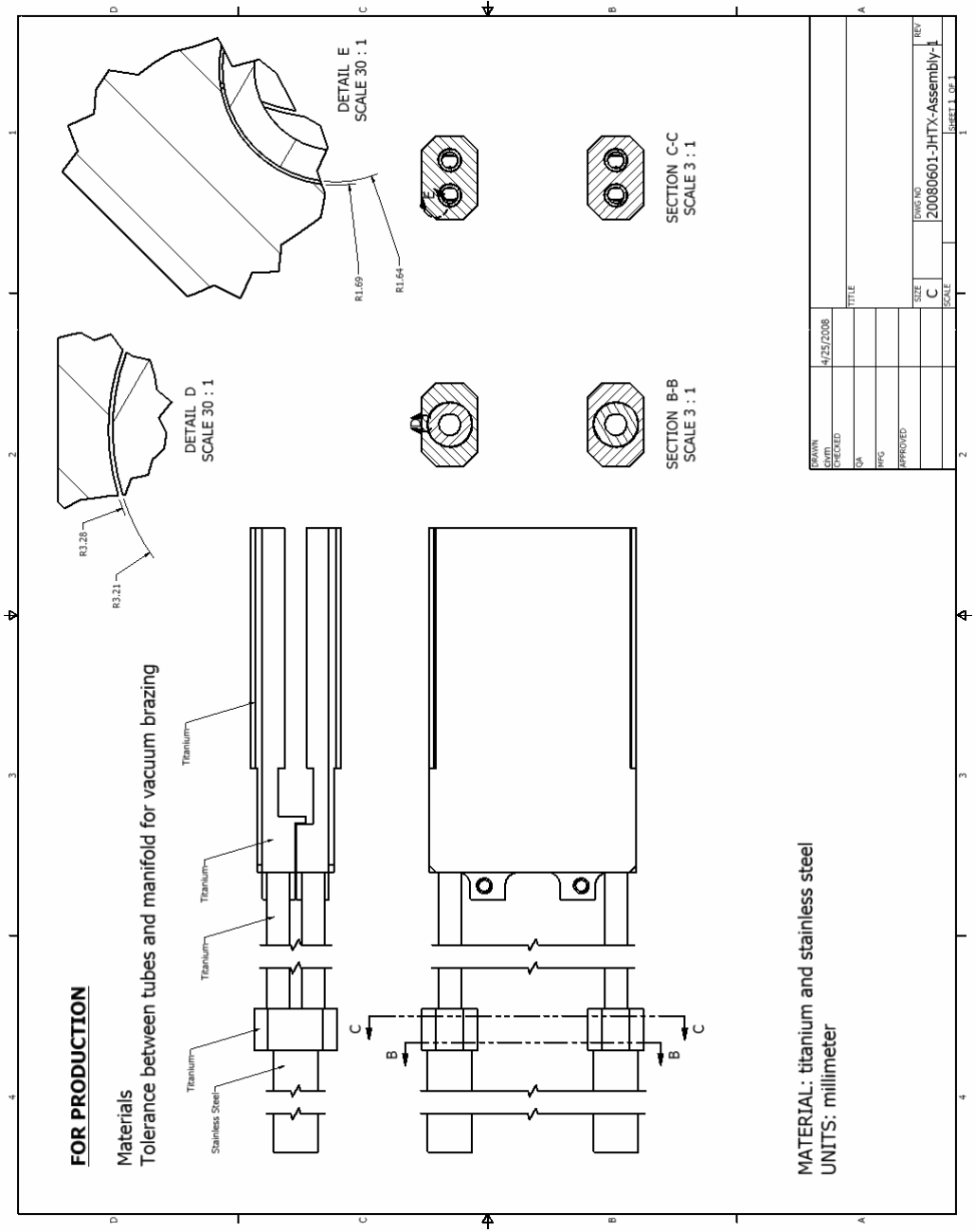
Polyvalent Cryogenic Probe
Liquid Helium to Alumina Heat Exchanger

Material: Titanium and Stainless Steel
Seals: Vacuum Braze
Operation: Cycling between room and cryogenic temperature
Environment: Vacuum and liquid helium

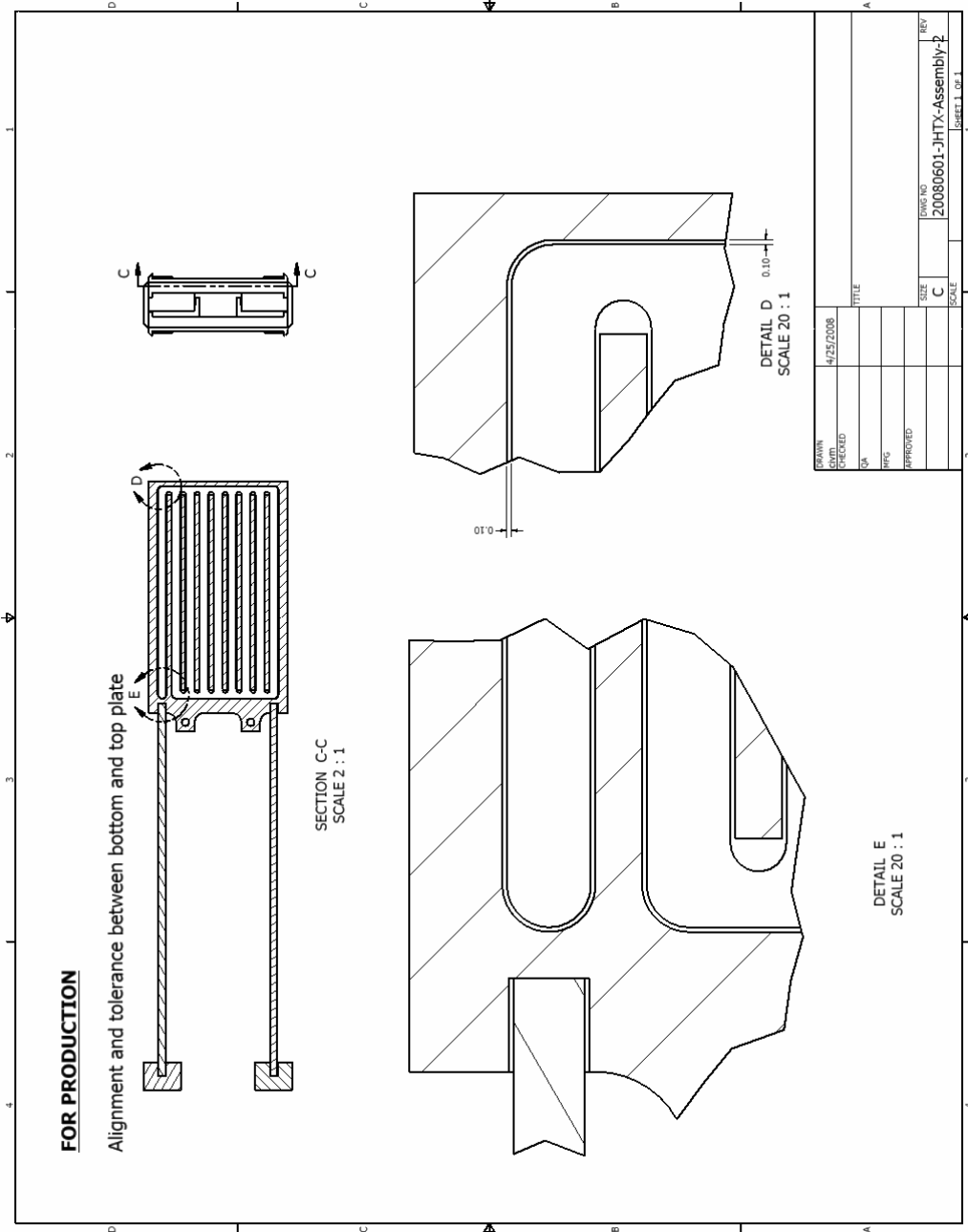
ITEM	QTY	DATE LUP	PART NUMBER	DESCRIPTION
1	1		20080413-HTXBottomRight	From McMaster 50814281
2	1		20080413-HTXBottomLeft	From McMaster 50814281
3	1		20080413-HTXTopLeft	From McMaster 50814281
4	1		20080413-HTXTopRight	From McMaster 50814281
5	2		20080413-Manifold	From McMaster 50814281
6	4		20080413-TitaniumTube, 1/2"	From McMaster 8896411
7	2		9926T121	From McMaster 9926T121

DATE	4/25/2008
TITLE	
SCALE	C
SIZE	
DWG NO	20080601-JHTX-Assembly-#
REV	
SECTION	1 OF 1

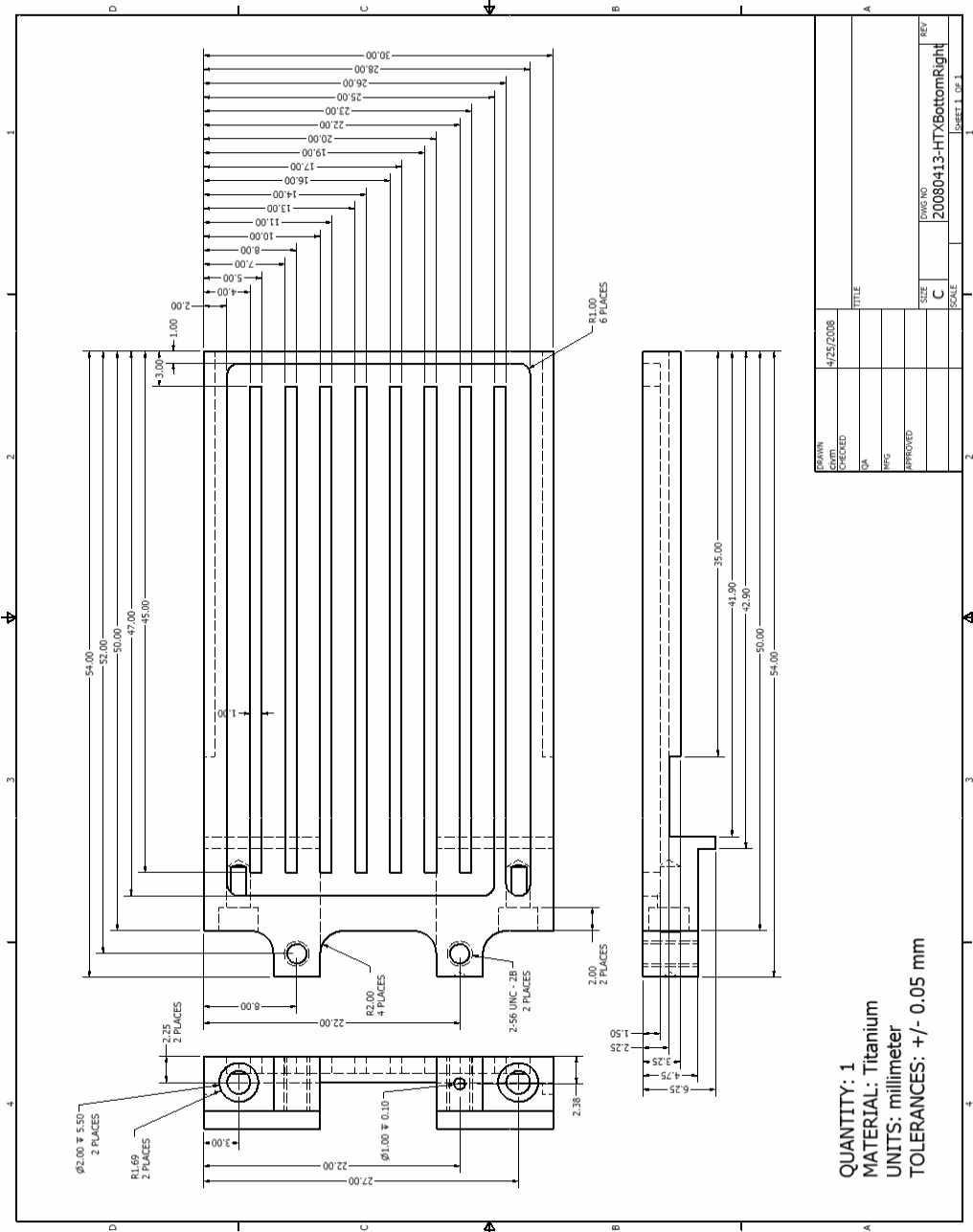




DATE	4/25/2008	TITLE	
DRAWN		SCALE	
CHECKED		SIZE	C
QA		DWG NO	20080601-JHTX-Assembly-I
WFG		REV	
APPROVED		SHEET	1 OF 1



DATE	4/25/2008	TITLE	
BY		SCALE	C
CHECKED		SIZE	A
QA		DWG NO	20080601-JHTX-Assembly-2
APP'D		REV	1
APPROVED		SHEET	1 OF 1



References

1. Lauterbur PC, Image Formation By Induced Local Interactions - Examples Employing Nuclear Magnetic-Resonance. *Nature* 1973;242(5394):190-191.
2. Mansfield P, Grannell PK. NMR Diffraction In Solids. *Journal of Physics C-Solid State Physics* 1973;6(22):L422-L426.
3. Beck B, Plant DH, Grant SC, Thelwall PE, Silver X, Mareci TH, Benveniste H, Smith M, Collins C, Crozier S, Blackband SJ. Progress in high field MRI at the University of Florida. *Magnetic Resonance Materials in Physics Biology and Medicine* 2002;13(3):152-157.
4. Hoult DI, Richard RE. The signal-to-noise ratio of the magnetic resonance experiment. *Journal of Magnetic Resonance* 1976(24):71-85.
5. Hoult DI, Lauterbur PC. Sensitivity Of The Zeugmatographic Experiment Involving Human Samples. *Journal of Magnetic Resonance* 1979;34(2):425-433.
6. Darrasse L, Ginefri JC. Perspectives with cryogenic RF probes in biomedical MRI. *Biochimie* 2003;85(9):915-937.
7. Black RD, Early TA, Roemer PB, Mueller OM, Mogrocampero A, Turner LG, Johnson GA. A High-Temperature Superconducting Receiver For Nuclear-Magnetic-Resonance Microscopy. *Science* 1993;259(5096):793-795.
8. Black RD, Roemer PB, Mueller OM. Electronics For A High-Temperature Superconducting Receiver System For Magnetic-Resonance Microimaging. *Ieee Transactions on Biomedical Engineering* 1994;41(2):195-197.
9. Bracanovic D, Esmail AA, Penn SJ, Webb SJ, Button TW, Alford NM. Surface YBa₂Cu₃O₇ receive coils for low field MRI. *Ieee Transactions on Applied Superconductivity* 2001;11(1):2422-2424.
10. Cheng MC, Yan BP, Lee KH, Ma QY, Yang ES. A high temperature superconductor tape RF receiver coil for a low field magnetic resonance-imaging system. *Superconductor Science & Technology* 2005;18(8):1100-1105.
11. Damico LA, Summers JJ, Schnall MD. Multiple Frequency Cryogenic NMR Probes. *Proceedings of the Sixth Annual Meeting of the Society of Magnetic Resonance in medicine* 1987;1:97.
12. Ginefri JC, Darrasse L, Crozat P. Comparison of radio-frequency and microwave superconducting properties of YBaCuO dedicated to magnetic resonance imaging.

- IEEE Transactions on Applied Superconductivity 1999;9(4):4695-4701.
13. Hall AS, Barnard B, McArthur P, Gilderdale DJ, Young IR, Bydder GM. Investigation Of A Whole-Body Receiver Coil Operating At Liquid-Nitrogen Temperatures. *Magnetic Resonance in Medicine* 1988;7(2):230-235.
 14. Hall AS, Alford NM, Button TW, Gilderdale DJ, Gehring KA, Young IR. Use Of High-Temperature Superconductor In A Receiver Coil For Magnetic-Resonance-Imaging. *Magnetic Resonance in Medicine* 1991;20(2):340-343.
 15. Hill HDW. Improved sensitivity of NMR spectroscopy probes by use of high-temperature superconductive detection coils. *Ieee Transactions on Applied Superconductivity* 1997;7(2):3750-3755.
 16. Hurlston SE, Brey WW, Suddarth SA, Johnson GA. A high-temperature superconducting Helmholtz probe for microscopy at 9.4 T. *Magnetic Resonance in Medicine* 1999;41(5):1032-1038.
 17. Lee KH, Cheng MC, Chan KC, Wong KK, Yeung SSM, Lee KC, Ma QY, Yang S. Performance of large-size superconducting coil in 0.21T MRI system. *Ieee Transactions on Biomedical Engineering* 2004;51(11):2024-2030.
 18. Lee HL, Lin IT, Chen JH, Horng HE, Yang HC. High-T-c superconducting receiving coils for nuclear magnetic resonance imaging. *Ieee Transactions on Applied Superconductivity* 2005;15(2):1326-1329.
 19. Ma QY, Chan KC, Kacher DF, Gao EZ, Chow MS, Wong KK, Xu H, Yang ES, Young GS, Miller JR, Jolesz FA. Superconducting RF coils for clinical MR imaging at low field. *Academic Radiology* 2003;10(9):978-987.
 20. Miller JR, Zhang K, Ma QY, Mun IK, Jung KJ, Katz J, Face DW, Kountz DJ. Superconducting receiver coils for sodium magnetic resonance imaging. *Ieee Transactions on Biomedical Engineering* 1996;43(12):1197-1199.
 21. Nouls JC, Izenon MG, Greeley HP, Johnson GA. Design of a superconducting volume coil for magnetic resonance microscopy of the mouse brain. *Journal of Magnetic Resonance* 2008;191(2):231-238.
 22. Odoj F, Rommel E, von Kienlin M, Haase A. A superconducting probehead applicable for nuclear magnetic resonance microscopy at 7 T. *Review of Scientific Instruments* 1998;69(7):2708-2712.
 23. Styles P, Soffe NF, Scott CA, Cragg DA, Row F, White DJ, White PCJ. A High-Resolution Nmr Probe In Which The Coil And Preamplifier Are Cooled With Liquid-Helium. *Journal of Magnetic Resonance* 1984;60(3):397-404.

24. Withers RS, Liang GC, Cole BF, Johansson M. Thin-film HTS probe coils for magnetic-resonance imaging. *IEEE Trans. Appl. Supercond.* (USA); 1993; Chicago, IL, USA. p 2450-2453. (*IEEE Trans. Appl. Supercond.* (USA)).
25. Black RD, Roemer PB, Mogrocampero A, Turner LG, Rohling KW. High-Temperature Superconducting Resonator For Use In Nuclear-Magnetic-Resonance Microscopy. *Applied Physics Letters* 1993;62(7):771-773.
26. van Bentum PJM, Janssen JWG, Kentgens PM. Towards nuclear magnetic resonance mu-spectroscopy and mu-imaging. *Analyst* 2004;129(9):793-803.
27. Haacke EM, Brown RW, Thompson MR, Venkatesan R. *Magnetic Resonance Imaging: Physical Principles and Sequence Design*. New York: Wiley-Liss; 1999.
28. Johnson JB. Thermal agitation of electricity in conductors. *Physical Review* 1928;32(1):97-109.
29. Nyquist H. Thermal agitation of electric charge in conductors. *Physical Review* 1928;32(1):110-113.
30. Pozar DM. *Microwave engineering*. Hoboken, NJ: John Wiley; 2005. xvii, 700 p. p.
31. Ginefri JC, Darrasse L, Crozat P. High-temperature superconducting surface coil for in vivo microimaging of the human skin. *Magnetic Resonance in Medicine* 2001;45(3):376-382.
32. Glover P, Mansfield P. Limits to magnetic resonance microscopy. *Reports on Progress in Physics* 2002;65(10):1489-1511.
33. Brunner P, Ernst RR. Sensitivity And Performance Time In Nmr Imaging. *Journal of Magnetic Resonance* 1979;33(1):83-106.
34. Weinmann HJ, Brasch RC, Press WR, Wesbey GE. Characteristics Of Gadolinium-Dtpa Complex - A Potential NMR Contrast Agent. *American Journal of Roentgenology* 1984;142(3):619-624.
35. Tweedle MF. The ProHance story: the making of a novel MRI contrast agent. *European Radiology* 1997;7:S225-S230.
36. Glover GH, Pauly JM. Projection Reconstruction Techniques For Reduction Of Motion Effects In MRI. *Magnetic Resonance in Medicine* 1992;28(2):275-289.
37. Ginefri JC, Poirier-Quinot M, Girard O, Darrasse L. Technical aspects: Development, manufacture and installation of a cryo-cooled HTS coil system for high-resolution in-vivo imaging of the mouse at 1.5 T. *Methods* 2007;43(1):54-67.
38. Darrasse L, Kassab G. Quick Measurement Of NMR-Coil Sensitivity With A Dual-

- Loop Probe. *Review of Scientific Instruments* 1993;64(7):1841-1844.
39. Ginefri JC, Durand E, Darrasse L. Quick measurement of nuclear magnetic resonance coil sensitivity with a single-loop probe. *Review of Scientific Instruments* 1999;70(12):4730-4731.
 40. Girard O, Ginefri JC, Poirier-Quinot M, Darrasse L. Method for nonlinear characterization of radio frequency coils made of high temperature superconducting material in view of magnetic resonance imaging applications. *Review of Scientific Instruments* 2007;78(12).
 41. Miller JR, Hurlston SE, Ma QY, Face DW, Kountz DJ, MacFall JR, Hedlund LW, Johnson GA. Performance of a high-temperature superconducting probe for in vivo microscopy at 2.0 T. *Magnetic Resonance in Medicine* 1999;41(1):72-79.
 42. Fang J, Chow MS, Chan KC, Wong KK, Shen GX, Gao E, Yang ES, Ma QY. Design of superconducting MRI surface coil by using method of moment. *Ieee Transactions on Applied Superconductivity* 2002;12(2):1823-1827.
 43. Gao EZ, Ma QY. A refined circuit model of high temperature superconducting spiral coils for MRI. *Ieee Transactions on Applied Superconductivity* 2001;11(1):403-406.
 44. Serfaty S, Darrasse L, Kan S. Double-bracelet resonator Helmholtz probe for NMR experiments. *Review of Scientific Instruments* 1995;66(12):5522-5526.
 45. Hayes CE, Edelstein WA, Schenck JF, Mueller OM, Eash M. An Efficient, Highly Homogeneous Radiofrequency Coil For Whole-Body NMR Imaging At 1.5-T. *Journal of Magnetic Resonance* 1985;63(3):622-628.
 46. Johnson GA, Cofer GP, Fubara B, Gewalt SL, Hedlund LW, Maronpot RR. Magnetic resonance histology for morphologic phenotyping. *Journal of Magnetic Resonance Imaging* 2002;16(4):423-429.
 47. Johnson GA, Cofer GP, Gewalt SL, Hedlund LW. Morphologic phenotyping with MR microscopy: The visible mouse. *Radiology* 2002;222(3):789-793.
 48. Johnson GA, Ali-Sharief A, Badea A, Brandenburg J, Cofer G, Fubara B, Gewalt S, Hedlund LW, Upchurch L. High-throughput morphologic phenotyping of the mouse brain with magnetic resonance histology. *Neuroimage* 2007;37(1):82-89.

Biography

John C. Nouls

Born

December 21, 1973
Los Angeles, CA



Education

Ph.D. in Biomedical Engineering

Duke University, *Durham, NC*

M.S. in Biomedical Engineering

University hospital of Geneva, *Geneva, Switzerland*

B.S. in Mechanical Engineering

Swiss Federal Institute of Technology, *Lausanne, Switzerland*

Awards and Affiliations

NIH Training Grant 1-T32-EB001040

ISMRM educational stipend, 2007 and 2006. Awarded to students and post-doctoral fellows with exceptional research.

Cover of Journal for Magnetic Resonance 191 (2), April 2008

Member of ISMRM, 2007-present

Member AAAS, 2007-present

Patents

1. World Patent WO/2004/065973, "Multi-Cell Polarizer Systems For Hyperpolarizing Gases"
2. World Patent WO/2002/085417, "Methods And Devices For Moisturizing Hyperpolarized Noble Gases And Pharmaceutical Products Thereof"
3. World Patent WO/2003/098248, "Methods, Systems, Circuits, And Computer Program Products For Determining Polarization Of A Gas"
4. World Patent WO/2004/065974, "Pump System And Method For Transferring Hyperpolarized Gases"

Refereed Publications

1. B Driehuys, **J Nouls**, A Badea, A Petiet, E Bucholz, K Ghagada, L Hedlund, Small-animal imaging with magnetic resonance microscopy, invited paper, ILAR journal, 45: 35-53 (2008).
2. **J Nouls**, M Izenzon, H Greeley and GA Johnson, Design of a superconducting volume coil for magnetic resonance microscopy of the mouse brain, J. Magn. Reson, 191(2):231-238 (2008).

Selected Conference Proceedings

J. Nouls, M. Izenzon, H. Greeley, GA Johnson, "A Superconducting Probe for Magnetic Resonance Imaging", Proc. of the Joint Meeting of the AMPERE/EENC, Lille, France, Sept 6-11 2004

J. Nouls, M. Izenzon, H. Greeley, GA Johnson, "A High-Temperature Superconducting Volume for Magnetic Resonance Microscopy at 9.4T", Proc. of the International Society for Magnetic Resonance Imaging in Medicine, Seattle, May 6-12 2006

J. Nouls, GA Johnson, "A Superconducting for Magnetic Resonance histology at the Diffusion Limit", Proc. of the International Society for Magnetic Resonance Imaging in Medicine, Berlin, Germany, May 19-25 2007